UNIVERSIDADE FEDERAL DE PERNAMBUCO
DEPARTAMENTO DE FÍSICA – CCEN
PROGRAMA DE PÓS-GRADUAÇÃO EM FÍSICA

LUIS GUSTAVO ORTIZ GUTIÉRREZ

APPLICATION OF ATOMIC SYSTEMS FOR COMPUTATION AND FUNDAMENTAL STUDIES ON SUPERRADIANCE

Recife
2017

LUIS GUSTAVO ORTIZ GUTIÉRREZ

APPLICATION OF ATOMIC SYSTEMS FOR COMPUTATION AND FUNDAMENTAL STUDIES ON SUPERRADIANCE

Tese apresentada ao Programa de Pós-Graduação em Física da Universidade Federal de Pernambuco, como requisito parcial para a obtenção do título de Doutor em Física.

Orientador:
Prof. Dr. Daniel Felinto Pires Barbosa
Universidade Federal de Pernambuco

Recife
2017

Catalogação na fonte
Bibliotecário Jefferson Luiz Alves Nazareno CRB 4-1758

O77a Ortiz Gutiérrez, Luis Gustavo.
Application of atomic systems for computation and fundamental studies on superradiance / Luis Gustavo Ortiz Gutiérrez. – 2017.
149 f.: fig., tab.

Orientador: Daniel Felinto Pires Barbosa.
Tese (Doutorado) – Universidade Federal de Pernambuco. CCEN. Física, Recife, 2017.
Inclui referências.

1. Computação quântica. 2. Armadilha de íons. 3. Superradiância. I. Barbosa, Daniel Felinto Pires. (Orientador). II. Titulo.

530.12 CDD (22. ed.) UFPE-FQ 2017-41

LUIS GUSTAVO ORTIZ GUTIÉRREZ

APPLICATION OF ATOMIC SYSTEMS FOR COMPUTATION AND FUNDAMENTAL STUDIES ON SUPERRADIANCE

Tese apresentada ao Programa de Pós-Graduação em Física da Universidade Federal de Pernambuco, como requisito parcial para a obtenção do título de Doutor em Física.

Aprovada em: 17/07/2017.

BANCA EXAMINADORA

_____

Prof. Dr. Daniel Felinto Pires Barbosa
Orientador
Universidade Federal de Pernambuco

_____

Prof. Dr. Márcio Heraclyto Gonçalves de Miranda
Examinador Interno
Universidade Federal de Pernambuco

_____

Profª Drª Sandra Sampaio Vianna
Examinador Interno
Universidade Federal de Pernambuco

_____

Prof. Dr. Ernesto Fagundes Galvão
Examinador Externo
Universidade Federal Fluminense

_____

Prof. Dr. Marcelo Martinelli
Examinador Externo
Universidade de São Paulo

A Constanza y Cynthia

Agradecimentos

Quero principalmente agradecer à família: minha esposa e filha que me acompanham em todos os novos caminhos que se apresentam e, mesmo à distância, aos meus pais e meus irmãos que têm sido muito mais importantes do que eles pensam. Aos meus dois orientadores: Alessandro e Daniel, que me inspiraram em duas áreas diferentes, embora não ter sido o planejado, independentemente das razões, acabou sendo muito positivo para mim. Quero agradecer aos amigos que tornaram os momentos agradáveis entre o dissabor: Julián, Iván, Melissa, Pablo, Luis Fernando, Ariday, Alejo, Alexis, Victor, Wilmer, Raoni, Alyson, Sajid, Fania, etc. Aos meus amigos de fora da universidade: Aurélio, Raquel, Davi, Auxiliadora, Marcela e Marcelo, que têm se tornado verdadeiramente uma família.

Abstract

The ability to coherently manipulate quantum systems enables a wide range of applications in the field of quantum information. In this thesis we are going to address two applications of quantum interaction between light and an atomic medium. First, in the case of a single charged atom (ion), we propose a set of logical gates for quantum computation. Second, we use a macroscopic ensemble of neutral atoms as quantum memory for the storage of quantum entanglement to be used in fundamental studies of the process of superradiance. The first part of this thesis is a theoretical work with experimental perspectives. The traditional platform for the development of quantum computing with a chain of ions confined in a Paul trap is based on the model introduced in 1995 by Cirac and Zoller (CZ). In this model the electronic levels describe the qubits and the collective vibrational modes act as mediators between the qubits. In order to help mitigate the problems of scalability, we have proposed a new architecture that is a true reversal of the CZ scheme. Our approach consists in using the internal degrees of freedom of a single ion as a mediator (bus) and harnessing the motion of ions as the unit of quantum information, which leads us to a continuous variables picture of the problem. In addition we developed a toolbox of quantum operations complete enough to achieve computational universality. In the second part of the thesis, we develop a study not only theoretical but also experimental using quantum memories in an atomic ensemble. The idea here is to use a set of atoms to store quantum information over a certain period of time. This stored information is originally packaged in a collective atomic mode, which could subsequently be extracted on demand in a light field, presenting non-classical correlations with a previously detected heralding field. The atomic medium used is a cloud of cold Rubidium atoms obtained from a magneto-optical trap, when the trap is off. The generation of photon pairs, correlated through interaction with the atoms, is done by implementing a "write-read" scheme inspired by the Duan-Lukin-Cirac-Zoller protocol for long-distance quantum communication. A characteristic of the photons that mediate these interactions is that they are narrowband enough to allow a direct study of the temporal shape of their wave packet. Through the analysis and theoretical modeling of this wave packet, we investigate the dynamics of extraction of the quantum information stored in the quantum memory of the atomic ensemble. We report an experimental finding of non-classical characteristics of superradiance by implementing the process not only with a single excitation, but also with two-photon Fock states. Specifically, this work presents the experimental measurement and the theoretical modeling of wave packets in both single-photon and two-photon superradiance regimes. This new step opens the way for the study of interactions between collective quantum memories and light modes in a regime of higher-order components of the electromagnetic field.

Keywords: Quantum computing. Ion trap. Superradiance.

Resumo

A capacidade de manipular coerentemente os sistemas quânticos permite uma ampla gama de aplicações no campo da informação quântica. Nesta tese vamos abordar duas aplicações da interação quântica entre luz e um meio atômico. Primeiro, no caso de um único átomo carregado (íon), propomos um conjunto de portas lógicas para a computação quântica. Em segundo lugar, usamos um ensemble macroscópico de átomos neutros como memória quântica para o armazenamento de emaranhamento quântico a fim de ser usado em estudos fundamentais do processo de superradiância. A primeira parte desta tese é um trabalho teórico com perspectivas experimentais. A plataforma tradicional para o desenvolvimento da computação quântica com uma cadeia de íons aprisionados em uma armadilha de Paul é baseada no modelo introduzido em 1995 por Cirac e Zoller (CZ). Neste modelo os níveis eletrônicos descrevem os qubits e os modos vibracionais coletivos atuam como mediadores entre os qubits. Para ajudar a mitigar os problemas de escalabilidade, temos proposto uma nova arquitetura que é uma verdadeira inversão do esquema CZ. Nossa abordagem consiste em usar os graus de liberdade internos de um único íon como um mediador (bus) e aproveitar o movimento dos íons como a unidade de informação quântica, o que nos leva a um quadro de variáveis contínuas do problema. Além disso, desenvolvemos uma caixa de ferramentas de operações quânticas completa o suficiente para alcançar a universalidade computacional. Na segunda parte da tese, desenvolvemos um estudo não só teórico, mas também experimental usando memórias quânticas em um ensemble atômico. A ideia aqui é usar um conjunto de átomos para armazenar informação quântica durante um certo período de tempo. Esta informação armazenada é originalmente anunciada por um modo atômico coletivo, o qual poderia ser posteriormente extraído 'a pedido' em um campo de luz, apresentando correlações não clássicas com um campo 'anunciante' previamente detectado. O meio atômico é uma nuvem de átomos frios de Rubídio obtida a partir de uma armadilha magneto-óptica, quando a armadilha está desligada. A geração de pares de fótons, correlacionados através da interação com os átomos, é feita através da implementação de um esquema de "escrita-leitura" inspirado no protocolo Duan-Lukin-Cirac-Zoller para comunicação quântica de longa distância. Uma característica dos fótons que mediam essas interações é que eles são banda estreita o suficiente para permitir um estudo direto da forma temporal de seu pacote de onda. Através da análise e modelagem teórica deste pacote de onda, investigamos a dinâmica de extração da informação quântica armazenada na memória quântica do ensemble atômico. Reportamos um achado experimental das características não-clássicas da superradiância, implementando o processo não apenas com uma única excitação, mas também com estados de Fock de dois fótons. Especificamente, este trabalho apresenta a medição experimental e a modelagem teórica de pacotes de onda em ambos os regimes de superradiância, de um único fóton e dois fótons. Este novo passo abre o caminho para o estudo das interações entre memórias quânticas coletivas e modos de luz em um regime de componentes de mais alta ordem do campo eletromagnético.

palavras-chave: Computação quântica. Armadilha de ions. Superradiância.

List of Figures

1 Energy level scheme of a single trapped ion. Ground state g and an excited state e are considered in a harmonic trap. Oscillator states are $0, 1, \ldots$. The laser frequency is ω_L and the qubit (transition) frequency is ω_0. Panel (a) shows $\delta = \omega_L - \omega_0 = \omega_t$, (b) when $\delta = \omega_L - \omega_0 = 0$ and (c) for $\delta = \omega_L - \omega_0 = -\omega_t$. 26

2 Spectrum of $^{40}Ca^{+}$ ion, showing carrier band, and red and blue sidebands with a detuning $\sim \pm 1$ MHz from the carrier frequency. 28

3 Bloch sphere 29

4 Bloch sphere picture of the target ion in a R_{phase} gate. (a) and (c) show the rotation $R_t^+\left(\frac{\pi}{\sqrt{2}}, 0\right)$, (b) and (d) correspond to $R_t^+\left(\pi, \frac{\pi}{2}\right)$. We can note that same rotations produce different effects depending on the state it is applied in. 33

5 Proposal of CVQC using the ion trap. (a) The CZ paradigm employs one or more motional modes of the quantum harmonic oscillator to mediate the interaction (the 'quantum bus') between pairs of qubits. In the original proposal, one motional mode is essentially employed as a two-level system. Increasing the size of the Hilbert space requires adding more ions to the physical system, reaching an exponential increase. (b) Our proposal utilizes the qubit as the quantum bus that allows vibrational modes to interact. Three harmonic oscillator form the Hilbert space available for manipulation. The size of the Hilbert space available is outright larger than in the CZ paradigm, although it increases only polynomially with the phonon cap number. 38

6 Toolbox of Gaussian operations available for the manipulation of the vibrational state of a single trapped ion. The desired quantum gate is selected by radiation frequency. With the exception of the Fourier transform operation $\hat{F}_s$ which needs monochromatic light with $\delta = 0$, all quantum gates require bichromatic radiation with $\delta_1 = -\delta_2 = \delta$. Possible values of detuning correspond to any of the: vibrational frequencies ω_s (continuous lines), double those frequencies (dashed lines), subtraction (dotted lines) or sum (dash-dot lines) of pairs of frequencies. The corresponding Gaussian operations are displacements $\hat{D}_s$, squeezers $\hat{S}_s$, beam splitters $\hat{I}_{ss'}$, and two-mode squeezers $\hat{E}_{ss'}$, respectively, where $s, s' \in \{a, b, c\}$. In choosing the ratio of vibrational frequencies, we have adopted the proportion $\omega_a : \omega_b : \omega_c = 7 : 5 : 4$. 47

7 Schematic description for photon-pair generation from a cold atomic ensemble. First the Write classical beam is applied on the cloud generating Field 1. After a programable time, the ensemble is illuminated by the Read beam, inducing the emmision of Field 2. 56

8 Two laser sources are used for all the beams in the experiment, which are locked in the cross-over between $F' = 1$ and $F' = 2$ and the cross-over between $F' = 1$ and $F' = 3$, tuning the frequencies by means of acusto-optical modulators. Write and read frequencies, related to the energy structure of ^{87}Rb, are depicted in red arrows. 57

9 Two-level system with fundamental state a and excited state b. Transition frequency ω_0. 67

10 Lambda configuration 71

11 Gaussian mode defined by the optical fiber 74

12 Reading process, a classical laser induce a superradiant emission of field 2. 76

13 A conceptual scheme for a general one-dimensional MOT with two counter-propagating beams with frequency ω and circular polarizations σ^+ and σ^- are shown. The separation between the Zeeman sub-levels m_F of the hyperfine energy level $F' = 1$ increases proportional to the magnetic field B, this field increases linearly from $z = 0$ in the positive and negative Z-axis directions. 90

14 Levels from principal quantum number 92

15 Fine structure of ^{87}Rb, example of levels 5s and 5p. When introducing the spin of the electron only 5p is going to split in two fine levels. 92

16 Hyperfine structure of levels 5s and 5p. We see that 5s turns into two hyperfine levels and 5p into 6 hyperfine levels. 93

17 Zeeman structure for Rb, levels $5^2S_{1/2}$, $5^2P_{1/2}$ and $5^2P_{3/2}$. It presents 8 Zeeman levels for $5^2S_{1/2}$, 8 for $5^2P_{1/2}$ and 16 for $5^2P_{3/2}$. 94
18 Hyperfine picture of λ configuration. In left panel, selected hyperfine levels to be used in configuration. 95
19 DLCZ scheme with linear polarizations. Write and Field 2 have vertical polarization, Read and Field 1 have horizontal polarizations. Field 1 and Field 2 have orthogonal polarizatons and are conjugated modes of a four-wave mixing process. 96
20 Λ configuration considering the Zeeman structure for linear polarizations. . 97
21 DLCZ scheme with circular polarizations. Write and Field 2 have Right-handed cricular polarization, Read and Field 1 have Left-handed cricular polarization. Field 1 and Field 2 have orthogonal polarizatons. 97
22 Λ configuration considering Zeeman structure for all possible circular polarizations, not only the 2 FWM processes we are interested in. 98
23 Rubidium spectrum obtained via saturated absorption measurement in a vapor cell of rubidium atoms at room temperature. It is empoyed as frequency reference of lasers TICO and TECO, which generate all beams of the experiment. 99
24 Rubidium scheme of energy levels showing transitions used for cooling and repumping lasers. In the case of the cooling and trapping system we employ lasers red detuned from the $F = 2 \rightarrow F' = 3$ transition. The repump laser is resonant with the $F = 1 \rightarrow F' = 2$ transition. 99
25 Experimental setup. TMD must be removed for standard DLCZ scheme. . 102
26 Experimental setup for the magneto-optical trap. 103
27 Timing for DLCZ scheme experiment, for both single-photon and two-photon generation. 107

28 Setup with linear polarizations. There is no optical pump. The half wave plate is placed to rotate the transmitted polarizations by 90°. 115
29 Characterization of first round of measurements, without optical pump and without intensity modulator as a function of p_1. Panel (a) shows TGR (twin generation rate), panel (b) is g_{12}, and (c) plots the conditional probability p_c. The actual measurement is realized with $p_1 = 0.0164$, highlighted on a blue vertical bar, where $p_c = 0.0951$, $g_{12} = 5.25$ and $TGR = 62.5$Hz. The region $p_1 \rightarrow 0$, where noise is dominant, is in orange background. The many-excitations region is in green. In the middle, there is the few (single or two) excitation regime with a blue background. 116
30 Single-photon wave packet, over 40 hours of measurement time, without optical pump and without intensity modulator. 119

31 Two-photon wave packet for the same data set of single-photon wave packet shown in Figure 30, considering only the time of the first of the two photons. 120
32 Two-photon wave packet as function of the time difference τ between the two emitted photons. 120
33 Optical pump process. σ^- transitions are induced for excitation in every Zeeman level of $F = 2$, however spontaneous emissions are not forced to be in any particular polarization, thus atoms tend to accumulate on the cyclic transition $F = 2, m_F = -2 \rightarrow F' = 3, m_F = -3$. 121
34 Λ configuration after optical pump. It pumps atoms to the $F = 2, m_F = -2$ state, which selects uniquely the other two states involved on the induced transitions by the chosen polarizations, σ^+ and σ^- for write and read beams, respectively. On the other hand, since we are considering a FWM process, the conjugated modes 1 and 2, are considered in the same transitions. 122
35 Study of the polarization of the atomic medium as a function of the $\lambda/2$ angle. Panel (a) shows the case without OP, (b) with two counter-propagating OP beams in orthogonal circular polarizations in the laboratory frame, and (c) with two counter-propagating σ^- OP beams in the laboratory frame. . 123
36 The action of write pulse polarizing the medium 124
37 Experimental setup using optical pump and circular polarizations in all beams. 125
38 Characterization of measurements with optical pump but without intensity modulator as a function of p_1. Panel (a) shows TGR (twin generetion rate). Panel (b) is g_{12}, and (c) plots the conditional probability p_c. The actual measurement is realized with $p_1 = 0.018$, highlighted on a blue vertical bar. Here $p_c = 0.063$, $g_{12} = 7.5$, $TGR = 38$ Hz. 126
39 Single-photon wave packet using optical pump but still without the intensity modulators. We have a short measurement, just for showing the lack of definition in Rabi flops, but at least without multiple frequency components. 126
40 Relation of optical depth on current of the optical amplifier for the trapping beams. 128
41 Single-photon wavepackets. Conditional probability $p_c(t)$ to detect a single photon on field 2 at time t once a single detection was registered on field 1, normalized by the total conditional probability P_c to detect a single-photon in field 2 at any time. (a) For $OD = 3.4$, wave packets for $I_R = 3.95$ mW (black curve) and $I_R = 1.76$ mW (red curve). (b) For $I_R = 3.95$ mW, wave packets for $OD = 3.4$ (black curve) and $OD = 2.0$ (red curve). The insets plot the corresponding theoretical curves according to Eq. 3.2.102. 128

42 Two-photon wavepackets with read pulse intensity $I_R = 3.95$ mW. Panels (a) and (b): Probability $p_{c1}(t_1)$ to detect the first photon of a pair on field 2 at t_1 conditioned on two detections on field 1, with an integration window of $\Delta t_1 = 0.5$ ns and normalized by the area P_{c1} of the curve. Panels (c) and (d): Probability $p_{c\tau}(\tau)$ of detecting a second photon on field 2 at time τ after the first detection shown on panels (a) and (b), respectively, and normalized by the area $P_{c\tau}$ of the curve. Data on panels (a) and (c) , with $OD = 3.4$, resulted from the same measurements as for the experimental black curves on Fig. 41. Panels (b) and (d), with $OD = 2.0$, came from the measurements of the red curve on Fig. 41b. Red curves are the theoretical fittings. 130
43 Level scheme and fields for two-photon superradiance. 132
44 Probabilities $P_{i,j}$ to detect j photons of field 2 conditioned on the detection of i photons in field 1 as a function of the probability p_1 to detect one photon in field 1. (a) Probabilities conditioned to one detection in field 1. (b) Probabilities conditioned to two detections on field 1. Circles, squares, and diamonds plot the probabilities for the detection of one, two, and three photons on field 2. The solid lines are linear fits. The black dashed line provide the value for the plateau of $P_{1,i}$, which is explicitly indicated as 0.0085 for (a) and 0.0170 for (b). The red and blue dashed lines gives the square and cube, respectively, of the black one. 134

List of Tables

1 Dipole matrix elements for transition $F = 1 \rightarrow F' = 2$ 95
2 Dipole matrix elements for transition $F = 2 \rightarrow F' = 2$ 96

Contents

1	**1 Introduction**	**16**
1.1	Overview	16
1.2	Outline of the thesis	17
2	**2 Continuous variables quantum computation**	**19**
2.1	Quantum computation over the internal degrees of freedom	19
2.1.1	*Quantum description of the ion motion in a trap*	20
2.1.2	*Hamiltonian*	22
2.1.3	*Qubits with trapped ions*	27
2.1.4	*Single qubit operations*	28
2.1.5	*Two-qubit operations - The Cirac-Zoller approach*	30
2.2	Quantum computation over the vibrational modes	37
2.2.1	*Basic implementation*	38
2.2.2	*Bichromatic CV quantum gates*	42
2.2.3	*Ion trap CVQC toolbox*	47
3	**3 Single-photon generation from an atomic ensemble**	**53**
3.1	Photon-pairs from the DLCZ-protocol scheme	55
3.1.1	*Single-photon generation for DLCZ*	55
3.1.2	*Operation of the DLCZ single-photon generator*	56
3.1.3	*Non-classical nature of states in DLCZ*	58
3.2	Single-photon superradiance	65
3.2.1	*Hamiltonian for atom-field interaction*	66
3.2.2	*Two-level atom*	67
3.2.3	*Spontaneous emission in 2-level atoms (Weisskopf-Wigner Theory)*	68
3.2.4	*Collective quantum memory*	70
3.2.5	*Uniform excitation approximation*	81
3.2.6	*Wave function of the emitted photon in the reading process*	83
3.2.7	*Superradiant amplification*	85
3.2.8	*Next step*	88
4	**4 Experimental apparatus**	**89**

4.1 Creation of the atomic ensemble . . . 91
4.1.1 *Structure of energy levels* . . . 91
4.1.2 *Atom source* . . . 98
4.1.3 *Lasers: Doppler cooling and repumping* . . . 98
4.1.4 *Magnetic trapping* . . . 100
4.1.5 *Vacuum system* . . . 100
4.2 Experimental setup for the write-read process . . . 104
4.2.1 *Setup* . . . 104
4.2.2 *Pulse system* . . . 108

5 5 Heralded two-photon generation 112
5.1 Measurement implementations . . . 113
5.2 Without optical pump . . . 114
5.3 Optical pump . . . 121
5.4 With optical pump but without intensity modulator . . . 124
5.5 With optical pump and with intensity modulator . . . 127
5.6 Theoretical model for two-photon superradiance . . . 131
5.7 Suppression of higher order components . . . 132

6 6 Conclusions 136
6.1 Continuous variables quantum computation . . . 136
6.2 Two-photon superradiance . . . 137

References 138

1 Introduction

1.1 Overview

Quantum mechanics is the field of physics which is dedicated to understanding the universe on the atomic scale. Fundamental particles as atoms and photons obey the laws of quantum mechanics and the probability distribution for the outcome of each possible measurement on the system is provided by the quantum state or a superposition of quantum states. For more than six decades, quantum (coherent) superposition states have been studied and used in applications such as photon interferometry and Ramsey spectroscopy [1]. However, entangled states, specifically those 'engineered' for specific tasks, have become completely accessible only in the last three decades. One of the main achievements in this area were the early experiments of non-locality in quantum mechanics [2] performed with pairs of entangled photons [3, 4]. Moreover, making use of the quantum properties of fundamental particles, systems to transmit and process (quantum) information can be built, which is the basis of what is called quantum communication and quantum computation, respectively. As the technology is being miniaturized and electronics is approaching the fundamental scale, the potential of these areas is becoming more and more important and a detailed theory of quantum information processing has been rapidly and steadly developed in the last twenty years. Simple quantum algorithms and a wide variety of quantum communication protocols [5–9] have also been demonstrated experimentally, including quantum teleportation and quantum cryptography.

Quantum information comes in two forms, discrete and continuous. The best-known example of continuous variables quantum information [10–12] is the quantized harmonic oscillator, which can be described by continuous variables such as position and momentum (an alternative description is the discrete but infinite-dimensional representation in terms of energy states). Examples of continuous-variable quantum systems include quantized modes of bosonic systems such as the different degrees of freedom of the electromagnetic field, vibrational modes of solids, atomic ensembles, nuclear spins in a quantum dot, Josephson junctions, and Bose-Einstein condensates. Because they provide the quantum description of the propagating electromagnetic field, continuous-variable quantum systems are particularly significant for quantum communication [13] and quantum-limited

techniques for detection, sensing, and imaging [14, 15]. Although encoding of continuous-variable systems in solid-state or atomic media are used for quantum computation [16], bosonic systems are important not only in the physical modeling of discrete-variable quantum computation, e.g., the quantized vibrational modes of ions embody the quantum bus between qubits in ion-trap quantum computers, but also allows for new approaches to quantum computation, as can be verified in the chapter 2. On the other hand, the best-known example of discrete quantum information is the quantum bit or 'qubit', a quantum system with two distinguishable states. Examples of quantum systems that can be used to register a qubit are spin-1/2 particles such as nuclear spins [17], the two lowest energy states of semiconductor quantum dots [18] or quantized superconducting circuits [19], the two polarization states of a single photon [20], and the the electronic levels of a two-level atom as is going to be studied in the second part of this thesis, i.e. chapters 3, 4 and 5, where single-photon and two-photon storage of quantum information is studied as well as the phenomenon of superradiance in these two regimes.

In this thesis we will study quantum information processing in the two forms described above, i.e. in continuous variables and in discrete variables regime. In the first case, when we treat the situation of an ion trapped in a Paul trap, we will see how the motion of the ion is quantized and can be coherently manipulated, not just to write, but also process some amount of quantum information. Since motion is a continuous quantum variable, then we are going to use a mathematical approach and treatment that is characteristic of continuous variables quantum information. In the second part of the thesis we will experimentally study the situation of a large ensemble of neutral atoms, which are also trapped, however in a magneto-optical trap. This set of atoms is used to store quantum information for a period of time. For this reason this implementation is called a "quantum memory". The quantum information in this case is written via an electronic energy transition, which can only lead to one of two possible states, fundamental or excited, and therefore it must be studied using tools of discrete variables quantum information. The quantum state before and after the quantum memory is written in a light beam, so this device is very interesting for quantum communication systems with photons.

1.2 Outline of the thesis

In chapter 2 we propose the architecture of a quantum processor based on a single trapped ion as well as a toolbox of quantum operations in continuous variables to achieve computational universality. In chapter 3 we explain a theoretical framework for the understanding of some cooperative effects in atomic systems, focusing mainly on the single-photon superradiance process. The assembly of the magneto-optical trap and the experimental setup concerning the measurement of two-photon superradiance in cold rubidium atoms is detailed in chapter 4. In chapter 5 the main experimental results found in relation to

the two-photon superradiance as well as some characterizations that are important for the interpretation of the experimental data are presented. Finally the conclusions are presented in chapter 6, regarding the two topics addressed in the thesis.

2 Continuous variables quantum computation

In this chapter we are going to propose an architecture for a quantum processor based on the motional modes of a trapped ion in a Paul trap. We focus not only on the theoretical model, but also on the experimental details needed for an eventual implementation. The first section is oriented to establish the present point of view of discrete variables quantum computation as proposed by Cirac and Zoller in 1995 [21], and which has inspired the majority of the improvements in this area in the last 20 years. We explain in detail the CZ gate which represents the core of this paradigm, and will be our starting point for the rest of the chapter. After that, we explain how that paradigm can be inverted, using the internal degrees of freedom not for storing units of quantum information but just as a mediator, and on the other hand, using the vibrational states of the single trapped ion as the actual information unit, and not as a mediator. In summary it is an inversion of the original proposal. The motivation of this new point of view is explained at the final sections of the chapter, since we appeal to the use of an smaller physical size accessing a larger Hilbert space.

2.1 Quantum computation over the internal degrees of freedom

A quantum processor consists of a collection of interacting quantum bits which can be independently manipulated and measured. There are some platforms to embody it, however ion traps have stood as one of the most successful experimental implementations, since requirements for computation universality [22–24] have been experimentally demonstrated. On the other hand, scalability [25, 26] showed to be a fundamental challenge for quantum processors.

An ion chain works as a quantum register wherein each pair of energy eigenstates of the ion's electronic configuration encodes one qubit [21]. The electric repulsion among ions and the external confinement give rise to collective modes of vibration which are employed as mediators when any chosen pair of qubits are interacting. Resonant or near-resonant lasers, with the qubit transitions, are used to carry out the quantum operations. Other internal energy levels of the ions are employed to initialize and measure the qubits. Despite the enormous evolution since the dawn of this scheme [23, 27–30], it would not

be inappropriate to name it as the 'Cirac & Zoller (CZ) paradigm' of ion trap quantum computing since it is based on a theoretical proposal of 1995 by Ignacio Cirac and Peter Zoller. To sum up, the CZ paradigm conceives each ion as a storage unit for a single qubit in internal electronic energy levels, with one or more vibrational modes mediating interactions among different qubits.

2.1.1 *Quantum description of the ion motion in a trap*

Let's start by assuming that the potential is quadratic in the three coordinates of the center of mass of the trapped ion [31], so the problem can be separated into three one-dimensional problems. Once in the one-dimensional situation, we substitute the x-coordinate with the operator $\hat{x}$ and so we can write the time-dependent potential operator

$$\hat{V}(t) = \frac{m}{2} W(t)\, \hat{x}^2,$$

where

$$W(t) = \frac{\omega_{\mathrm{rf}}^2}{4} \left[a_x + 2q_x \cos\left(\omega_{\mathrm{rf}} t\right)\right],$$

comes from the equation of Mathieu for a Paul trap

$$\frac{d^2x}{d\xi^2} + \left[a_x - 2q_x \cos\left(2\xi\right)\right] x = 0, \tag{2.1.1}$$

which belongs to a general class of differential equations with periodic coefficients. The general form of its stable solutions comes from the Floquet theorem [32, 33]

$$x(\xi) = Ae^{i\beta_x \xi} \sum_{n=-\infty}^{\infty} C_{2n} e^{i2n\xi} + Be^{-i\beta_x \xi} \sum_{n=-\infty}^{\infty} C_{2n} e^{-i2n\xi}. \tag{2.1.2}$$

Where the real characteristic exponents β_x and the coefficients C_{2n} are functions only of a_x and q_x and do not depend on the initial conditions. We also have to note that the independent variable ξ, according to the theoretical model describing Paul's trap, is the one that carries the temporal dependence, $\xi = \omega_{\mathrm{rf}} t/2$.

However, we will not delve into the origin of this function since it escapes the objectives of this thesis and rather concerns the construction of the trap and its quadrupolar potential. What is of vital importance is its interpretation, therefore we are going to imagine that the particle is in a sort of harmonic oscillator potential, but instead with another elastic constant (normally it is chosen ω^2), and also variable in time.

With all of the above, we are in a position to construct the Hamiltonian motion for the ion in the trap, which will be very similar to the known Hamiltonian of a harmonic oscillator.

$$\hat{H}^{(m)} = \frac{\hat{p}^2}{2m} + \frac{m}{2} W(t)\,\hat{x}^2. \tag{2.1.3}$$

Immediately we can deduce the equations of motion associated with this Hamiltonian, in the Heisenberg picture:

$$\dot{\hat{x}} = \frac{1}{i\hbar}\left[\hat{x}, \hat{H}^{(m)}\right] = \frac{\hat{p}}{m},$$

$$\dot{\hat{p}} = \frac{1}{i\hbar}\left[\hat{p}, \hat{H}^{(m)}\right] = -mW(t)\,\hat{x}.$$

These equations of motion clearly satisfy

$$\ddot{\hat{x}} + W(t)\,\hat{x} = 0,$$

which is equivalent to Mathieu's equation (2.1.1). Let us also consider the same equation but substituting $\hat{x}$ by $u(t)$. This is useful to find solutions by employing a special solution of the Mathieu equation in the variable u considering the boundary conditions $u(0) = 1$ and $\dot{u}(0) = i\omega_t$. This solution can be obtained through equation (2.1.2) with $A = 1$ and $B = 0$,

$$u(t) = Ae^{i\beta_x \xi} \sum_{n=-\infty}^{\infty} C_{2n} e^{i2n\xi}. \tag{2.1.4}$$

Remembering the parameter $\xi = \omega_{\mathrm{rf}} t/2$ we must find a solution that is of the type

$$u(t) = e^{i\beta_x \omega_{\mathrm{rf}} t/2} \Phi(t),$$

being $\Phi(t)$ a periodic function with period $T = 2\pi/\omega_{\mathrm{rf}}$.

In this way the boundary conditions become

$$u(0) = \sum_{n=-\infty}^{\infty} C_{2n} = 1$$

and

$$\omega_t = \omega_{\mathrm{rf}} \sum_{n=-\infty}^{\infty} C_{2n}(\beta_x/2 + n).$$

This solution and its complex conjugate are linearly independent, so that they respond to the Wronskian identity

$$\begin{aligned} u^*(t)\,\dot{u}(t) - u(t)\,\dot{u}^*(t) &= u^*(0)\,\dot{u}(0) - u(0)\,\dot{u}^*(0) \\ &= 2i\omega_t. \end{aligned}$$

As the coordinates being studied $\hat{x}(t)$ and $u(t)$ satisfy the same differential equation, then the following linear combination

$$\hat{C}(t) = \sqrt{\frac{m}{2\hbar\omega_t}} i \left[u(t)\,\dot{\hat{x}}(t) - \dot{u}(t)\,\hat{x}(t) \right] \tag{2.1.5}$$

is proportional to its Wronskian identity and also constant over time

$$\hat{C}(t) = \hat{C}(0) = \frac{1}{\sqrt{2m\hbar\omega_t}} \left[m\omega_t \hat{x}(0) + i\hat{p}(0) \right].$$

Even more, the right side of the equation is exactly the definition of the annihilation operator for a static potential of harmonic oscillator of mass m and frequency ω_t

$$\hat{C}(t) = \hat{C}(0) = \hat{a},$$

what immediately implies in the commutation relation $\left[\hat{C}, \hat{C}^\dagger\right] = \left[\hat{a}, \hat{a}^\dagger\right] = 1$. This static potential oscillator will be named as reference oscillator from now on.

Finally we know that operators $\hat{x}(t)$ and $\hat{p}(t)$, in the Heisenberg picture, can be restated in terms of $u(t)$ and the reference oscillator operators. Using equation (2.1.5):

$$\hat{x}(t) = \sqrt{\frac{\hbar}{2m\omega_t}} \left[\hat{a}u^*(t) + \hat{a}^\dagger u(t) \right], \tag{2.1.6}$$

$$\hat{p}(t) = \sqrt{\frac{\hbar m}{2\omega_t}} \left[\hat{a}\dot{u}^*(t) + \hat{a}^\dagger \dot{u}(t) \right]. \tag{2.1.7}$$

So that all temporal dependence is given by the special solution $u(t)$ and its complex conjugate.

2.1.2 *Hamiltonian*

When we work with strongly trapped atoms, we have the possibility of coherently manipulating an internal electronic state using another internal state or states of motion, through the application of appropriate electromagnetic fields. In this section we consider the trapped ions in a very reasonable approximation as if they were two-level systems, with levels g and e and energy difference $\hbar\omega_0 = \hbar(\omega_e - \omega_g)$ [34, 35]. This approximation is appropriate if at least two fundamental conditions are met: the frequency of the light producing the coupling is very close to the resonance for two internal levels, and if the Rabi frequencies that describe the coupling strength are considerably smaller than the relative detuning to other transitions close to the resonance. In this way we describe the

Hamiltonian of the free atom under the approximation of a two-level system

$$\begin{aligned}\hat{H}^{(e)} &= \hbar\left(\omega_g \left|g\right\rangle\left\langle g\right| - \omega_e \left|e\right\rangle\left\langle e\right|\right) \\ &= \hbar\frac{\omega_g+\omega_e}{2}\left(\left|g\right\rangle\left\langle g\right| + \left|e\right\rangle\left\langle e\right|\right) + \hbar\frac{\omega_0}{2}\left(\left|g\right\rangle\left\langle g\right| - \left|e\right\rangle\left\langle e\right|\right).\end{aligned}$$

Since we are in a two-level system approximation, the operators we are using can be mapped on a spin-1/2 operator basis, with their respective algebra, which is represented by the identity (2×2) and the three Pauli matrices:

$\hat{I} \longleftrightarrow \left\|g\right\rangle\left\langle g\right\| + \left\|e\right\rangle\left\langle e\right\|$	$\hat{\sigma}_x \longleftrightarrow \left\|g\right\rangle\left\langle e\right\| + \left\|e\right\rangle\left\langle g\right\|$
$\hat{\sigma}_y \longleftrightarrow i\left(\left\|g\right\rangle\left\langle e\right\| - \left\|e\right\rangle\left\langle g\right\|\right)$	$\hat{\sigma}_z \longleftrightarrow \left\|e\right\rangle\left\langle e\right\| - \left\|g\right\rangle\left\langle g\right\|$

In this way the Hamiltonian is expressed in terms of the identity and the Pauli matrix $\hat{\sigma}_z$:

$$\hat{H}^{(e)} = \hbar\frac{\omega_g+\omega_e}{2}\hat{I} + \hbar\frac{\omega_0}{2}\hat{\sigma}_z,$$

where the first term is an energy contribution independent of the state. Therefore the Hamiltonian can be rescaled by this quantity $\hat{H}^{(e)} \to \hat{H}^{(e)} - \hbar\frac{\omega_g+\omega_e}{2}\hat{I}$ without losing its physical interpretation:

$$\hat{H}^{(e)} = \hbar\frac{\omega_0}{2}\hat{\sigma}_z. \tag{2.1.8}$$

In the later theoretical treatment, it is important to note that the light fields to be used are being considered in the lowest order of their multipolar expansion, i.e., for dipole-allowed transitions we will consider the dipolar approximation, whereas for dipole-forbidden transitions we will only consider the quadrupole component. For Raman transitions, the near resonant intermediate state is to be eliminated adiabatically, so that these transitions are to be considered equivalent to other two-level transitions.

Finally we will introduce the interaction Hamiltonian, which corresponds to the interaction with an additional electromagnetic field applied to the ion. For simplicity we are only considering the case where we have a single ion, a single applied field and a single motional mode.

The electromagnetic field is assumed to be classical, periodically variable in time and propagating in the x direction. This field is applied on an ion that is only free to oscillate in the z axis with a frequency ω_z. If we assume that the internal levels of the atom are coupled by electric fields, then the interaction Hamiltonian is [36]

$$\hat{H}^{(i)} = -\hat{\vec{d}}\cdot\hat{\vec{E}}\left(x,t\right), \tag{2.1.9}$$

where $\hat{\vec{d}}$ is the electric dipole operator for the internal transition and $\hat{\vec{E}}\left(x,t\right)$ comes from the propagation of the uniform wave along the x-axis and with polarization in the z-

direction. Considering $\hat{x}_s$ as the coordinate operator in the Schrödinger picture we have

$$\begin{aligned}\hat{\vec{E}} &= \vec{E}_z \cos\left(k\hat{x}_s - \omega_L t + \varphi\right) \\ &= \frac{\vec{E}_z}{2}\left(e^{i(k\hat{x}_s-\omega_L t+\varphi)} + e^{-i(k\hat{x}_s-\omega_L t+\varphi)}\right),\end{aligned}$$

being ω_L the optical frequency, k the modulus of the wavevector, fulfilling $k = {}^{2\pi}/_{\lambda}$, and λ the wavelength.

The atomic dipole moment operator is given by $\hat{\vec{d}} = -e\hat{\vec{r}} = -\vec{d}_{ge}\,(ge + eg)$, where e is the electron's charge, $\vec{r}$ is the relative coordinate of valence electron, $\vec{d}_{ge}$ is a real numbered vector (not an operator) with direction given by the dipole polarization axis, i.e. z-direction, and the magnitude given by the dipole matrix element for the transition between g and e. The matrix elements d_{ge} can be calculated by using the Wigner-Eckart theorem and the Clebsch-Gordan coefficients for the atomic transitions. So we can state that

$$\hat{\vec{d}} = -\frac{\vec{d}_{ge}}{2}\left(\hat{\sigma}_+ + \hat{\sigma}_-\right)$$

so that

$$H^{(i)} = -\hat{\vec{d}}\cdot\hat{\vec{E}}\,(x,t) = \hbar\Omega\left(\hat{\sigma}_+ + \hat{\sigma}_-\right)\left(e^{i(k\hat{x}_s-\omega_L t+\varphi)} + e^{-i(k\hat{x}_s-\omega_L t+\varphi)}\right), \tag{2.1.10}$$

where $\hbar\Omega \equiv -\frac{d_{ge}E_z}{4}$, $\hat{\sigma}_+ \equiv \hat{\sigma}_x + i\hat{\sigma}_y$ and $\hat{\sigma}_- \equiv \hat{\sigma}_x - i\hat{\sigma}_y$. We will also assume that the lifetimes of the levels are long, i.e., the spectrum of transitions excited by the wave is well resolved if Ω is small enough.

Now we are in a position to write our total Hamiltonian as the sum of the three Hamiltonians that we have been studying so far (Eqs. 2.1.3, 2.1.8 and 2.1.10),

$$\hat{H} = \hat{H}^{(m)} + \hat{H}^{(e)} + \hat{H}^{(i)}. \tag{2.1.11}$$

The simplest view of this dynamics, induced by the introduction of the light field, is given by the interaction picture with the free Hamiltonian $\hat{H}_0 = \hat{H}^{(m)} + \hat{H}^{(e)}$ and the interaction $\hat{V} = \hat{H}^{(i)}$.

With $\hat{U}_0 = \exp\left[-\left({}^{i}/_{\hbar}\right)\hat{H}_0 t\right]$, the transformed interaction Hamiltonian is:

$$\begin{aligned}\hat{H}_{int} &= \hat{U}_0^{\dagger}\hat{H}^{(i)}\hat{U}_0 \\ &= \hbar\Omega e^{(i/\hbar)\hat{H}^{(e)}t}\left(\hat{\sigma}_+ + \hat{\sigma}_-\right)e^{-(i/\hbar)\hat{H}^{(e)}t} \\ &\quad\times e^{(i/\hbar)\hat{H}^{(m)}t}\left[e^{i(k\hat{x}_s-\omega_L t+\varphi)} + e^{-i(k\hat{x}_s-\omega_L t+\varphi)}\right]e^{-(i/\hbar)\hat{H}^{(m)}t}\end{aligned}$$

First we are going to develop the part of the electronic Hamiltonian. Here we find two

terms that are going to be solved in an analogous way. Therefore we are going to develop in detail only the solution for one of them:

$$\hbar\Omega e^{(i/\hbar)\hat{H}^{(e)}t}\hat{\sigma}_+ e^{-(i/\hbar)\hat{H}^{(e)}t}.$$

This expression can be rewritten through the Baker-Campbell-Hausdorf formula, $e^A B e^{-A} = B + [A,B] + 1/2[A,[A,B]] + \ldots$, and making use of the algebra of the ladder operators $[\hat{\sigma}_z, \hat{\sigma}_\pm] = \pm 2\hat{\sigma}_\pm$, thus

$$e^{(i/\hbar)\hat{H}^{(e)}t}\hat{\sigma}_+ e^{-(i/\hbar)\hat{H}^{(e)}t} = \hat{\sigma}_+ \left(1 + i\omega_0 t + \ldots\right) = \hat{\sigma}_+ e^{i\omega_0 t},$$

and similarly for $\hat{\sigma}_-$, in such a way that we can already write the Hamiltonian as

$$\hat{H}_{int} = \hbar\Omega \left(\hat{\sigma}_+ e^{i\omega_0 t} + \hat{\sigma}_- e^{-i\omega_0 t}\right) e^{(i/\hbar)\hat{H}^{(m)}t} \left[e^{i(k\hat{x}-\omega_L t+\varphi)} + e^{-i(k\hat{x}-\omega_L t+\varphi)}\right] e^{-(i/\hbar)\hat{H}^{(m)}t}.$$

Now we apply the Rotating Wave Approximation (RWA). When we multiply the factors that contain the temporal dependence, we find terms of the type $\exp\left[\pm i\left(\omega_L \pm \omega_0\right)t\right]$. Here there are two terms corresponding to the sum of the frequencies $\omega_L + \omega_0$ and two other terms that come from the subtraction of the frequencies $\delta = \omega_L - \omega_0$. In this way, the fast terms, coming from the sum of frequencies, can be neglected, since they are hardly going to affect in any way the temporal evolution of the system:

$$\begin{aligned}
\hat{H}_{int} &= \hbar\Omega \left(\hat{\sigma}_+ e^{i\omega_0 t} + \hat{\sigma}_- e^{-i\omega_0 t}\right) e^{(i/\hbar)\hat{H}^{(m)}t} \left[e^{i(k\hat{x}-\omega_L t+\varphi)} + e^{-i(k\hat{x}-\omega_L t+\varphi)}\right] e^{-(i/\hbar)\hat{H}^{(m)}t} \\
&= \hbar\Omega\hat{\sigma}_+ e^{i\omega_0 t} e^{(i/\hbar)\hat{H}^{(m)}t} e^{i(k\hat{x}-\omega_L t+\varphi)} e^{-(i/\hbar)\hat{H}^{(m)}t} \\
&\quad + \cancel{\hbar\Omega\hat{\sigma}_+ e^{i\omega_0 t} e^{(i/\hbar)\hat{H}^{(m)}t} e^{-i(k\hat{x}-\omega_L t+\varphi)} e^{-(i/\hbar)\hat{H}^{(m)}t}} \\
&\quad + \cancel{\hbar\Omega\hat{\sigma}_- e^{-i\omega_0 t} e^{(i/\hbar)\hat{H}^{(m)}t} e^{i(k\hat{x}-\omega_L t+\varphi)} e^{-(i/\hbar)\hat{H}^{(m)}t}} \\
&\quad + \hbar\Omega\hat{\sigma}_- e^{-i\omega_0 t} e^{(i/\hbar)\hat{H}^{(m)}t} e^{-i(k\hat{x}-\omega_L t+\varphi)} e^{-(i/\hbar)\hat{H}^{(m)}t} \\
&= \hbar\Omega e^{-i[\delta t-\varphi]} + \hat{\sigma}_+ e^{(i/\hbar)\hat{H}^{(m)}t} e^{ik\hat{x}} e^{-(i/\hbar)\hat{H}^{(m)}t} \\
&\quad + \hbar\Omega e^{i[\delta t-\varphi]} + \hat{\sigma}_- e^{(i/\hbar)\hat{H}^{(m)}t} e^{-ik\hat{x}} e^{-(i/\hbar)\hat{H}^{(m)}t}
\end{aligned}$$

Now, we focus on the second part of the Hamiltonian, which concerns the Hamiltonian of motion in the interaction picture. We see that it is equivalent to have carried this Hamiltonian from the Schrödinger picture to the Heisenberg picture. In this way, the operator $\hat{x}_S$ will be replaced by the operator $\hat{x}\,(t)$, in the Heisenberg picture, as shown in equation (2.1.6):

$$e^{(i/\hbar)\hat{H}^{(m)}t} e^{\pm ik\hat{x}} e^{-(i/\hbar)\hat{H}^{(m)}t} = e^{\pm ik\hat{x}(t)}. \tag{2.1.12}$$

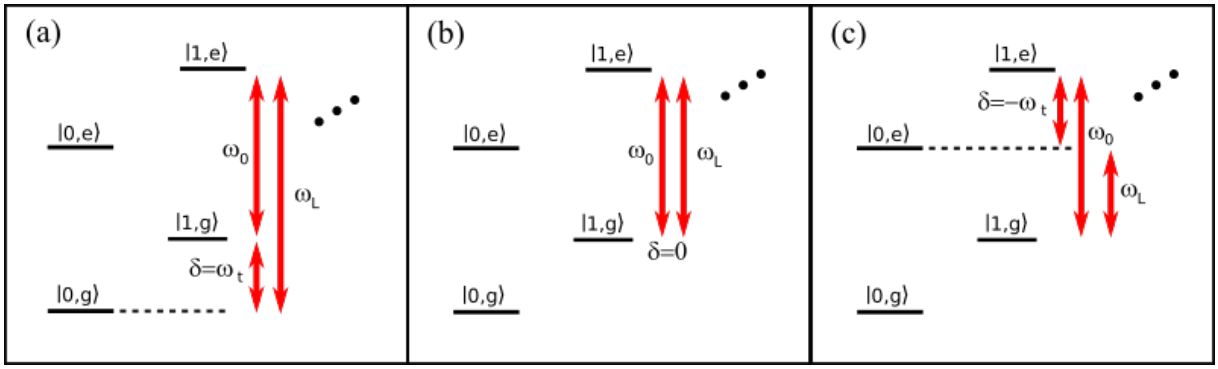

Figure 1: Energy level scheme of a single trapped ion. Ground state g and an excited state e are considered in a harmonic trap. Oscillator states are $0, 1, \ldots$. The laser frequency is ω_L and the qubit (transition) frequency is ω_0. Panel (a) shows $\delta = \omega_L - \omega_0 = \omega_t$, (b) when $\delta = \omega_L - \omega_0 = 0$ and (c) for $\delta = \omega_L - \omega_0 = -\omega_t$.

We now introduce the Lamb-Dicke parameter $\eta = kx_0$, which gives the ratio between the typical length scale of the ion's oscillation amplitude and the projection of the wavelength of the incident laser radiation, where $x_0 = \sqrt{\hbar/2m\omega_t}$ is the extension along the x-axis of the ground state wave function of the reference oscillator. In this way we obtain that

$$k\hat{x}\left(t\right) = \eta\left[\hat{a}u^{*}\left(t\right) + \hat{a}^{\dagger}u\left(t\right)\right],$$

such that

$$e^{(i/\hbar)\hat{H}^{(m)}t}e^{\pm ik\hat{x}}e^{-(i/\hbar)\hat{H}^{(m)}t} = e^{\pm i\eta\left[\hat{a}u^{*}(t)+\hat{a}^{\dagger}u(t)\right]}.$$

Inserting this into the previous Hamiltonian:

$$\hat{H}_{int}\left(t\right) = \hbar\Omega\hat{\sigma}_{+}e^{-i[\delta t-\varphi]}\exp\left(i\eta\left[\hat{a}u^{*}\left(t\right) + \hat{a}^{\dagger}u\left(t\right)\right]\right) + H.c.$$

Remembering the form of the solution (2.1.4), and considering some approximations that fit the usual experimental conditions, as$(|a_x|, q_x^2) \ll 1$, so that $\beta_x\omega_{\mathrm{rf}} \approx \omega_t$ and $C_0 \approx (1 + q_x/2)^{-1}$, we can write a more simplified form of the function $u\left(t\right)$ to be used in the Hamiltonian

$$u\left(t\right) \approx \frac{e^{i\omega_t t}}{1 + q_x/2}.$$

In addition, we are now going to rescale the interaction strength $\Omega \to \Omega\left(1 + q_x/2\right)$, in such a way that the interaction Hamiltonian takes a simpler form

$$\hat{H}_{int}\left(t\right) = \hbar\Omega\hat{\sigma}_{+}e^{-i[\delta t-\varphi]}\exp\left(i\eta\left[\hat{a}e^{-i\omega_t t} + \hat{a}^{\dagger}e^{i\omega_t t}\right]\right) + H.c.. \tag{2.1.13}$$

2.1.3 *Qubits with trapped ions*

Using the Lamb-Dicke approximation ($\eta\sqrt{\langle\hat{a}+\hat{a}^\dagger\rangle} \ll 1$), we can rewrite Eq. (2.1.13) by expanding the exponential [34, 37]:

$$\exp\left(\pm i\eta\left[\hat{a}e^{-i\omega_t t}+\hat{a}^\dagger e^{i\omega_t t}\right]\right) \approx 1 \pm i\eta\left[\hat{a}e^{-i\omega_t t}+\hat{a}^\dagger e^{i\omega_t t}\right].$$

Such an approximation requires that the coupling between the qubit and the collective vibration mode of the ions should be sufficiently weak. Thus,

$$\begin{aligned}\hat{H}_{int}(t) =& \hbar\Omega\left\{\hat{\sigma}_+ e^{-i(\delta t-\varphi)}\left(1+i\eta\left[\hat{a}e^{-i\omega_t t}+\hat{a}^\dagger e^{i\omega_t t}\right]\right)+\hat{\sigma}_- e^{i(\delta t-\varphi)}\left(1-i\eta\left[\hat{a}e^{-i\omega_t t}+\hat{a}^\dagger e^{i\omega_t t}\right]\right)\right\}\\ & \hbar\Omega\left\{\hat{\sigma}_+ e^{-i(\delta t-\varphi)}+\hat{\sigma}_- e^{i(\delta t-\varphi)}+\left(\hat{\sigma}_+ e^{-i(\delta t-\varphi)}-\hat{\sigma}_- e^{i(\delta t-\varphi)}\right) i\eta\left[\hat{a}e^{-i\omega_t t}+\hat{a}^\dagger e^{i\omega_t t}\right]\right\}.\end{aligned}$$

Three cases of the laser detuning δ are of particular interest (see Fig. 1): $\delta = 0$ and $\delta = \pm\omega_t$. This becomes apparent if a second rotating wave approximation is carried out where time dependent terms for the three cases above are discarded:

1. the Hamiltonian describing the carrier transition ($\delta = 0$):

$$\hat{H}_{car} = \hbar\Omega\left(\sigma_+ e^{i\varphi}+\sigma_- e^{-i\varphi}\right) \tag{2.1.14}$$

   Here only the electronic states $|g\rangle$ and $|e\rangle$ of the ion are changed (carrier transitions).

2. the Hamiltonian describing the blue sideband transition ($\delta = \omega_t$):

$$\hat{H}_+ = i\hbar\Omega\eta\left(\sigma_+\hat{a}^\dagger e^{i\varphi}-\sigma_-\hat{a}e^{-i\varphi}\right). \tag{2.1.15}$$

   Simultaneously to exciting the electronic state of the ion, in this case a motional quantum (a phonon) is created. Within this two-level system, Rabi flopping with the Rabi frequency

$$\Omega_{n,n+1} = \sqrt{n+1}\eta\Omega \tag{2.1.16}$$

   occurs, where n describes the number of motional quanta (phonons). For convenience, we define the blue sideband Rabi frequency $\Omega_+ = \Omega_{0,1}$ which describes the flopping frequency between the $|g,0\rangle$ and the $|e,1\rangle$ state.

3. the Hamiltonian describing the red sideband transition ($\delta = -\omega_t$):

$$\hat{H}_- = i\hbar\Omega\eta\left(\sigma_-\hat{a}^\dagger e^{-i\varphi}+\sigma_+\hat{a}e^{i\varphi}\right). \tag{2.1.17}$$

   Simultaneously to exciting the electronic state, here a phonon is destroyed, and Rabi flopping with the Rabi frequency

$$\Omega_{n,n-1} = \sqrt{n}\eta\Omega \tag{2.1.18}$$

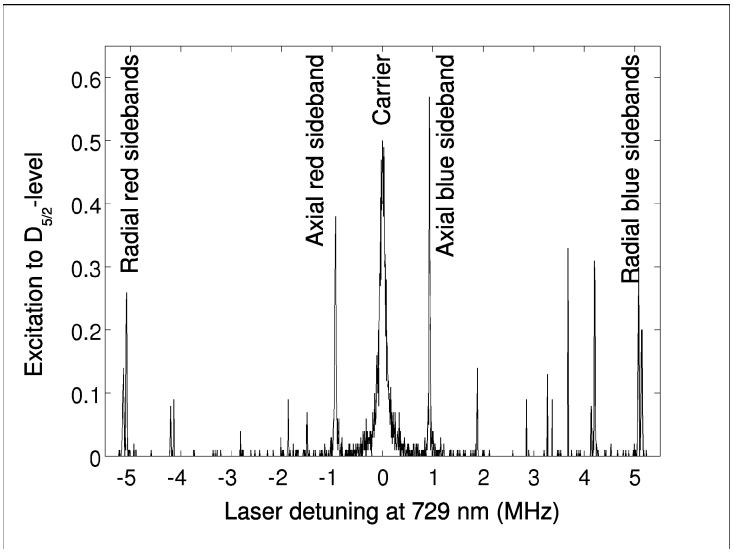

Figure 2: Spectrum of $^{40}Ca^{+}$ ion, showing carrier band, and red and blue sidebands with a detuning $\sim \pm 1$ MHz from the carrier frequency.

takes place.

In Fig. 2 we can see an experimental spectrum of a single trapped $^{40}Ca^{+}$ ion near the qubit transition (experiment from [35]). When the laser frequency is in resonance with the qubit transition ($\delta = 0$), we can clearly observe the strong carrier transition, as well as the blue ($\delta = \omega_t$) and red ($\Delta\delta = -\omega_t$) sidebands, corresponding to Eqs. 2.1.14, 2.1.15 and 2.1.17, respectively. The motional frequencies of the single ion can be deduced from the spectrum to amount to $\omega_z \approx 2\pi \times 1$ MHz (axial frequency) and $\omega_{r_{x,y}} \approx 2\pi \times 5$ MHz (radial frequencies), since in sidebands the laser detuning is ω_t, which precisely matches the trap frequency, as can be seen in Fig. 1.

2.1.4 *Single qubit operations*

Quantum algorithms are often considered as a sequence of single-qubit operations plus a specific two-qubit operation. The most common examples of this approach are the conditional phase gate, the controlled-NOT gate, and the $\sqrt{\text{SWAP}}$ gate [38, 39]. Mathematically, we directly find single qubit operations by means of a resonant radiation inducing such a coupling by a rotation $R(\theta, \phi)$ acting on any state vector $\alpha\,|0\rangle + \beta\,|1\rangle$ [39], using the Hamiltonian for Eq. (2.1.14):

$$R\left(\theta, \varphi\right) = \exp\left[i\left(\frac{\theta}{2}\right)\left(e^{i\varphi}\hat{\sigma}_{+} + e^{-i\varphi}\hat{\sigma}_{-}\right)\right] \tag{2.1.19}$$

We know that

$$e^{i\varphi}\hat{\sigma}_{+} + e^{-i\varphi}\hat{\sigma}_{-} = e^{i\varphi}\frac{1}{2}\left(\hat{\sigma}_x + i\hat{\sigma}_y\right) + e^{-i\varphi}\frac{1}{2}\left(\hat{\sigma}_x - i\hat{\sigma}_y\right) = \hat{\sigma}_x\cos\varphi - \hat{\sigma}_y\sin\varphi$$

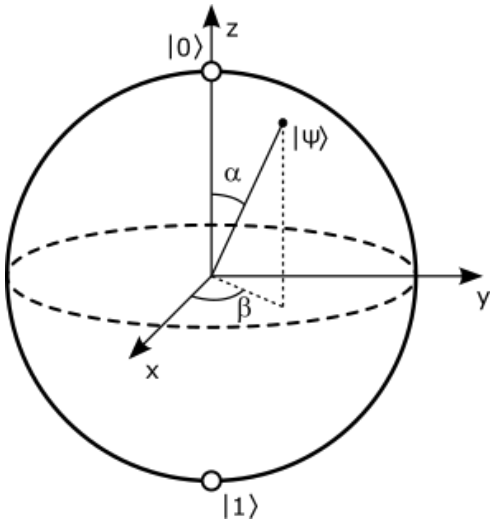

Figure 3: Bloch sphere

and thus

$$\begin{aligned}
R(\theta,\varphi) &= \exp\left[i\left(\frac{\theta}{2}\right)(\hat{\sigma}_x\cos\varphi-\hat{\sigma}_y\sin\varphi)\right] \\
&= \sum_{n=0}^{\infty}\frac{i^n\left[i\left(\frac{\theta}{2}\right)(\hat{\sigma}_x\cos\varphi-\hat{\sigma}_y\sin\varphi)\right]^n}{n!} \\
&= \sum_{n=0}^{\infty}\frac{(-1)^n\left[{}^{i\theta}/_2\,(\hat{\sigma}_x\cos\varphi-\hat{\sigma}_y\sin\varphi)\right]^{2n}}{(2n)!} \\
&\quad +i\sum_{n=0}^{\infty}\frac{(-1)^n\left[{}^{i\theta}/_2\,(\hat{\sigma}_x\cos\varphi-\hat{\sigma}_y\sin\varphi)\right]^{2n+1}}{(2n+1)!} \\
&= I\sum_{n=0}^{\infty}\frac{(-1)^n\left[{}^{i\theta}/_2\right]^{2n}}{(2n)!}+i\,(\hat{\sigma}_x\cos\varphi-\hat{\sigma}_y\sin\varphi)\sum_{n=0}^{\infty}\frac{(-1)^n\left[{}^{i\theta}/_2\right]^{2n+1}}{(2n+1)!} \\
&= I\cos\frac{\theta}{2}+i\,(\hat{\sigma}_x\cos\varphi-\hat{\sigma}_y\sin\varphi)\sin\frac{\theta}{2} \\
&= \begin{pmatrix}\cos\frac{\theta}{2} & ie^{i\varphi}\sin\frac{\theta}{2}\\ ie^{-i\varphi}\sin\frac{\theta}{2} & \cos\frac{\theta}{2}\end{pmatrix}. \qquad (2.1.20)
\end{aligned}$$

It is useful to understand how the single-qubit operations are represented on the Bloch-sphere (see Fig. 3). We identify the north pole with the excited state (logical $|0\rangle$) and the south pole with the ground state (1). In the Bloch sphere picture, the angle β specifies the rotation in the equatorial plane, and thus it doesn't represent any population change but just a phase, and α is the angle in relation to the z axis, which actually is related to the population inversion. Rotations around the z axis, amounting to a phase shift, can be either decomposed into rotations around the x and the y axis or a far detuned laser beam can shift the energies, due to an AC-Stark effect, to achieve the required phase shift.

The relevant control parameters in the experimental realization are the phase of the laser field φ and the pulse area $\theta = \Omega t$, given by the product of the Rabi frequency Ω

times the pulse length t. With these two parameters we can define the two angles of the state in the Bloch sphere. These parameters can be controlled, for example, through an acousto-optical modulator in double-pass configuration [40], manipulating the amplitude and phase of the RF field wich drives the acousto-optical modulator. The θ angle in the Bloch sphere is experimentally accessed via pulse area, which is easy to understand. However, the phase angle φ can be a little confusing. After optical pumping, the experiments start with the ion qubits in an energy eigenstate. Therefore the electric field of the resonant excitation laser generates a dipole (or quadrupole) moment oscillating in phase with the field at the laser frequency. In this way the first laser pulse (whose length is not a multiple of π, in order to get out of the poles of the Bloch sphere) sets the phase reference for all subsequent operations on that ion. Up to this point we can imagine, for example, a $\pi/2$ rotation around the x axis until the equatorial plane. Using the phase of this first laser as reference, now shifting the phase of a second excitation field by π, we are going to apply the same rotation around the x axis as before, but starting from the opposite side of the Bloch sphere. Therefore we will reverse the original evolution.

Single qubit operations are carried out normally with fidelities exceeding 0.99 [41], which are usually limited by intensity fluctuations. Using single-qubit operations we are able to perform single-qubit gates as, for example, Pauli gates and Hadamard gate, which are the most useful in the traditional quantum computation scheme.

2.1.5 *Two-qubit operations - The Cirac-Zoller approach*

One route to achieve a universal set of gates [38] is to complement single-qubit operations with two-qubit gate operations. These operations are one of the most important ingredients of a quantum computer as they provide the possibility to entangle two qubits. In combination with single-qubit operations they allow for implementation of any unitary operation [42].

In ion trap quantum computing, the implementation of suitable two-qubit operations is the most challenging task. The interest in two-qubit operations is documented by a vast number of proposals [43, 44], an important example is the Cirac-Zoller [21].

In this section we discuss the gate proposed by Cirac and Zoller (1995) in which the motional mode acts directly as a mediator transmitting quantum information. The explanation of this quantum gate will be representative for any other two-qubit gate in the traditional scheme of dicrete-variables quantum computation. The idea is to outline this gate in two ways, first developing an abstract explanation, i.e. without worrying about how the operations could be performed physically, and secondly detailing how to achieve these steps in an actual ion trap quantum processor, including the appropriate electromagnetic fields to be applied.

Abstract view

The Cirac-Zoller phase gate can be summarized in three steps, (i) to map the internal state of one ion to the motion of an ion string, (ii) to flip the state of the target ion conditioned on the motion of the ion string, and finally (iii) to map the motion of the ion string back onto the original ion.

1. In the first step we will start considering that we have two ions in their fundamental vibrational state, that is, without phonons. The possible quantum states here are four, and they differ only by the internal states of each of them, thus having the options of: both ions in the ground state, both in the excited state and two possibilities of being one in the ground state and the other in the excited state. Now we apply an excitation in the first ion (so that when it is already in the excited state it would have no effect) accompanied by the creation of a phonon. If it is not possible to have an effect in both degrees of freedom at the same time, electronic and vibrational, then the state is left unchanged

$$\begin{array}{ll} |g_a\rangle\,|g_b\rangle\,|0\rangle & |e_a\rangle\,|g_b\rangle\,|1\rangle \\ |g_a\rangle\,|e_b\rangle\,|0\rangle & \longrightarrow \quad |e_a\rangle\,|e_b\rangle\,|1\rangle \\ |e_a\rangle\,|g_b\rangle\,|0\rangle & |e_a\rangle\,|g_b\rangle\,|0\rangle \\ |e_a\rangle\,|e_b\rangle\,|0\rangle & |e_a\rangle\,|e_b\rangle\,|0\rangle \end{array}$$

2. Then we will exert a transition in the second (target) ion with the following characteristics: if the electronic state is found to be the fundamental one it will take the atom to an auxiliar excited state $|a\rangle$ accompanied by the creation of a phonon and, on the other hand, if the second ion is in the excited state $|e\rangle$, it will go to ground state $|g\rangle$ accompanied by the annihilation of a phonon, all this gaining a phase i. If it is not possible to have an effect in both degrees of freedom at the same time, electronic and vibrational, then the state is left unchanged

$$\begin{array}{ll} |e_a\rangle\,|g_b\rangle\,|1\rangle & i\,|e_a\rangle\,|a_b\rangle\,|2\rangle \\ |e_a\rangle\,|e_b\rangle\,|1\rangle & \longrightarrow \quad i\,|e_a\rangle\,|g_b\rangle\,|0\rangle \\ |e_a\rangle\,|g_b\rangle\,|0\rangle & i\,|e_a\rangle\,|a_b\rangle\,|1\rangle \\ |e_a\rangle\,|e_b\rangle\,|0\rangle & |e_a\rangle\,|e_b\rangle\,|0\rangle \end{array}$$

   then we apply the inverse of this instruction, i.e. if the electronic state is found to be the auxiliar excited state $|a\rangle$ it will take the atom to the fundamental one accompanied by the annihilation of a phonon and, on the other hand, if the second ion is in ground state $|g\rangle$, it will go to the excited state $|e\rangle$ accompanied by the creation of a phonon, all this gaining a phase i. If it is not possible to have an effect in both degrees of freedom at the same time, electronic and vibrational, then the

state is left unchanged

$$\begin{array}{rcl} i\,|e_a\rangle\,|a_b\rangle\,|2\rangle & & -1\,|e_a\rangle\,|g_b\rangle\,|1\rangle \\ i\,|e_a\rangle\,|g_b\rangle\,|0\rangle & \longrightarrow & -1\,|e_a\rangle\,|e_b\rangle\,|1\rangle \\ i\,|e_a\rangle\,|a_b\rangle\,|1\rangle & & -1\,|e_a\rangle\,|g_b\rangle\,|0\rangle \\ |e_a\rangle\,|e_b\rangle\,|0\rangle & & 1\,|e_a\rangle\,|e_b\rangle\,|0\rangle \end{array}$$

3. Finally we apply a transition in the first ion very similar to the one of the previous step, only that the phase here will be of -1, in the following way: when the ion is in the ground state it will be taken to the excited state accompanied by the creation of a phonon, and when it is in the excited state it will end in the fundamental state accompanied by the destruction of a phonon. If it is not possible to have an effect in both degrees of freedom at the same time, electronic and vibrational, then the state is left unchanged

$$\begin{array}{rcl} -1\,|e_a\rangle\,|g_b\rangle\,|1\rangle & & 1\,|g_a\rangle\,|g_b\rangle\,|0\rangle \\ -1\,|e_a\rangle\,|e_b\rangle\,|1\rangle & \longrightarrow & 1\,|g_a\rangle\,|e_b\rangle\,|0\rangle \\ -1\,|e_a\rangle\,|g_b\rangle\,|0\rangle & & 1\,|e_a\rangle\,|g_b\rangle\,|0\rangle \\ 1\,|e_a\rangle\,|e_b\rangle\,|0\rangle & & -1\,|e_a\rangle\,|e_b\rangle\,|0\rangle \end{array}$$

It is easy to observe that the final state will be, in 3 cases, identical to the initial one and, in the remaining case, it will be different only by a minus sign. This conforms what we call a controlled-Z gate, and takes this name because it effectively applies a Z operation (Pauli matrix $\hat{\sigma}_Z$) on the target qubit (ion b) conditioned to the control qubit (ion a) being in the excited state:

$$\begin{pmatrix} 1 & 0 & 0 & 0 \\ 0 & 1 & 0 & 0 \\ 0 & 0 & 1 & 0 \\ 0 & 0 & 0 & -1 \end{pmatrix} \begin{pmatrix} c_{gg} \\ c_{ge} \\ c_{eg} \\ c_{ee} \end{pmatrix} = \begin{pmatrix} c_{gg} \\ c_{ge} \\ c_{eg} \\ -c_{ee} \end{pmatrix}$$

Once one have managed to create this controlled-Z gate, one proceeds using a well-known fact in the quantum computing literature:

$$CNOT = H \times C_Z \times H$$

being here, H a Hadamard gate, and C_Z a controlled-Z gate.

Actual physical view

At the beginning, we consider that we have two ions in their ground vibrational state, that is, without phonons, in the same way that was described in section 2.1.5. The

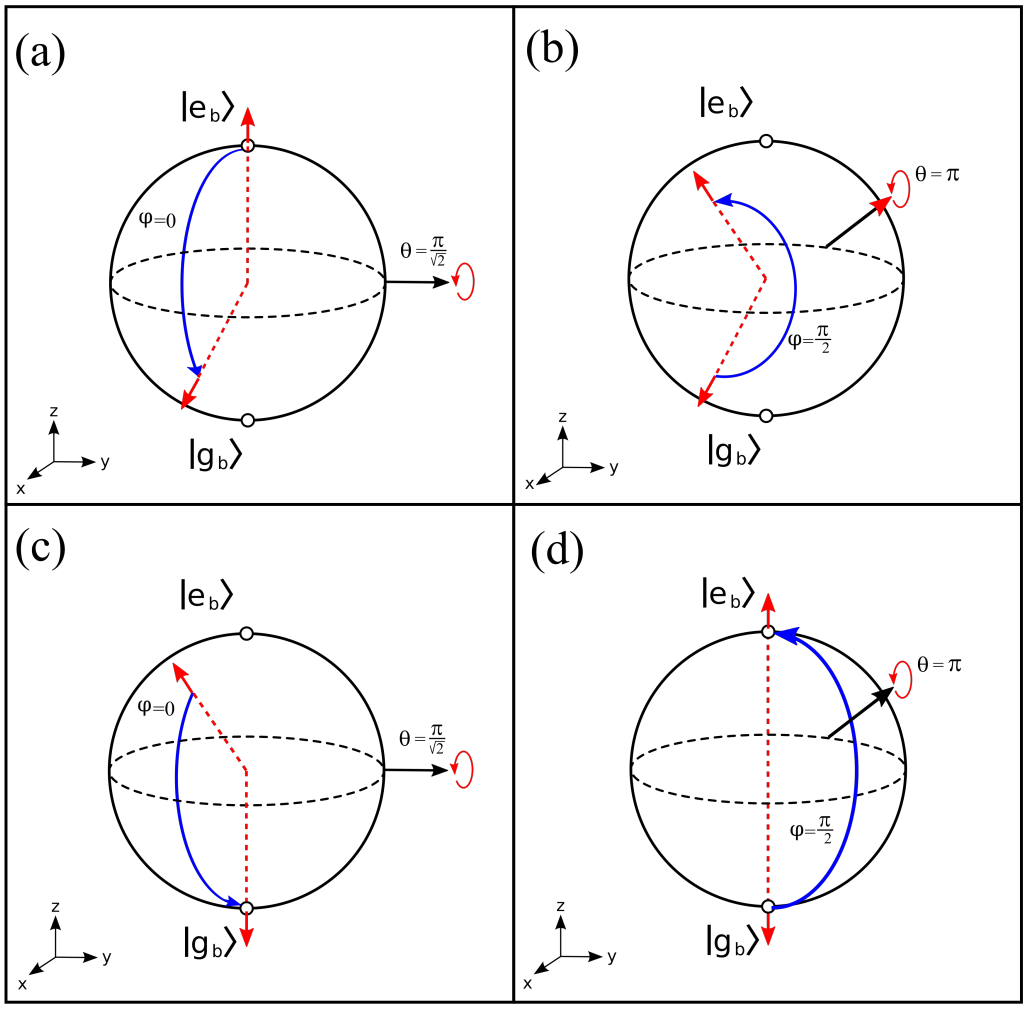

Figure 4: Bloch sphere picture of the target ion in a R_{phase} gate. (a) and (c) show the rotation $R_t^+\left(\frac{\pi}{\sqrt{2}}, 0\right)$, (b) and (d) correspond to $R_t^+\left(\pi, \frac{\pi}{2}\right)$. We can note that same rotations produce different effects depending on the state it is applied in.

coupling between the internal and external degrees of freedom is given by the momentum conservation. The interaction between the ionic qubits can be mediated by motional degrees of freedom, that serve as a quantum bus for distributing quantum information between the ions. Therefore, we will discuss first the manipulation of the motion of single ions and ion strings (see also [34]). The basic level scheme representing a single ion coupled to a single motional mode is depicted in Fig. 1. If the laser field, however, is detuned by the trap frequency towards higher energies, the so-called blue sideband is excited (see Eq. (2.1.15)) and the operation

$$R^{+}(\theta,\phi)=\exp\left[i\frac{\theta}{2}\left(e^{i\varphi}\hat{\sigma}_{+}\hat{a}^{\dagger}+e^{-i\varphi}\hat{\sigma}_{-}\hat{a}\right)\right] \tag{2.1.21}$$

is carried out. Here $\hat{\sigma}_{\pm}$ are the atomic flip operators which act on the electronic quantum state of an ion by inducing transitions from the $|g\rangle$ to the $|e\rangle$ state and vice versa. The operators $\hat{a}$ and $\hat{a}^{\dagger}$ denote the annihilation and creation of a phonon at the trap frequency ω_t, i.e., they act on the motional quantum state. As in Eq. (2.1.20), the parameter θ depends on the strength and duration of the applied pulse, and φ denotes the relative phase between the optical field and the atomic polarization. Importantly, the electronic and motional degrees of freedom change simultaneously. Similarly, for the opposite detuning the red sideband can be excited.

1. In the first step we apply a laser pulse which produces a π rotation on the control ion. In order to clarify let's consider, for example, the state of the second line in the previous subsection, $|\psi_0\rangle = |g_a, e_b, 0\rangle$, then we can generalize it to all possible input states. The first operation is in the notation defined in 2.1.21:

$$R_c^{+}(\pi,0)\,.$$

   The result of this rotation, over the example state, is $|\psi_1\rangle = |e_a, e_b, 1\rangle$. In general, the effect of this first step is to change the traget ion basis from $\{|g_b,0\rangle, |e_b,0\rangle, |g_b,0\rangle, |e_b,0\rangle\}$ to $\{|g_b,1\rangle, |e_b,1\rangle, |g_b,0\rangle, |e_b,0\rangle\}$, in order to apply the next step.

2. Next we realize a composite 2π-rotation by driving a sequence of laser pulses in the blue sideband [45] on the target ion, for example over the state $|\psi_2\rangle$. First we apply the operation (see Fig. 4a)

$$R_t^{+}\left(\frac{\pi}{\sqrt{2}},0\right),$$

   originating a transition to a superposition state

$$|\psi_2\rangle=\frac{1}{2-\sqrt{2}}\left[\frac{1}{\sqrt{2}}|g_b\rangle+\left(1-\frac{1}{\sqrt{2}}\right)|e_b\rangle\right]|e_a,0\rangle\,,$$

   here the vibrational state has lost one phonon. After this we apply a second blue

sideband laser pulse (see Fig. 4b)

$$R_t^+\left(\pi, \frac{\pi}{2}\right).$$

Now our state turns into another superposition state

$$|\psi_3\rangle = \frac{i}{2-\sqrt{2}}\left[\left(1-\frac{1}{\sqrt{2}}\right)|g_b\rangle + \frac{1}{\sqrt{2}}|e_b\rangle\right]|e_a, 1\rangle\,.$$

Here we have gained one phonon and additioned a phase i. Then we use a third laser pulse, equal to the first one (see Fig. 4c). However, the effect now is completely different, because we are in another state

$$R_t^+\left(\frac{\pi}{\sqrt{2}}, 0\right).$$

Our resulting state is $|\psi_4\rangle = i\,|e_a, g_b, 0\rangle$. After that we apply the second pulse again (see Fig. 4d)

$$R_t^+\left(\pi, \frac{\pi}{2}\right),$$

and we have $|\psi_5\rangle = -\,|e_a, e_b, 1\rangle$. If we study the net effect of these 4 pulses, we have a phase gate in the basis $\{|g_b, 1\rangle, |e_b, 1\rangle, |g_b, 0\rangle, |e_b, 0\rangle\}$

$$R_{\text{phase}} = R_t^+(\pi, \frac{\pi}{2})R_t^+\left(\frac{\pi}{\sqrt{2}}, 0\right)R_t^+(\pi, \frac{\pi}{2})R_t^+\left(\frac{\pi}{\sqrt{2}}, 0\right)$$

or in matrix form

$$R_{\text{phase}} = \left(\begin{array}{c|cccc} & |g_b,1\rangle & |e_b,1\rangle & |g_b,0\rangle & |e_b,0\rangle \\ \hline |g_b,1\rangle & -1 & 0 & 0 & 0 \\ |e_b,1\rangle & 0 & -1 & 0 & 0 \\ |g_b,0\rangle & 0 & 0 & -1 & 0 \\ |e_b,0\rangle & 0 & 0 & 0 & 1 \end{array}\right)$$

3. Finally, we need another pulse but now applied on the control ion. Again we use a blue sideband pulse, similar to that of step 1, except for the phase, that in this case is -1:

$$R_c^+(\pi, \pi),$$

finally, in our example, obtaining $|\psi_6\rangle = |g_a, e_b, 1\rangle$, i.e. unchanged compared to the input one in the first step, ψ_0. In general, the gloal of this step, is to get the basis back to $\{|g_b, 0\rangle, |e_b, 0\rangle, |g_b, 0\rangle, |e_b, 0\rangle\}$ and simultaneously introduce a overall -1 factor, and therefore be able to perform an operation in the vibrational ground state basis.

So that, when we put the whole effect of the 3 steps, in general, i.e. extending the example $|\psi_0\rangle \rightarrow |\psi_6\rangle$ over the 4 cases, the output state is not going to be modified with respect to the input but for a constant. Now what we have is the controlled-Z gate explained earlier, in the original basis, as $R_Z = R_c^+(\pi,0)\, R_{\text{phase}} R_c^+(\pi,\pi)$, and summarized in the matrix below

$$R_Z = \left(\begin{array}{c|cccc} & |g_b,0\rangle & |e_b,0\rangle & |g_b,0\rangle & |e_b,0\rangle \\ \hline |g_b,0\rangle & 1 & 0 & 0 & 0 \\ |e_b,0\rangle & 0 & 1 & 0 & 0 \\ |g_b,0\rangle & 0 & 0 & 1 & 0 \\ |e_b,0\rangle & 0 & 0 & 0 & -1 \end{array}\right).$$

As explained earlier, if two Hadamard gates were applied, one before and one after the controlled-Z gate, we would obtain an effective $CNOT$ gate. However, there is a completely equivalent way of performing this approach, as can be found in [46]. The phase gate (R_{phase}) is transformed into a $CNOT_{1100}$ operation, in the computational basis $\{|g_b,1\rangle, |e_b,1\rangle, |g_b,0\rangle, |e_b,0\rangle\}$, if it is sandwiched in between two appropriated $\pi/2$ carrier pulses, $CNOT_{1100} = R_t^C\left(\frac{\pi}{2},\pi\right) R_{\text{phase}} R_t^C\left(\frac{\pi}{2},0\right)$, then we change the basis and apply the overall phase -1, by means the first and third steps mentioned earlier, $CNOT = R_c^+(\pi,\pi) \times CNOT_{1100} \times R_c^+(\pi,0)$. The full pulse sequence is:

$$\begin{aligned} CNOT \;=\; & R_c^+(\pi,\pi) \\ & \times R_t^C\left(\frac{\pi}{2},\pi\right) \\ & \times R_t^+(\pi,\frac{\pi}{2}) R_t^+\left(\frac{\pi}{\sqrt{2}},0\right) \\ & \times R_t^+(\pi,\frac{\pi}{2}) R_t^+\left(\frac{\pi}{\sqrt{2}},0\right) \\ & \times R_t^C\left(\frac{\pi}{2},0\right) \\ & \times R_c^+(\pi,0), \end{aligned}$$

or equivalentely

$$CNOT = \left(\begin{array}{c|cccc} & |g_b,0\rangle & |e_b,0\rangle & |g_b,0\rangle & |e_b,0\rangle \\ \hline |g_b,0\rangle & 1 & 0 & 0 & 0 \\ |e_b,0\rangle & 0 & 1 & 0 & 0 \\ |g_b,0\rangle & 0 & 0 & 0 & 1 \\ |e_b,0\rangle & 0 & 0 & 1 & 0 \end{array}\right),$$

where the subscripts c and t label the control and target ion, and the superscripts $+$ and C label the blue sideband and carrier operations, respectively. Process fidelities of up to 0.92 and entangled states with a fidelity of 0.95 have been demonstrated with this

approach [47].

The observed gate fidelity is well understood in terms of a collection of experimental imperfections. Actually, loss of qubit coherence causes a reduction of the fidelity which can be countered with faster gates. However, this implies larger Rabi frequencies, which in turn spoil the fidelity by uncontrolled AC-Stark shifts [48, 49].

We have shown, up to now, just an example of controlled quantum gate over the internal (discrete) degrees of freedom of trapped ions, the CNOT gate through the Cirac-Zoller approach. However, this example is fundamental to understand how the present view of quantum computation functions. We have shown that vibrational modes are necessary in order to mediate the different energy level qubits, since we can use laser pulses that have effect, simultaneously, in both the internal and external degrees of freedom of the trapped ion. It is interesting to note that everything explained here with blue sideband pulses can be accessed also through red sideband lasers, in a completely equivalent scheme.

2.2 Quantum computation over the vibrational modes

As shown in the previous section, one of the current proposals of quantum computing regards sequences of quantum gates coherently manipulating discrete two-level systems, the qubits [39]. An alternative picture considers physical observables with continuous spectra – continuous variables (CV) – to accomplish the physical encoding and quantum processing [50,51]. In the continuous variables quantum computing (CVQC) paradigm, Gaussian states and Gaussian operations are the fundamental pillars of quantum logic [52, 53], as well as a single non-Gaussian operation needed to attain computation universality [54,55]. In this case an infinite-dimensional Hilbert space holds the basic physical object of quantum computing. This Hilbert space may be considered as continuous in the eigenbasis of some observables, but also can be regarded as a discrete configuration space in the eigenbasis of other observables. In particular, as regarded in this thesis, a motional mode of the ion chain [56–60] can be either studied in terms of superpositions of the quantized energy eigenstates of the harmonic oscillator, the number or Fock states [61] or in the continuous phase space of position and momentum observables, e.g. by the Wigner function. Recent literature on generation, control [62–64] and measurement [65–67] of vibrational modes of trapped ions have been addressed in several manners: by entanglement with optical resonator modes [68], using it as an equivalent model for the study of other systems [69], exotic quantum states generation [70, 71], or simulations of solid state systems [72–74].

In this section, we investigate the implementation of quantum gates in the motional modes [75,76]. We consider the viability and features of turning the CZ paradigm around to use the qubit degree of freedom to mediate the interaction among the vibrational states, as can be seen in Fig. 5. Whereas our proposal can be scaled up to a system of different single ions [77], we focus here on the simplest case of a single trapped ion and its set of

three motional modes as a initial point. We try to establish the potential of this quantum system as well as the expected limitations on the size of the configuration space made possible by this simple change of perspective in the use of the ion trap. We present a CVQC toolbox for manipulation of single modes and the interaction between them, in particular to show which entangling gates would be available. The presented gates are attainable by bichromatic laser fields with tunable frequencies. Number-dependent Rabi flops on the qubit can be performed in order to readout the quantum state [78–80].

2.2.1 *Basic implementation*

Physical system

We will consider, in this proposal, the oscillation modes of the quantum harmonic oscillator as the physical objects to be manipulated [81]. There are three available modes in the simplest case of a single trapped ion oscillator, e.g. x, y, and z axis. In actual experimental conditions, the eigenbasis of the number operator is the best option to quantify the size of the Hilbert space associated with each vibrational mode and available to manipulation. Since the anharmonicities of the actual potential and the unability to manilpulate an unlimited phonon number, the basis for each mode is assumed to be truncated at a maximum phonon number N, and is hence composed of the eigenstates

$$\{0, 1, 2, \ldots, N\}. \tag{2.2.1}$$

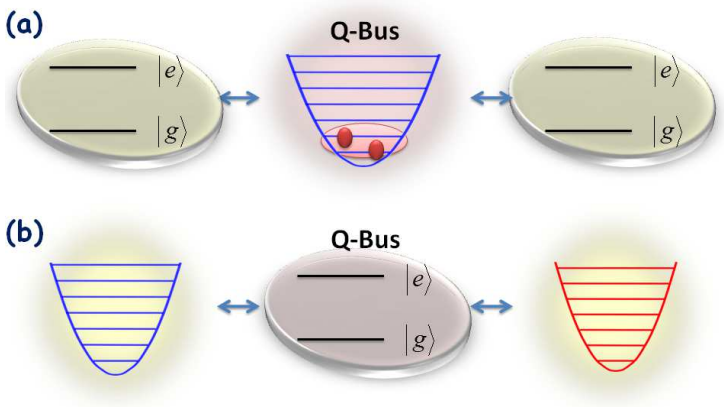

Figure 5: Proposal of CVQC using the ion trap. (a) The CZ paradigm employs one or more motional modes of the quantum harmonic oscillator to mediate the interaction (the 'quantum bus') between pairs of qubits. In the original proposal, one motional mode is essentially employed as a two-level system. Increasing the size of the Hilbert space requires adding more ions to the physical system, reaching an exponential increase. (b) Our proposal utilizes the qubit as the quantum bus that allows vibrational modes to interact. Three harmonic oscillator form the Hilbert space available for manipulation. The size of the Hilbert space available is outright larger than in the CZ paradigm, although it increases only polynomially with the phonon cap number.

The quantum state represented in terms of phonon number eigenstates relates to a 'particle-like' picture of the system. The quantum state of the harmonic oscillator also

admits a CV representation in the position and momentum phase space, a 'wave-like' description employing the Wigner function. This function is a quasiprobability distribution which is devoted to the study of quantum corrections to classical statistical mechanics. The goal is to link the wavefunction that appears in Schrödinger's equation to a probability distribution in phase space. Quantum gates are transformations of the Wigner function in phase space. In the ion trap processor, bichromatic laser light can be used to perform quantum gates by coupling motional modes to the internal degrees of freedom [27, 28, 82, 83]. The qubit is by construction a highly non-linear physical system – one that saturates with a single quantum –, a property here employed to generate non-Gaussian operations on the vibrational modes. We impose that $\hat{\rho} = \hat{\rho}_q \hat{\rho}_m$, where qubit ($\hat{\rho}_q$) and motional modes ($\hat{\rho}_m$) states are separable before and after the application of quantum gates, since in our proposed architecture the qubit is only an auxiliary source of non-linearity and coupling among motional modes.

The proposed CVQC toolbox of operations can be divided in Gaussian and non-Gaussian operations. The class of Gaussian operations is defined as which maintains as Gaussian an initially Gaussian Wigner function. There are single- and two-mode Gaussian operations. Single-mode displacements and squeezers, respectively, displace the origin of phase space or change the scale of the position and momentum axis. Both of them have already been experimentally demonstrated in the ion trap processor [84, 85]. Two-mode operations comprise the beam splitter and the two-mode squeezer. The beam splitter is a passive transformation that linearly combines two field modes. The two-mode squeezer, an active transformation, can be understood as two single-mode squeezers simultaneously acting on orthogonal combinations of two modes. It is also possible to comprise two-mode conditional gates as generalizations of such operations. Examples of non-Gaussian operations are obtained by the blue and red sideband interactions, producing single-mode phonon creation or annihilation, as well as it is possible, through the cross Hamiltonian counterpart, to achieve simultaneous creation or annihilation of two photons, one in each mode.

Hamiltonian of the ion trap

The CV toolbox of quantum operations is developed concerning the simplest implementation of an ion trap processor: a single ion comprising the qubit and three independent modes of vibration. We consider in this section the basic coherent manipulation of a single trapped ion by an external source of coherent light [61, 86].

We recall the Hamiltonian regarding one qubit and two motional modes coupled to it by a monochromatic external laser. The generalization of the interaction to three oscillator modes and bichromatic lasers capable of producing the desired quantum gates follows next.

In the mentioned case, the ion trap Hamiltonian reads as

$$\hat{H} = \hat{H}_0 + \hat{H}_I, \tag{2.2.2}$$

where $\hat{H}_I$ is the interaction Hamiltonian discussed below and $\hat{H}_0$ provides the free dynamics of qubit and motional modes,

$$\hat{H}_0 = \tfrac{1}{2}\hbar\omega_0\hat{\sigma}_z + \hbar\omega_a\hat{a}^\dagger\hat{a} + \hbar\omega_b\hat{b}^\dagger\hat{b}. \tag{2.2.3}$$

The frequency of the qubit transition is ω_0 and its two-dimensional Hilbert space is described in terms of the excited e and ground g internal states of the ion, with which we write $\hat{\sigma}_z = ee - gg$. The two independent vibrational modes under consideration are described in terms of the annihilation operators $\hat{a}$ and $\hat{b}$ and the respective creation operators satisfying the commutation relations $[\hat{a}, \hat{a}^\dagger] = [\hat{b}, \hat{b}^\dagger] = 1$. Their oscillation frequencies are ω_s, where $s \in \{a, b\}$ denotes the mode.

A dipolar coupling between the ion and an external coherent light source is modeled by the simplest interaction Hamiltonian $\hat{H}_I = -\vec{d}\cdot\vec{E}$. The atomic dipole operator is $\vec{d} = \vec{\mu}(\hat{\sigma}_+ + \hat{\sigma}_-)$, with dipole moment $\vec{\mu}$ and operators $\hat{\sigma}_+ = eg$ and $\hat{\sigma}_- = ge$. The light source drives the ion by means of the electric field $\vec{E} = \vec{E}_0 \exp(i\vec{k}\cdot\vec{r} - i\omega_L t)$ with wavevector $\vec{k}$ and frequency ω_L. The interaction Hamiltonian can be made to account for the free evolution associated with $\hat{H}_0$ (interaction picture), yielding

$$\begin{aligned}\tilde{H}_I = \tfrac{1}{2}\hbar\Omega\hat{\sigma}_+^{-i\delta t}\exp[&i\eta_a(\hat{a}e^{-i\omega_a t} + \hat{a}^\dagger e^{i\omega_a t}) \\ &+ i\eta_b(\hat{b}e^{-i\omega_b t} + \hat{b}^\dagger e^{i\omega_b t})] + \text{h.c.},\end{aligned} \tag{2.2.4}$$

where $\Omega = |\vec{\mu}\cdot\vec{d}|/\hbar$ is the Rabi frequency, $\delta = \omega_L - \omega_0$ is the radiation-atom detuning, and $\eta_s = kx_s\cos\theta$ are the Lamb-Dicke parameters, defined in terms of the typical scale of the ground state oscillator wavefunction $x_s = \sqrt{\hbar/(2m\omega_s)}$ and the direction of propagation θ of the laser with respect to the direction of vibration of mode s. Typical experimental conditions in optical qubits imply $\eta_s \ll 1$, values for which the Lamb-Dicke regime can be evoked to expand the interaction Hamiltonian in powers of η_s.

In the next section we consider CV quantum gates obtained via expansion of the interaction Hamiltonian up to second order in η_s [87, 88], as

$$\begin{aligned}\tilde{H}_I =& \hat{H}^{(0)} + \eta_a\hat{H}_a^{(1)} + \eta_b\hat{H}_b^{(1)} \\ &- \eta_a^2\hat{H}_a^{(2)} - \eta_b^2\hat{H}_b^{(2)} - 2\eta_a\eta_b\hat{H}_{ab}^{(2)} + \mathcal{O}(\eta_s^3).\end{aligned} \tag{2.2.5}$$

Each term is studied in the Fock basis of the motional states. The single-quantum saturation associated with the qubit degree of freedom plays the fundamental role of allowing the coherent manipulation of single quanta in the motional modes.

The first Hamiltonian, i.e. the zeroth-order term, considers the carrier transition, resonant for $\delta = 0$:

$$\hat{H}^{(0)} = \tfrac{1}{2}\hbar\Omega' \left({}^{-i\delta t}\hat{\sigma}_+ + {}^{i\delta t}\,\hat{\sigma}_- \right). \tag{2.2.6}$$

We can notice a modified Rabi frequency Ω', which depends on the motional coupling as $\Omega' = (1 - \eta_a^2 - \eta_b^2)\Omega$. This Hamiltonian induces qubit transitions without affecting the motional state of the ion. It may be used to prepare the qubit quantum state in order to apply a suitable control over the motional modes.

The next two first-order terms involve the blue- and red-sideband transitions of each vibrational mode, through the Hamiltonians

$$\begin{aligned} \hat{H}_s^{(1)} = {} & \tfrac{1}{2}\hbar\Omega \left({}^{-i(\delta+\omega_s)t}\hat{\sigma}_+\hat{s} + {}^{i(\delta+\omega_s)t}\,\hat{\sigma}_-\hat{s}^\dagger \right) \\ & + \tfrac{1}{2}\hbar\Omega \left({}^{-i(\delta-\omega_s)t}\hat{\sigma}_+\hat{s}^\dagger + {}^{i(\delta-\omega_s)t}\,\hat{\sigma}_-\hat{s} \right). \end{aligned} \tag{2.2.7}$$

The terms resonant for $\delta = -\omega_s$, promote the excitation of the qubit while annihilating a phonon in the motional mode, and conversely; the remaining two terms, resonant for $\delta = \omega_s$, excite the qubit while creating one additional phonon in mode $\hat{s}$, and vice-versa. The CZ paradigm utilizes this Hamiltonian to map the qubit state into one motional mode or to realize conditional logic between them, employing the vibrational mode as an effective two-level ancilla system.

We focus mainly in the second-order terms of $\hat{H}_I$. They entail the creation or annihilation of two phonons at a time together with the excitation or deexcitation of the qubit. The single-mode Hamiltonians are

$$\begin{aligned} \hat{H}_s^{(2)} = {} & \tfrac{1}{2}\hbar\Omega \left({}^{-i\delta t}\hat{\sigma}_+ + {}^{i\delta t}\,\hat{\sigma}_- \right) \hat{s}^\dagger\hat{s} \\ & + \tfrac{1}{2}\hbar\Omega \left({}^{-i(\delta+2\omega_s)t}\hat{\sigma}_+\hat{s}^2 + {}^{i(\delta+2\omega_s)t}\,\hat{\sigma}_-\hat{s}^{\dagger 2} \right) \\ & + \tfrac{1}{2}\hbar\Omega \left({}^{-i(\delta-2\omega_s)t}\hat{\sigma}_+\hat{s}^{\dagger 2} + {}^{i(\delta-2\omega_s)t}\,\hat{\sigma}_-\hat{s}^2 \right). \end{aligned} \tag{2.2.8}$$

The second-order term $\hat{H}_{ab}^{(2)}$, so-called cross Hamiltonian, creates or annihilates pairs of phonons, one in each mode, via the interaction

$$\begin{aligned} \hat{H}_{ab}^{(2)} = {} & \frac{\hbar\Omega}{2} \left({}^{-i(\delta+\omega_a-\omega_b)t}\hat{\sigma}_+\hat{a}\hat{b}^\dagger + {}^{i(\delta+\omega_a-\omega_b)t}\,\hat{\sigma}_-\hat{a}^\dagger\hat{b} \right) \\ & + \frac{\hbar\Omega}{2} \left({}^{-i(\delta-\omega_a+\omega_b)t}\hat{\sigma}_+\hat{a}^\dagger\hat{b} + {}^{i(\delta-\omega_a+\omega_b)t}\,\hat{\sigma}_-\hat{a}\hat{b}^\dagger \right) \\ & + \frac{\hbar\Omega}{2} \left({}^{-i(\delta+\omega_a+\omega_b)t}\hat{\sigma}_+\hat{a}\hat{b} + {}^{i(\delta+\omega_a+\omega_b)t}\,\hat{\sigma}_-\hat{a}^\dagger\hat{b}^\dagger \right) \\ & + \frac{\hbar\Omega}{2} \left({}^{-i(\delta-\omega_a-\omega_b)t}\hat{\sigma}_+\hat{a}^\dagger\hat{b}^\dagger + {}^{i(\delta-\omega_a-\omega_b)t}\,\hat{\sigma}_-\hat{a}\hat{b} \right). \end{aligned} \tag{2.2.9}$$

Following the same reasoning, the n^{th}-order term of $\hat{H}_I$, if considered, would coherently distribute n phonons between the two modes, although with ever decreasing coupling strength of order η_s^n, which would imply longer operation times.

2.2.2 *Bichromatic CV quantum gates*

The qubit gives a convenient way to add or subtract individual phonons in motional modes, due to its property of saturating with the absorption of a single quantum. At the same time, it also prevents the motional state from attaining a fast increase in the number of excitations.

Continuous variables quantum gates must be allowed to visit ever higher excitation numbers without saturating, a feature that may require the qubit state to factor out of the interaction. Hence to allow interesting combinations of terms of $\hat{H}_s^{(1)}$, $\hat{H}_s^{(2)}$, or $\hat{H}_{ab}^{(2)}$ to be simultaneously resonant, we consider bichromatic light sources to drive the quantum dynamics [27, 28, 82, 83].

A more intuitive representation of CV operations in this case makes use of the phase space of position and momentum observables, describing quantum gates in terms of the transformations they produce in the Wigner function of the quantum system. We employ this approach below to describe the quantum operations of the toolbox.

Single-mode Gaussian operations

We will now describe the set of single-mode Gaussian operations, which comprises displacements and squeezers.

Displacements consist of a translation of the phase space, or equivalently a rigid motion of the Wigner function. If the arguments of the single-mode Wigner function are x_s and p_s, a displacement with parameter $\alpha = x_\alpha + ip_\alpha$ produces the phase space transformations $x_s \to x_s - x_\alpha$ and $p_s \to p_s - p_\alpha$.

For their part, squeezers scale up the phase space, compressing and stretching different directions, while respecting the conservation of areas . A squeezer with parameter $\xi = r\exp(2i\theta)$ affects the orthogonal axis $x_\theta = \cos\theta x_s + \sin\theta p_s$ and $p_\theta = -\sin\theta x_s + \cos\theta p_s$ in phase space according to the transformations $x_\theta \to e^{-r}x_\theta$ and $p_\theta \to e^r p_\theta$. In the description in terms of phonons, the most prominent characteristic of a squeezed state is the primacy of even numbers of quanta.

Despite the Fourier transform operation being formally implicit in the squeezing operation, we are going to consider them as separate quantum gates. In phase space, the Fourier transform gate produces a rotation. It transforms position and momentum according to the $x_s \to x_\theta$ and $p_s \to p_\theta$ defined above. In the phonon picture, the Fourier gate introduces a number-dependent phase shift in the form $n_s \to e^{in\theta}n_s$, where n_s is the phonon number in mode $\hat{s}$, generating a dynamics akin to the free evolution of the oscillator.

Let's begin introducing the single-mode displacement Hamiltonian. Since we are interested specifically on the ion trap processor, a single-mode displacement of mode $\hat{s}$ is performed by the Hamiltonian $\hat{H}_s^{(1)}$, given the conditions below. Two coherent radiation

sources with the same intensity and opposite detunings $\delta_1 = -\delta_2 = \delta = \omega_s$, according to Eq. (2.2.7), generate the Hamiltonian

$$\hat{H}_s^{(1)} = i\hbar\hat{\sigma}_{\phi-\pi/2}\left(\tilde{\alpha}\hat{s}^\dagger - \tilde{\alpha}^*\hat{s}\right), \tag{2.2.10}$$

where the relative phase between the two frequency components of light is 2ϕ and $\hat{\sigma}_\phi = \hat{\sigma}_x\cos\phi + \hat{\sigma}_y\sin\phi$. This phase controls the displacement parameter per unit time, given by $\tilde{\alpha} = \Omega^{i\left(\phi-\frac{\pi}{2}\right)}$. The realization of a single-mode displacement operation requires the qubit quantum state to be initialized in an eigenstate of the operator $\hat{\sigma}_{\phi-\pi/2}$. This can be done by a resonant pulse as in Eq. (2.2.6). Let us adopt the convention that the qubit eigenstate $+_{\phi-\pi/2}$ with positive eigenvalue is chosen. Then the displacement $\hat{D}(\alpha) := \exp\left(\alpha\hat{s}^\dagger - \alpha^*\hat{s}\right)$ of mode $\hat{s}$ by the amplitude $\alpha = \eta_s^2\tilde{\alpha}t$ is produced by the evolution operator $\hat{D}_s = \exp\left(-i\eta_s^2\hat{H}_s^{(1)}t/\hbar\right)$.

Hamiltonian $\hat{H}_s^{(2)}$ gives rise to the single-mode squeezing operation. The bichromatic field with detunings $\delta_1 = -\delta_2 = \delta = 2\omega_s$ will produce according to Eq. (2.2.8) the nonlinear dynamics

$$\hat{H}_s^{(2)} = i\hbar\hat{\sigma}_\phi\left(\tilde{\xi}^*\hat{s}^2 - \tilde{\xi}\hat{s}^{\dagger 2}\right), \tag{2.2.11}$$

which is expressed in terms of the squeezing parameter per unit time $\tilde{\xi} = \Omega^{i(\phi-\pi/2)}$. Provided the qubit is prepared in the eigenstate $+_\phi$, acting with this Hamiltonian on the motional state for a time t will implement the single-mode squeezing operator $\hat{S}(\xi) = \exp\left(\xi^*\hat{s}^2 - \xi\hat{s}^{\dagger 2}\right)$, with squeezing parameter $\xi = \eta_s^2\tilde{\xi}t$. The corresponding evolution operator is $\hat{S}_s = \exp\left(-i\eta_s^2\hat{H}_s^{(2)}t/\hbar\right)$. Although not systematically investigated, quantum noise reduction has been observed in the motional state of trapped ions [84, 85], revealing the potential of the ion trap to produce large amounts of squeezing for quantum computing.

The Fourier transform operation is realized with $\delta = 0$, i.e. by a monochromatic laser tuned to the qubit transition. The Hamiltonian reads as

$$\hat{H}_s'^{(2)} = \tfrac{1}{2}\hbar\Omega\hat{\sigma}_\phi\hat{s}^\dagger\hat{s}, \tag{2.2.12}$$

and provides the evolution $\hat{F} = e^{i\theta\hat{s}^\dagger\hat{s}}$, where the rotation phase is $\theta = \eta_s^2\Omega t/2$, provided the qubit remains in the state $+_\phi$.

Two-mode Gaussian operations

Two-mode Gaussian operations act on two vibrational modes in order to produce transformations in linear combinations of modal operators. They can be either passive, promoting the exchange of quanta between modes, or active, in which case quanta are concomitantly added or removed from both modes in a correlated way.

Beam splitter (named after its optical counterpart) is a passive quantum gate that coherently combines the modal operators by amounts that vary with the interaction time. On the other hand, the two-mode squeezer is an active operation which produces correlated pairs of quanta, in the phonon picture, or EPR-like entangled states in the phase space picture [89].

The mentioned two-mode operations are achieved in the ion trap processor by means of the cross Hamiltonian $H_{ab}^{(2)}$. A bichromatic field may modify Eq. (2.2.9) to produce two types of dynamics. On the first one, we choose radiation frequencies such that $\delta_1 = -\delta_2 = \delta = \omega_a - \omega_b$ (we assume $\omega_a > \omega_b$ for definiteness). The resulting Hamiltonian reads

$$\hat{H}_{ab}^{(2)} = \hbar\Omega\,\hat{\sigma}_\phi \left({}^{-i\phi}\hat{a}\hat{b}^\dagger + {}^{i\phi}\,\hat{a}^\dagger\hat{b} \right). \tag{2.2.13}$$

Specifically, the beam splitter transformation is performed by the evolution operator $\hat{I}_{ab} = \exp\left(-i\eta_a\eta_b\hat{H}_{ab}^{(2)}t/\hbar\right)$. It promotes the interference of modal operators in the form $\hat{a} \to \hat{a}\cos(\phi t) + \hat{b}\sin(\phi t)$ and $\hat{b} \to -\hat{a}\sin(\phi t) + \hat{b}\cos(\phi t)$, where $\phi = 2\eta_a\eta_b\Omega$. For instance, modes interfere maximally at half this time, for $t = \pi/(2\phi)$; for double that amount of time, the quantum state of one mode is mapped into the other, and vice-versa, coherently exchanging their local quantum states. In case the two-mode quantum state is initially separable, the beam splitter dynamics will entangle the modes unless the initial state is a coherent state.

The second kind of two-mode dynamics involves detunings $\delta_1 = -\delta_2 = \delta = \omega_a + \omega_b$. The resonant terms of Eq. (2.2.9) produce the interaction Hamiltonian

$$\hat{H}_{ab}^{\prime(2)} = \hbar\Omega\,\hat{\sigma}_\phi \left({}^{-i\phi}\hat{a}\hat{b} + {}^{i\phi}\,\hat{a}^\dagger\hat{b}^\dagger \right). \tag{2.2.14}$$

The two-mode squeezer operation, $\hat{E}_{ab} = \exp\left(i\hat{H}_{ab}^{\prime(2)}t/\hbar\right)$, produces EPR-type entangled states between the motional modes when acting over the oscillator ground state. As in previous cases, the relative phase between the laser frequency components controls the operation phase as long as the qubit degree of freedom is prepared in the eigenstate $+_\phi$.

Non-Gaussian single- and two-mode operations

Starting from a Gaussian quantum state, Gaussian operations are restricted to produce only Gaussian states. In order to get more general quantum states and achieve computational universality, at least one non-Gaussian operation is needed [54, 55]. In fact, the ion trap quantum processor provides a wide variety of non-Gaussian operations, made available by the strong non-linearity of the qubit degree of freedom, which saturates with a sole quantum. The number of phonons in the CV degrees of freedom can thus be increased by discrete amounts by coupling it with the qubit, thus producing non-Gaussian quantum states.

The most suitable operation of single-mode phonon creation or annihilation arises from the red- and blue-sideband interactions produced by $\hat{H}_s^{(1)}$ [Eq. (2.2.7)]. They can be realized with a monochromatic laser beam with frequency $\delta = \omega_s$ (blue sideband) or $\delta = -\omega_s$ (red sideband), respectively, yielding

$$\hat{H}_{s,\text{blue}} = \tfrac{1}{2}\hbar\Omega\left(\hat{\sigma}_+\hat{s}^\dagger + \hat{\sigma}_-\hat{s}\right), \tag{2.2.15}$$

$$\hat{H}_{s,\text{red}} = \tfrac{1}{2}\hbar\Omega\left(\hat{\sigma}_+\hat{s} + \hat{\sigma}_-\hat{s}^\dagger\right). \tag{2.2.16}$$

We denote the blue sideband evolution operator as $\hat{B}_s = \exp\left(-i\eta_s\hat{H}_{s,\text{blue}}t/\hbar\right)$ and the red sideband as $\hat{R}_s = \exp\left(i\eta_s\hat{H}_{s,\text{red}}t/\hbar\right)$. Both interactions show linear coupling strength on η_s, making them stronger in comparison with the Gaussian operations considered previously. This property favors the creation or annihilation of any number of phonons in a stepwise process, by applying blue or red sidebands intercalated by π-pulses in the carrier transition ($\delta = 0$). In this manner, the Fock state n can be generated.

In the case of two-mode non-Gaussian operations, the cross Hamiltonian $\hat{H}_{ab}^{(2)}$ allows the simultaneous creation or annihilation of two phonons, one in each mode, by also employing a laser of single frequency. For example, a laser with detuning $\delta = \pm(\omega_a - \omega_b)$ will remove one phonon from one mode and create one phonon in the other, promoting the coherent exchange of a single excitation between modes.

Processes of creation or annihilation of phonons must be realized over suitable initial states, such as the ground state of the oscillator, in order to avoid entanglement between qubit and vibrational modes. In this manner, non-Gaussian features can be used as resources introduced at certain steps of the computation obeying such constraint (e.g. at its beginning).

If operations in other modes were needed, a third vibrational mode (ancilla) can be employed. For instance, in the case of Gaussian operations, a displacement operation can be realized by writing a coherent state with large amplitude on the ancilla mode and applying the beam splitter operation for a short duration to coherently combine its quantum state with that of mode $\hat{a}$ or $\hat{b}$. Non-Gaussian features could also be written in the third mode and then introduced in other modes by the two-mode Gaussian operators mentioned previously. Operations such as sum or subtraction of phonons could be realized in a similar manner.

Two-mode conditional operations

As seen in the previous section, controlled gates are the core of quantum computation. Two-mode controlled operations are intended to change the quantum state of one mode conditioned on the state of another, usually generating entanglement [51]. One example

of such operation is the controlled displacement, represented by the operator

$$\hat{C}_{\hat{x}_a} = \exp(-i\hat{x}_a \otimes \hat{p}_b) \ , \tag{2.2.17}$$

where the order of the systems is *control* $\otimes$ *target*. For instance, if both modes start as independent coherent states, this gate displaces the average momentum of the target mode by the average position of the control mode. Other types of controlled gates can be devised by taking Eq. (2.2.17) as model.

In our proposal, controlled gates can be deployed by two bichromatic lasers, i.e. by tetrachromatic light. In fact, by the form of Eq. (2.2.17), conditioned dynamics can be seen to involve a combination of beam splitter and squeezing operations. A tetrachromatic laser with frequency components $\delta_1 = -\delta_2 := \omega_a - \omega_b$ and $\delta_3 = -\delta_4 := \omega_a + \omega_b$ with the same intensity gives rise to the dynamics

$$\hat{H}_{ab}^{''(2)} = \hbar\Omega\, \hat{\sigma}_\phi \hat{x}_a \hat{x}_{\phi,b}, \tag{2.2.18}$$

where $\hat{x}_{\phi,b} = e^{-i\phi}\hat{b} + e^{i\phi}\hat{b}^\dagger = \hat{x}_b \cos\phi + \hat{p}_b \sin\phi$ is a rotated coordinate in the phase space of mode $\hat{b}$. The evolution operator is $\hat{C}_{ab} = \exp\left(-i\eta_a\eta_b \hat{H}_{ab}^{''(2)} t/\hbar\right)$.

Schwinger map

Considering two harmonic oscillators, we can derive the algebra of angular momentum of the associated operators according to the map $\hat{J}_+ = \hat{a}^\dagger\hat{b}$ and $\hat{J}_- = \hat{a}\hat{b}^\dagger$, where $\hat{J}_\pm = \hat{J}_x \pm i\hat{J}_y$ are the raising and lowering operators defined in terms of the x- and y-components of the angular momentum vector. The corresponding z-component is represented by the operator $\hat{J}_z = (\hat{a}^\dagger\hat{a} - \hat{b}^\dagger\hat{b})/2$. Each eigenvalue of the angular momentum magnitude $\hat{J}^2$ corresponds to a fixed total number $N = n_a + n_b$ of phonons available in the two modes. Eigenstates of $\hat{J}^2$ can be represented by an angular momentum vector over a sphere. The poles of the sphere are the eigenstates N and $-N$ of $\hat{J}_z$. They correspond to the harmonic oscillator states $N_a 0_b$ and $0_a N_b$, respectively. The other eigenstates of $\hat{J}_z$ exist as superpositions of Fock states $n_a N - n_b$, where n is the difference of quanta between modes $\hat{a}$ and $\hat{b}$ (equal to half the eigenvalue of $\hat{J}_z$).

Sometimes, the two-mode quantum operations described above, can be understood as manipulations of such angular momentum vector, even though in most cases the two-mode motional quantum state will not be in a superposition of Fock states satisfying the property $n_a + n_b = N$. The Schwinger map is particularly suitable to treat the beam splitter operation, since it conserves the total number of excitations in the two modes. In the Schwinger map, the beam splitter Hamiltonian of Eq. (2.2.13) reads as

$$\hat{H}_{ab}^{(2)} = \hbar\Omega\, \hat{\sigma}_\phi \hat{J}_\phi, \tag{2.2.19}$$

where $\hat{J}_\phi = \cos\phi \hat{J}_x + \sin\phi \hat{J}_y$. Hence the beam splitter operation can be interpreted as a rotation of the angular momentum vector existing in the sphere associated with an eigenstate of $\hat{J}^2 = \hat{J}_x^2 + \hat{J}_y^2 + \hat{J}_z^2$. For quantum states inhabiting more than one sphere, the beam splitter realizes a coherent superposition of rotations, one in each sphere.

2.2.3 *Ion trap CVQC toolbox*

Architecture

The CVQC implementation by means of the motional modes of trapped ions requires the ability to select specific quantum dynamics by tuning the properties of the manipulation laser. As presented above, quantum gates can be implemented with monochromatic radiation or using a combination of frequency components commensurate with the frequencies of vibration. They are selected by radiation frequency (detuning) and direction of propagation (Lamb-Dicke parameter).

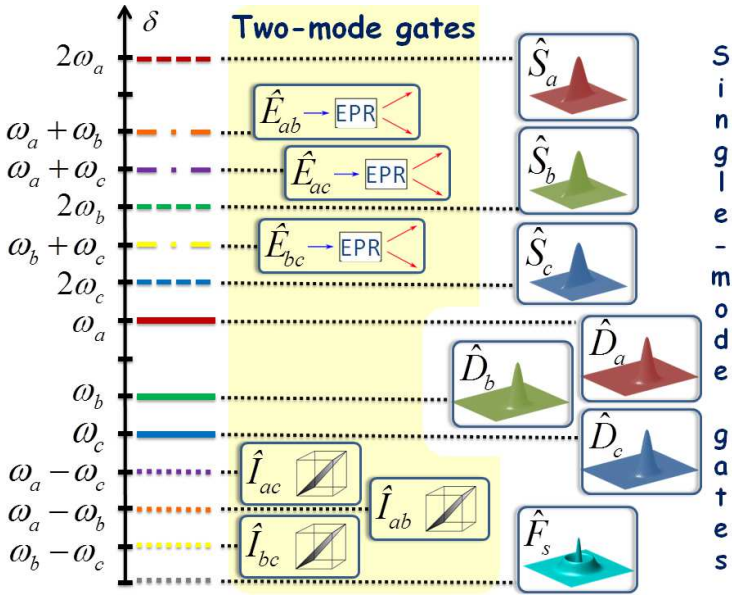

Figure 6: Toolbox of Gaussian operations available for the manipulation of the vibrational state of a single trapped ion. The desired quantum gate is selected by radiation frequency. With the exception of the Fourier transform operation $\hat{F}_s$ which needs monochromatic light with $\delta = 0$, all quantum gates require bichromatic radiation with $\delta_1 = -\delta_2 = \delta$. Possible values of detuning correspond to any of the: vibrational frequencies ω_s (continuous lines), double those frequencies (dashed lines), subtraction (dotted lines) or sum (dash-dot lines) of pairs of frequencies. The corresponding Gaussian operations are displacements $\hat{D}_s$, squeezers $\hat{S}_s$, beam splitters $\hat{I}_{ss'}$, and two-mode squeezers $\hat{E}_{ss'}$, respectively, where $s, s' \in \{a, b, c\}$. In choosing the ratio of vibrational frequencies, we have adopted the proportion $\omega_a : \omega_b : \omega_c = 7 : 5 : 4$.

The set of all quantum gates described in Sec. 2.2.2 conform the basic toolbox to carry out the coherent manipulation of the vibrational modes. Figure 6 shows the Gaussian operations together with the bichromatic laser detunings required for their realization in the case that all three vibrational modes of a single trapped ion are employed (the label s now reads $s \in \{a, b, c\}$).

The five single-mode quantum gates: the displacement $\hat{D}_s$, squeezer $\hat{S}_s$, Fourier transform $\hat{F}_s$, blue- $\hat{B}_s$, and red-sideband $\hat{R}_s$ operations, were previously developed in detail, however let's summarize their necessary laser frequency components and evolution operators:

$$\begin{aligned}
\delta_1 = -\delta_2 = \omega_s: &\quad \hat{D}_s = e^{-\frac{i}{\hbar}\eta_s^2 \hat{H}_s^{(1)} t}, \\
\delta_1 = -\delta_2 = 2\omega_s: &\quad \hat{S}_s = e^{-\frac{i}{\hbar}\eta_s^2 \hat{H}_s^{(2)} t}, \\
\delta = 0: &\quad \hat{F}_s = e^{-\frac{i}{\hbar}\eta_s^2 \hat{H}_s'^{(2)} t}, \\
\delta = \omega_s &\quad \hat{B}_s = e^{-\frac{i}{\hbar}\eta_s \hat{H}_{s,\mathrm{blue}} t}, \\
\delta = -\omega_s: &\quad \hat{R}_s = e^{-\frac{i}{\hbar}\eta_s \hat{H}_{s,\mathrm{red}} t}.
\end{aligned} \tag{2.2.20}$$

Two-mode operations must be applied to pairs of modes. To account for the three combinations of mode pairs, we introduce a second index $s' \in \{a, b, c\}$. The two-mode gates are the beam splitter $\hat{I}_{ss'}$, the two-mode squeezer $\hat{E}_{ss'}$, and the general conditional operation $\hat{C}_{ss'}$. They require the radiation frequencies:

$$\begin{aligned}
\delta_1 = -\delta_2 = \omega_s - \omega_{s'}: &\quad \hat{I}_{ss'} = e^{-\frac{i}{\hbar}\eta_s \eta_{s'} \hat{H}_{ab}^{(2)} t}, \\
\delta_1 = -\delta_2 = \omega_s + \omega_{s'}: &\quad \hat{E}_{ss'} = e^{-\frac{i}{\hbar}\eta_s \eta_{s'} \hat{H}_{ab}^{'(2)} t}, \\
\begin{cases} \delta_1 = -\delta_2 = \omega_s - \omega_{s'} \\ \delta_3 = -\delta_4 = \omega_s + \omega_{s'} \end{cases} &: \quad \hat{C}_{ss'} = e^{-\frac{i}{\hbar}\eta_s \eta_{s'} \hat{H}_{ab}^{''(2)} t}.
\end{aligned} \tag{2.2.21}$$

Three types of gates utilize monochromatic radiation (Fourier transform $\hat{F}_s$, blue-sideband $\hat{R}_s$ and red-sideband $\hat{R}_s$), four require bichromatic lasers (displacement $\hat{D}_s$, squeezer $\hat{S}_s$, beam splitter $\hat{I}_{ss'}$, and two-mode squeezer $\hat{E}_{ss'}$), and one employs tetrachromatic light (the conditional operation $\hat{C}_{ss'}$).

Different operations are selected by laser detuning δ and propagation direction (through η_s), so as to keep off-resonant terms of the complete Hamiltonian sufficiently detuned in order to avoid exciting population in undesirable quantum states. Hence for a given pair of modes the proposed CVQC architecture requires the frequencies ω_s, $\omega_{s'}$, $2\omega_s$, $2\omega_{s'}$, $\omega_s - \omega_{s'}$, and $\omega_s + \omega_{s'}$ to be incommensurate and sufficiently separated. For a processor based on the three motional modes of a single trapped ion, a total of 12 incommensurate frequencies must be available. For instance, the oscillation frequencies $\omega_a = 2\pi \times 7$ MHz, $\omega_b = 2\pi \times 5$ MHz, and $\omega_c = 2\pi \times 4$ MHz (i.e. in the proportion 7:5:4 adopted in Fig. 6) would furnish 1 MHz as the free spectral interval between quantum gates. These vibrational frequencies can be achieved by engineering the trap potential through the electrodes geometry and the magnitudes of the applied external voltages. Asymmetric trap designs producing vibrational frequencies as high as 50 MHz have been demonstrated [90].

Control of the Lamb-Dicke parameters η_s, although not necessary for all quantum gates, also helps avert off-resonant excitations. Since these parameters depend on the direction of laser propagation, it is possible to mitigate undesirable excitations by em-

ploying laser beams propagating in suitable directions. The Fourier transform operation, however, requires the ability to control the Lamb-Dicke parameters by laser direction, given that it utilizes the qubit carrier frequency for the manipulation of all modes. The Fourier transform can also be made to act simultaneously on more than one mode by adapting the same idea.

The CVQC ion trap architecture utilizes the qubit degree of freedom as mediator for the interaction between modes, and as such it must remain separable from the vibrational modes once CV gates are applied. That requirement is automatically fulfilled by all Gaussian quantum gates, since in those cases the qubit remains in an eigenstate of a Pauli operator throughout the quantum evolution. The only cases in which the fulfillment of this requirement must be verified are those involving the application of non-Gaussian operations (i.e. blue- and red-sidebands), for which the saturation properties of the qubit are harnessed and thus play a role in entangling it with the vibrational modes.

Considering a single motional mode for the sake of the argument, blue- and red-sideband operations induce transitions between the basis states $g, n_s \leftrightarrow e, n_s \pm 1$ with effective coupling rates varying as $\Omega_{n_s} = \Omega_0\sqrt{n+1}$, where $\Omega_0 = \eta_s\Omega$ is the Rabi frequency for the fundamental transition $g, 0 \leftrightarrow e, 1$, in case of the blue-sideband operation, or $e, 0 \leftrightarrow g, 1$ for the red-sideband. For instance, the creation of an additional phonon on the quantum state g, n_s would require a π pulse, corresponding to the interaction time $\tau_{n_s} = \pi/\Omega_0\sqrt{n_s+1}$ which depends on n_s. Thus a general single-mode vibrational quantum state initially separable from the qubit state and written as $\psi_s = \sum_{n_s} d_{n_s} n_s$ would become entangled with the qubit after application of any of these non-Gaussian pulses.

To avoid this situation, non-Gaussian operations cannot be applied to any quantum state, but must be restricted to initial states capable of satisfying the requirement of factorization of the qubit upon completion of the quantum gate, in order to avoid mixed states at the final measurement step. The ground state is an obvious choice of initialization. A sequence of blue-sideband pulses and carrier pulses can then be applied to produce any Fock state n_a, n_b, n_c.

In the first order Lamb-Dicke approximation ($\eta \ll 1$), the phonon number of other vibrational modes, different than the ground state, does not affect the dynamics of the system. But, as a second order effect, the occupation of these modes changes the ion-light coupling strength, which causes an effective fluctuation on Rabi frequency as the number of phonons follows a thermal distribution after cooling [91,92]. However, the Lamb-Dicke parameter, which depends on the angle between the direction of oscillation of the ion and the propagation of the laser, can and should be used to minimize undesired excitations of other modes of vibration.

In truth, the class of non-Gaussian quantum states available can be increased by employing the Schwinger map. Considering a pair of modes, states with the form $n_s, 0_{s'}$

possess well defined value of $\hat{J}_z$. The beam splitter operation can then be applied to distribute the n_s quanta between the modes while keeping the qubit separable. Then two-mode non-Gaussian states are also available which are built as superpositions of the basis states $n_s, n_{s'}$ satisfying $n_s + n_{s'} = N'$, where N' is a constant.

Dimension of the motional Hilbert space

It is a useful exercise to estimate the potential limits of CVQC with the motional modes of a trapped ion. The number of modes would probably be limited to a few, owing to the requirement of frequency selectivity in the coherent manipulation. Here we estimate the limitations of the most basic architecture composed of a single trapped ion and three motional modes.

Let us first estimate the expected performance of the ion trap motional modes with proven technology. Typical large ion traps, with electrode distances on the order of 1 mm, although not built for the purpose of CVQC, can currently handle at least $N \approx 100$ phonons according to experiment [93]. The Hilbert space readily available in the three motional modes of such traps would have dimension $D \approx 10^6$. The equivalent number N_{qubit} of ions needed to produce a Hilbert space of the same dimension in the CZ paradigm would be $N_{\text{qubit}} \approx \log 10^6 / \log 2 \approx 20$. Hence we can safely estimate that transitioning to the CVQC could in principle increase the Hilbert space available in the current ion trap processor to values much larger than the best limits demonstrated to date [94].

Ultimately, the size of the Hilbert space associated with each mode is limited by anharmonicities in the trap potencial, which make the energy separation between adjacent Fock states dependent on the number of phonons. Since actual implementations of the harmonic potential can only be valid in a restricted physical volume, anarmonicities will introduce a maximum phonon number cap N per mode. Hence for a single trapped ion the three vibrational modes available would entail a Hilbert space of dimension $D \approx N^3$. To estimate practical values of N, we may consider the typical length of a long ion chain available with current technology ($\ell \approx 100$ μm) as providing the maximum attainable length for the wavefunction of a single trapped ion. Imposing $\ell \approx \sqrt{N+1}x_s$, the phonon cap would thus be limited to $N \approx (\ell/x_s)^2 \approx 10^8$. The three modes would together visit a Hilbert space of dimension $N \approx 10^{24}$. The same Hilbert space could be accessed in the CZ paradigm by employing $N_{\text{qubit}} \approx 80$ ionic qubits. This value represents the limitations imposed by the hardware on our CVQC architecture in the simplest scenario using proven technology (i.e. wherein a single trapped ion is utilized and the harmonic potential is not optimized to cover a larger volume in space).

A more stringent limit would consider the onset of undesirable effects on the CV quantum gates as they start to show dependence on the phonon number for large N. In fact, higher order terms can be neglected in the expansion of Eq. (2.2.5) only if $\eta_s^2 N \ll 1$. We hence consider $N \approx 0.01/(\eta_s^2)$ as the reasonable phonon cap of our architecture. For

laser excitation of fixed frequency, the Lamb-Dicke parameter scales with the oscillator frequency as $\omega_s^{-1/2}$. Increasing the trap stiffness thus allows for a larger Hilbert space while decreasing the interaction strength and hence extending the duration of quantum gates, which limits the maximum number of gates whithin the coherence time of the motional modes. This latter side effect could be compensated by increasing the laser power as long as off-resonant excitations can be neglected. A credible scenario considering the balance between gate speed and trap stiffness would put the Lamb-Dicke parameter at values around $\eta_s \approx 10^{-3}$, allowing for the three-mode Hilbert space to achieve the realistic dimension of $D \approx 10^{12}$. The equivalent number of qubits would be in this case $N_{\text{qubit}} \approx 40$. Interesting applications in quantum simulations already exist for a configuration space of this size [60, 95–97].

Another important aspect to consider in this trap architecture is the heating effect on the coherence time. The Innsbruck group has seen a coherence time for the vibrational state of the order of 100 ms [98] in the center of mass mode, which is consistent with voltage fluctuations expected to be around 10^{-5}, they measure the increase in the number of phonons by the observation of the Rabi oscillation signal on the blue sideband in a Ramsey experiment. Specifically, it can be seen that the creation time of one phonon is measured again by the Innsbruck group, being about 140 ms, and the decoherence time of the information stored in the vibrational mode of the order of 85 ms [99]. Furthermore, the Oxford group observed in a single calcium ion a coherence time of 182 ms for the motion state, limited by movement heating of around 3 quanta/s [100]. However, the Innsbruck group found that in the case of a chain of ions, for the axial breathing mode (and other higher axial modes) coherence times of about 5 ms are more typical [101]. Therefore, it is clear the advantage of using a single ion to protect the states of motion from decoherence.

It is known that the number of motional modes in frequency space increases with the number of ions which prohibits the addressing of single motional modes. This problem, so-called "spectral crowding", will not be, in principle, present in our system since our proposal is indeed made for a single ion, although we do not disregard as a perspective to explore the possibility of extending it to more than one atom. However if we consider the ability to scale the system for more than one ion, a possible way to overcome the problem of spectral crowding is adopting a modular design, i.e. the decomposition of the device in a larger number of interconnected traps, either using a complicated geometry to allow ions exchange from a trap to another or following a hybrid system, for example making use of photonics interfaces which, according to recent studies [102], are proving to be less and less disadvantageous in terms of noise and speed efficiency of operations, compared to an isolated ion crystal.

As a side advantage, in an actual experimental implementation scale and not in the asymptotic limit, the vibrational modes of trapped ions can be made to attain a large

Hilbert space while producing modest increase in the *physical volume* occupied by the quantum system (and thus decreasing the experimental complexity), a feature that should help protect it from environmental decoherence.

3 Single-photon generation from an atomic ensemble

Quantum technologies such as quantum networks and quantum cryptography, need a key piece: the distribution of quantum states over long distances [103].

The channels for the transmission of quantum information are mainly two, optical fibers and free space, at least for the case of qubits written in light, which is the best candidate for quantum communication for reasons of speed and size, up to now. These channels, however, have two more fundamental problems when attempting to make quantum communication over long distances, photon losses and decoherence. The most immediate problem, however, is the loss of photons.

This problem is not exclusive to quantum communication. In the processes of classic communication at long distances (telecommunication) it is standard the use of various mechanisms to overcome the losses in the system. Currently, this is primarily done by using signal amplifiers, which are nothing more than devices that generate copies of the information, and forward it to the next amplifier node, in this way they can also be referred by the name of "repeaters".

In the case of quantum communication this approach does not overcome the problem of losses due to the no-cloning theorem [104, 105]. Fortunately there is a solution to this limitation, known as the "quantum repeater", based on a more complex method employing an inherently quantum characteristic: entanglement.

The key feature of the entanglement that helps to overcome the above-mentioned limitations is that entanglement can be "swapped" [106]. To understand the entanglement swapping we start with two entangled states, the first of them entangling two systems, A and B. The second entangles, in an analogous way, the systems C and D. It is interesting to mention that none of the A or B systems need to have ever interacted with C or D. Now, if we apply a joint measurement of systems B and C, on a basis of entangled states, accompanied by a classical communication of the result to the remaining systems, it is possible to create an entangled state between A and D.

In this way, the key idea of the quantum repeater could be explained as follows: The entanglement between two points, with a distance L between them, can be achieved by entanglement swapping between two entangled pairs, each covering half of the distance

$(L/2)$. The great advantage of this approach is that its scaling is direct, i.e. to generate the entanglement at the distance $L/2$, it is enough to apply the same reasoning with two entangled pairs that are $L/4$ apart, and so on. Generally speaking, if we want to divide our distance into N equal parts, $L_0 = L/N$, small enough to be significantly unaffected by losses, we will have $n = log_2 N$ entanglement swapping operations.

For the actual implementation of this quantum repeater scheme we need to store the entanglement in one of the elemental units (links) while getting the entanglement on the other units. When two entangled pairs have been synchronized we can perform the entanglement swapping. At the next level it will also be necessary to store the information to properly perform the next entanglement swapping operation, and so on at all levels until reaching the main distance connection L.

The device performing this quantum information storage function is called a quantum memory and lies at the heart of the quantum repeater. The original proposal of quantum repeater [107] also contains other ingredients, such as for example heralded entanglement and entanglement purification. However, most of the efforts made by the scientific community have not yet gone beyond quantum memory with heralded entanglement, in order to achieve simplified architectures of quantum repeater, as a first step in the great challenge that a future quantum internet [108]would present, which is nothing more than a large quantum network of collaboration between quantum computers, through super-secure long-distance communications.

One of the great challenges of quantum information today is the realistic implementation of a quantum internet [109]. A somewhat less ambitious goal is the realization of elemental quantum networks, which are constituted by quantum nodes and channels for interconnection. The most reasonable thing seems to be, until now, to use light fields as carriers of information through optical fibers and to use matter, either as individual atoms or atomic ensembles, to implement fixed nodes (quantum memories).

From this point of view, the interface between matter and light at the quantum level is key in this technological development. The prototypical model of quantum information processing understands the concept of information as string of qubits, and performs operations through elementary quantum logic gates. A qubit is a single particle state in a Hilbert space of dimension 2. This particle can be any fundamental quantum system, such as a photon, so that it can encode information in various ways. If the coding of the states $|0\rangle$ and $|1\rangle$ is performed through polarization, these states may be the two possible linear polarizations ($|H\rangle$ and $|V\rangle$) or some change of basis from them (right and left-handed circular polarization, for example). Qubit encodings on path, number of photons, or time-bin are also common. A superposition state between $|0\rangle$ and $|1\rangle$ represents a qubit in its most general form. From these definitions we can more precisely describe the role of a quantum memory: it must be able to store strings of qubits, or parts of strings correctly and also re-emmit this information on demand. In this way, a more

elementary implementation of a quantum memory considers the simplest case of storage and delivery of information, through a photon. The generation of single photons, however, is not so simple, and has also been a topic of great interest among researchers for some time [110–112]. A standard and fairly common way of generating single photons is actually generating pairs of correlated photons and taking advantage of only one of them, leaving the other to herald the appearance of the first one [113]. This method is usually simpler to implement experimentally than an individual-photon generator device, and at the same time one can take advantage of its heralding when wants to scale this model of one link to a more complex architecture [114, 115]. In this chapter we explain the original DLCZ-protocol scheme, which is one of the most successful experimental implementations of quantum memory, proposed by Duan et al. in his seminal work published in 2001 [103]. We emphasize the symmetrical collective state in which the quantum information is stored and its relation to a two-mode squeezed vacuum. In the sequence we present a theoretical derivation of how to model a single-photon wave packet emitted in the read process of this quantum memory and how it is possible through this to understand the role played by the superradiance process in this dynamics. At the end of the chapter we discuss the scope and limitations of working on the single-photon approach.

3.1 Photon-pairs from the DLCZ-protocol scheme

3.1.1 *Single-photon generation for DLCZ*

The generation of single photons with well-defined spatial and temporal modes is an essential feature for the development of elementary logic gates, whether for quantum computation or quantum communication, among other applications. These single photons have already been studied and have been of great use in pioneering works of quantum computing [116–118]. In practice, recent works have demonstrated their wide range of use in quantum cryptography [119], scalable quantum computing [120] and especially in what most interests us, quantum networks [103, 121, 122].

In the problem of generation of single photons, there are, roughly speaking, two main approaches. The first is the generation of single photons in a deterministic way, through a "Turnstile Device" that is usually based on quantum dots or individual atoms trapped in a cavity. The second class is the conditional generation of single photons from a correlated quantum system in which a conditional measure is made. The first articles that presented this last approach for generating single photons were in photon pairs from atomic cascades [123] and spontaneous parametric down conversion (SPDC) [124]. Since more than a decade, a third strategy emerges, born naturally along with the DLCZ protocol, using thick atomic samples [125]. Other further works, although clearly still inspired by the DLCZ protocol, have made great strides not only in the generation of single photons through conditional measurements, but also in relation to the storage of

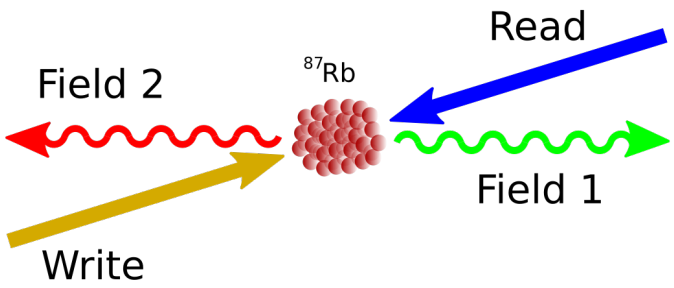

Figure 7: Schematic description for photon-pair generation from a cold atomic ensemble. First the Write classical beam is applied on the cloud generating Field 1. After a programable time, the ensemble is illuminated by the Read beam, inducing the emmision of Field 2.

these states in the atomic medium [**?**, 114, 121, 125–131].

3.1.2 *Operation of the DLCZ single-photon generator*

The operation scheme for photon-pair generation using the DLCZ scheme is detailed below.

Observing Fig. 7 we see a sample of cold atoms illuminated by 2 classical laser beams. From the atomic sample, two (non-classical) fields are emmited, oriented in counterpropagating directions, one from each other, and also in a slightly different direction to the classical fields. These 2 emmited fields are detected thanks to photo-counters that deliver this information for an analysis system that will determine the quality of the correlation between the detected photons. Classical beams are called "write" and “read”. They are aligned one against the other in a counterpropagant way, crossing the cloud of atoms more or less in the middle. The emitted beams are called “field 1” and “field 2”. The write laser is simultaneous to field 1 and the read beam is simultaneous to field 2, since fields 1 and 2, correspond to the spontaneous emissions generated from the write and read excited transitions respectively.

As shown in Fig. 7, write is the initial pulse and creates a collective excitation state in the ensemble of atoms, as may be determined by the photoelectric detection of field 1. This step is completely probabilistic. However, once a click has been detected in field 1, we can be sure that there is a collective state stored in the atomic vapor. We then let a programmable period of time δt pass, before illuminating the sample with another classic beam, the read pulse. This transforms the collective state into an excitation of the electromagnetic field, i.e. a photon whose temporal and spatial mode is well defined, the field 2. Fields 1 and 2 are quantum correlated since they violate a Cauchy-Schwartz

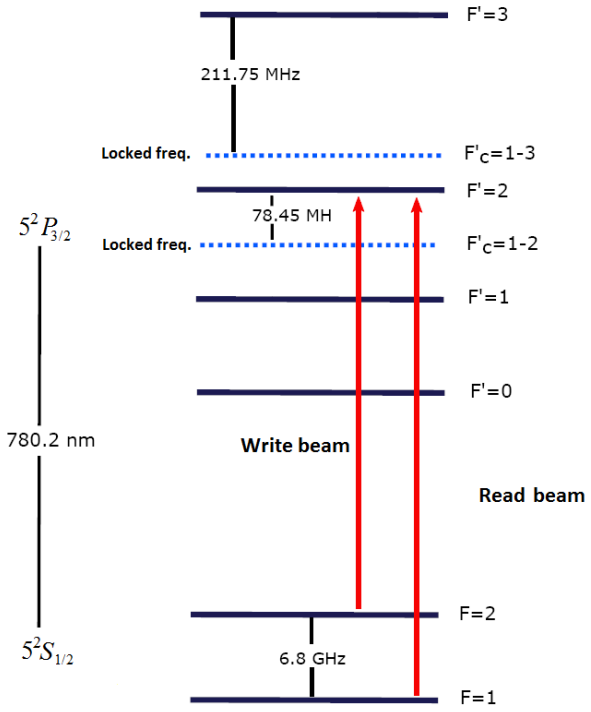

Figure 8: Two laser sources are used for all the beams in the experiment, which are locked in the cross-over between $F' = 1$ and $F' = 2$ and the cross-over between $F' = 1$ and $F' = 3$, tuning the frequencies by means of acusto-optical modulators. Write and read frequencies, related to the energy structure of ^{87}Rb, are depicted in red arrows.

inequality [125].

Observing Fig. 7 we can understand the arrangement of the beams in the experiment, in which the correlated photons are produced from a sample, that is a cloud of rubidium atoms trapped in a magneto-optical trap (MOT). The hyperfine energy levels of the ^{87}Rb participating in the experiment are shown in Fig. 8.

The protocol begins by turning off all lasers responsible for trapping and cooling for a certain period of time. During this time, a train of write and read pulses is initiated. Nevertheless, we are going to describe only a j-th write pulse with its respective read pulse, this description will be valid for all 1000 trials that occur along the train. The write beam of the j-th trial is a rectangular pulse of 52 ns duration and tuned in the transition of $|F = 2\rangle$ to $|F' = 2\rangle$. This pulse induces a spontaneous Raman scattering towards the level $|F = 1\rangle$, via $|F = 2\rangle \longrightarrow |F' = 2\rangle \longrightarrow |F = 1\rangle$. The write pulse is very weak, so to scatter a Raman photon in a forward wave packet $\psi^{(1)}\left(\vec{r}, t_j^{(1)}\right)$ occurs with a very small probability for each pulse. A photon of field 1 may then be detected with this probability. When it actually happens, it means that this photon guarantees the storage of an excitation distributed coherently and symmetrically over the N atoms illuminated by the write pulse. From this moment on, the collective excitation can be mapped in another photon, but at a later time controlled by the experimentalist, provided it is not so long that the environmental decoherence destroy the state. We define this second instant as $t_j^{(2)} = t_j^{(1)} + \delta t$. During this time $t_j^{(2)}$ we are going to illuminate the sample with a rectangular

laser pulse of 191 ns duration and resonant with the transition $|F=1\rangle \longrightarrow |F'=2\rangle$. This pulse will induce a Raman transition $|F=1\rangle \longrightarrow |F'=2\rangle \longrightarrow |F=2\rangle$, accompanied by the emission of a photon in field 2 due to the transition $|F'=2\rangle \longrightarrow |F=2\rangle$, whose wave packet is $\psi^{(1,2)}(\vec{r}, t_j^{(2)})$. This wave packet is going to be studied in more detail in the next section.

The light scattered by the write and read lasers is captured and taken to 4 avalanche photodiode detectors (APD), 2 detectors for each field (D_{1A}, D_{1B} for field 1 and D_{2A}, D_{2B} for field 2), since they are needed to study the violation of the Cauchy-Schwarz inequality as will be explained in detail later. The detection events (clicks) from field 1 are recorded within a time interval from $t_j^{(1)}$ to $t_j^{(1)} + T^{(1)}$, similarly field 2 is detected within a time window from $t_j^{(2)}$ to $t_j^{(2)} + T^{(2)}$, where $T^{(1)}(T^{(2)})$ similar to the write (read) duration.

Once a measurement has been made for long enough to accumulate statistics, we can calculate the single probabilities p_1 and p_2, of detecting a photon in each field irrespective to what happened in the other and p_{12}, the joint probability of detecting a photon at each field in the same trial. Also, the fact of having 2 detectors in each field, allows to measure probabilities of the type p_{11} and p_{22}, the probabilities of 2 detectors firing due to the same field.

The total count of singles (clicks on a detector) will be used to calculate p_1 and p_2, while coincidences (when 2 APD's have clicked on the same trial) will be useful for calculating p_{11}, p_{12} and p_{22}. So $p_1 = (n_{1A} + n_{1B})/N_{TOT}$ and $p_2 = (n_{2A} + n_{2B})/N_{TOT}$ where n_{1A}, n_{1B},n_{2A} and n_{2B} are the number of singles of each detector and N_{TOT} is the total number of trials used throughout the measurement time.

For joint detections we have to $p_{11} = N_{11}/N_{TOT}$, $p_{22} = N_{22}/N_{TOT}$ and $p_{12} = N_{12}/N_{TOT}$, where N_{11} is the number of coincidences in which both APD's of field 1 have fired, N_{22} the equivalent for field 2, N_{12} is the number of times in which an APD of field 1 and an APD of field 2 have fired in the same trial. Combinations allow to do other counts of 3 or 4 clicks in the same trial, but for now we will focus on those.

From p_1, p_2, p_{11}, p_{22} and p_{12} we can derive normalized intensity correlation functions. There are three that are going to be of more interest initially g_{11}, g_{22} and g_{12}. The first two are called autocorrelation functions and are calculated as $g_{11} = p_{11}/(p_1 p_2)$, and $g_{22} = p_{22}/(p_1 p_2)$. Similarly we have the cross-correlation function $g_{12} = p_{12}/(p_1 p_2)$.

3.1.3 *Non-classical nature of states in DLCZ*

When the sample of atoms is illuminated by the write laser, a Raman transition is induced and the emission of a photon occurs in field 1, which heralds the storage of a collective state coherently shared among all the atoms illuminated by the write beam. However we have not explained in depth so far how this happens. When a single photon is detected

in field 1, the atomic state is

$$|1_a\rangle = \frac{1}{\sqrt{N}} \sum_{i=0}^{N} |g_1\rangle \dots |s_i\rangle \dots |g_N\rangle \,, \tag{3.1.1}$$

which is a superposition of all the individual atomic states in $|g\rangle$ and only one atom in $|s\rangle$. The truth is that there are other possibilities, such as n atoms transferred to the $|s\rangle$:

$$|n_a\rangle = \left(\begin{array}{c} N \\ n \end{array} \right)^{-\frac{1}{2}} \sum_{i=0}^{N} |g_1\rangle \dots |s_i\rangle \dots |s_{i+n-1}\rangle \dots |g_N\rangle \,. \tag{3.1.2}$$

This state will be produced with a certain probability, so that the larger n, the lower that probability is. These types of states will be important in other sections of this thesis. For now we are going to study the standard DLCZ scheme that uses only the state of Eq. (3.1.1). To understand what happens to the joint state of the atomic ensemble and field 1 we are going to start by looking at the Hamiltonian that describes in a general way this dynamics

$$\hat{H} = \chi \left(\hat{a}_1^\dagger \hat{a}_a^\dagger + \hat{a}_1 \hat{a}_a \right), \tag{3.1.3}$$

where χ is a coupling constant that depends on the intensity and detuning of the laser, number of atoms, and the strengths of the transitions $|g\rangle \rightarrow |e\rangle$ and $|e\rangle \rightarrow |s\rangle$, $\hat{a}_1^\dagger$ is the photon creation operator and $\hat{a}_a^\dagger$ is the creation operator of the atomic excitation. This Hamiltonian can be obtained through the detailed derivation in [132]. It is important to mention that this Hamiltonian is formally equivalent to that of the nonlinear optical process of parametric down-conversion [133–136]. Using ordering techniques developed in [137], we can show that the application of this Hamiltonian in a two-mode vacuum state creates an entangled state. This entangled state is known in the literature as "two-mode squeezed vacuum". As this Hamiltonian represents a squeezing operation, we can now define a squeezing operator:

$$\hat{S}_{1a}(\xi) = \exp\left[\xi \hat{a}_1^\dagger \hat{a}_a^\dagger - \xi^* \hat{a}_1 \hat{a}_a \right] \tag{3.1.4}$$

where ξ is related to χ of the Hamiltonian.

Now we define the operators:

$$\hat{K}_- = \hat{a}_1 \hat{a}_a \qquad , \qquad \hat{K}_+ = \hat{a}_1^\dagger \hat{a}_a^\dagger \qquad , \qquad \hat{K}_0 = \left(\hat{a}_1 \hat{a}_1 + \hat{a}_a^\dagger \hat{a}_a^\dagger \right)/2,$$

that conform to a SU(1,1) group and define a Lie algebra:

$$\begin{aligned}\left[\hat{K}_-, \hat{K}_+\right] &= 2\hat{K}_0 \\ \left[\hat{K}_0, \hat{K}_\pm\right] &= \pm 2\hat{K}_\pm.\end{aligned}$$

Using the "Disentanglement Theorem" [138], the following equality is valid for any SU(1,1) group

$$\exp\left(\alpha_0\hat{K}_0 + \alpha_+\hat{K}_+ + \alpha_-\hat{K}_-\right) = \exp\left(\gamma_+\hat{K}_+\right)\exp\left(\ln\left[\gamma_0\hat{K}_0\right]\right)\exp\left(\gamma_-\hat{K}_-\right), \quad (3.1.5)$$

where

$$\gamma_0 = \left(\cosh\theta - \frac{\alpha_0}{2\theta}\sinh\theta\right)^{-2}, \quad (3.1.6)$$

$$\gamma_\pm = \frac{2\alpha_\pm \sinh\theta}{2\theta\cosh\theta - \alpha_0\sinh\theta}, \quad (3.1.7)$$

are the similarity constants parameterized in θ, through

$$\theta^2 = \frac{\alpha_0^2}{4} - \alpha_+\alpha_- \quad (3.1.8)$$

In our case we want to rewrite the squeezing operator of Eq. (3.1.4). Then we will focus on the case where

$$\alpha_0 = 0 \qquad , \qquad \alpha_+ = \xi \qquad , \qquad \alpha_- = -\xi^*.$$

If we write ξ in the polar form, $\xi = re^{i\phi}$, then from (3.1.8) we have

$$\theta = r.$$

From (3.1.6) and (3.1.7), we get

$$\gamma_0 = (\cosh r)^{-2} \qquad ; \qquad \gamma_\pm = \pm e^{\pm i\phi}\tanh r$$

so we can write

$$\hat{S}_{1a}(r) = e^{\left[e^{i\phi}\tanh r\right]\hat{a}_1^\dagger\hat{a}_a^\dagger} e^{\ln\left[(\cosh r)^{-2}\right]\left(\hat{a}_1^\dagger\hat{a}_1^\dagger - \hat{a}_a\hat{a}_a\right)/2} e^{\left[-e^{-i\phi}\tanh r\right]\hat{a}_1\hat{a}_a}. \quad (3.1.9)$$

Now we are going to apply this two-mode squeezing operator (with squeezing parameter r), on a two-mode vacuum state. However, before that, it is interesting to calculate some operations of creation and annihilation on a vacuum state to go ahead of what is going

to happen:

$$\begin{aligned} e^{k\hat{a}_1\hat{a}_a}0_1 0_a &= \mathbb{I}_{1a}0_1 0_a + k\hat{a}_1 0_1 \hat{a}_a 0_a + \frac{k^2}{2}\hat{a}_1^2 0_1 \hat{a}_a^2 0_a + \dots \\ &= 0_1 0_a. \end{aligned} \tag{3.1.10}$$

On the other hand we have

$$e^{k\left(\hat{a}_1^\dagger \hat{a}_1 + \hat{a}_a \hat{a}_a^\dagger\right)}0_1 0_a = e^{k\hat{a}_1^\dagger \hat{a}_1}0_1 e^{k\left(\hat{a}_a^\dagger \hat{a}_a + 1\right)}0_a. \tag{3.1.11}$$

Since the vacuum states are eigenstates of all the operators in the exponents, we can place the eigenvalues directly in the exponent

$$e^{k\hat{a}_1^\dagger \hat{a}_1}0_1 = 0_1 \tag{3.1.12}$$

$$e^{k\left(\hat{a}_a^\dagger \hat{a}_a + 1\right)}0_a = e^k 0_a. \tag{3.1.13}$$

Finally we write the squeezing operator

$$\begin{aligned} \hat{S}_{1a}(r) &= \frac{1}{\cosh r} e^{\left[e^{i\phi}\tanh r \hat{a}_1^\dagger \hat{a}_a^\dagger\right]} \\ &= \frac{1}{\cosh r}\sum_{n=1}^{\infty} e^{in\phi}(\tanh r)^n \left(\hat{a}_1^\dagger\right)^n \left(\hat{a}_a^\dagger\right)^n \end{aligned} \tag{3.1.14}$$

so that the two-mode squeezed vacuum state is

$$\hat{S}_{1a}(r)\, 0_1 0_a = \frac{1}{\cosh r}\sum_{n=1}^{\infty} e^{in\phi}\left[\tanh r\right]^n n_1 n_a. \tag{3.1.15}$$

At the limit of $r \ll 1$, $\tanh r \approx r$, $\cosh r \approx 1$, and

$$\hat{S}_{1a}(r)\, 0_1 0_a \approx 0_1 0_a + e^{i\phi} r 1_1 1_a + e^{i2\phi} r^2 2_1 2_a + \dots. \tag{3.1.16}$$

Finally, we can then say that the joint state of the atomic ensemble with field 1, for a sufficiently low write power, is

$$\psi_{1,a} = \sqrt{1-p}\left[0_1 0_a + e^{i\beta}\sqrt{p} 1_1 1_a + e^{2i\beta} p 2_1 2_a + \mathcal{O}\left(p^{3/2}\right)\right], \tag{3.1.17}$$

where we use the basis of the excitation number in the description of the state, so that n_1 corresponds to the state of field 1 with n photons, associated to the atomic state n_a which has n atoms transferred to s. The excitation probability of a single atom transferred from$g$ to s is p, and the probabilities to transfer two or more atoms of g to s associated with the presence of two or more photons in field 1 shall be equal to or less than p^2 as can be seen in the equation. We also observed a phase β determined by the propagation of the write field.

In the next step, and after a programmable time, we want to access the stored information. We send, as detailed above, a second pulse to the ensemble, the read laser, resonant with the transition $s \rightarrow e$. Thanks to this new interaction between light and the atomic medium, the symmetrical collective atomic state is transferred to another photonic mode, field 2, in the transition $e \rightarrow g$. Because of the collective effect, the probability of all atoms returning to the initial state, grows with the number of atoms squared [126] which makes the read process highly efficient. If we now look at the joint state between field 1 and field 2, we obtain a state identical to the previous one, just substituting the atomic kets by the photonic kets of field 2, so assuming efficiency equals to 1 for simplicity.

$$\begin{aligned} \psi_{1,2} &= \sqrt{1-p}\left[0_1 0_2 + e^{i\beta'}\sqrt{p}1_1 1_2 + e^{2i\beta'}p2_1 2_2 + \mathcal{O}\left(p^{3/2}\right)\right] \\ &= \sqrt{1-p}\sum_{n=0}^{\infty} {}^{in\beta'}p^{n/2}n_1, n_2. \end{aligned} \tag{3.1.18}$$

Looking at this expression we see that the phase β' now includes also the propagation of the read field. The nature of this state, as the previous one, is entangled in the basis of number of photons, in the same way as in the case of SPDC [103, 139]. It is then necessary to verify the quantum character of the process through a set of parameters and measurements. It is possible to obtain correlation functions for this characterization, through a Cauchy-Schwarz inequality for classical fields, [125]. We will use second-order correlation functions to analyze the non-classical character of the correlations between the field 1 and field 2 detections, following the Clauser approach [123] when analyzing the experimental results.

There is a set of experimental factors that will lead to the deterioration of the correlations between fields 1 and 2 photons, for example losses, mode couplings, background fluorescence, etc. Fortunately there is a single well-defined boundary between the classical and quantum domains that can be verified operationally through coincidence detection [123].

Classically, the light collected by a detector is measured as a time-average of the field intensity, given by the detector's response time. If we are considering classical fields described by complex amplitudes, the mean intensities detected for two distinct fields can be characterized by three different quantities, I_1^2, I_2^2 and $I_1 I_2$. These quantities obey a Cauchy-Schwarz inequality [123, 139, 140] valid for all classical fields:

$$I_1^2 I_2^2 \geq {I_1 I_2}^2. \tag{3.1.19}$$

When we approach the quantum limit of a weak light field, our detectors are no longer measuring the light in the same way, they do a photo-counting, in our case, both in field 1 and field 2. As already explained above, a set of probabilities that characterize the system are defined: p_1, p_2, p_{11}, p_{22} and p_{12}.

If we divide the probability of generating a pair of photons by the probability of

observing an event of accidental coincidence of each photon, we define a normalized cross-correlation function between fields 1 and 2

$$g_{12} = \frac{p_{12}}{p_1 p_2} = \frac{:\hat{I}_1\hat{I}_2:}{\hat{I}_1\hat{I}_2}. \tag{3.1.20}$$

Similarly, we can define autocorrelation functions for fields $i \in \{1, 2\}$

$$g_{ii} = \frac{p_{ii}}{p_i^2} = \frac{:\hat{I}_i^2:}{\hat{I}_i^2}. \tag{3.1.21}$$

In these correlation functions we have also placed a definition using intensity operators $\hat{I}_i$. It describes the field in a detector, after an average over the state (colon means normal ordering) in order to facilitate the connection of these quantities with the classical expressions I_1, I_2 and $I_1 I_2$.

In terms of the cross-correlation function and autocorrelation function, we can rewrite the Cauchy-Schwarz inequality 3.1.19:

$$g_{12}^2 \leq g_{11} g_{22} \tag{3.1.22}$$

and the ratio between the two sides of the previous inequality is known as the parameter R

$$R = \frac{g_{12}^2}{g_{11} g_{22}} \leq 1. \tag{3.1.23}$$

Now we are going to analyze what values we could expect for these characterization parameters from states like the two-mode squeezed vacuum obtained with our experimental apparatus.

The intensity operators are defined as

$$\hat{I}_i = \eta_i \hat{a}_i^\dagger \hat{a}_i, \tag{3.1.24}$$

where η_i is the detection efficiency and has intensity dimension.

So we rewrite g_{12} as

$$g_{12} = \frac{:\hat{a}_1^\dagger\hat{a}_1\hat{a}_2^\dagger\hat{a}_2:}{\hat{a}_1^\dagger\hat{a}_1\hat{a}_2^\dagger\hat{a}_2} = \frac{\hat{a}_1^\dagger\hat{a}_2^\dagger\hat{a}_1\hat{a}_2}{\hat{a}_1^\dagger\hat{a}_1\hat{a}_2^\dagger\hat{a}_2}, \tag{3.1.25}$$

where we have applied the normal ordering between the creation and annihilation operators.

Let's start by evaluating the mean number of photons in field 1, $\hat{a}_1^\dagger\hat{a}_1$, over the state $\psi_{1,2}$:

$$\psi_{1,2} \left| \hat{a}_1^\dagger\hat{a}_1 \right| \psi_{1,2} = \left| \hat{a}_1 \psi_{1,2} \right|^2, \tag{3.1.26}$$

where we know

$$\hat{a}_1\psi_{1,2} = \sqrt{1-p}\sum_{n=0}^{\infty} p^{n/2}\sqrt{n}n_1 - 1, n_2 \tag{3.1.27}$$

so

$$p_1 = |\hat{a}_1\psi_{1,2}|^2 = (1-p)\sum_{n=0}^{\infty} p^n n = \frac{p}{1-p}. \tag{3.1.28}$$

Similarly, by symmetry, we obtain the same result for field 2

$$\hat{a}_1^\dagger\hat{a}_1 = \hat{a}_2^\dagger\hat{a}_2 = \frac{p}{1-p} = p_2. \tag{3.1.29}$$

For the number of coincidences $\hat{a}_1^\dagger\hat{a}_2^\dagger\hat{a}_1\hat{a}_2$ we start by calculating

$$\hat{a}_1\hat{a}_2\psi_{1,2} = \sqrt{1-p}\sum_{n=0}^{\infty} p^{n/2}\sqrt{n}\sqrt{n}n_1 - 1, n_2 - 1 \tag{3.1.30}$$

so that

$$p_{12} = |\hat{a}_1\hat{a}_2\psi_{1,2}|^2 = (1-p)\sum_{n=0}^{\infty} p^n n^2 = \frac{p\,(1+p)}{(1-p)^2} \tag{3.1.31}$$

Combining the equations 3.1.28, 3.1.29 and 3.1.31 we obtain the cross-correlation function

$$g_{12} = 1 + \frac{1}{p}. \tag{3.1.32}$$

For the calculation of autocorrelations, we need $\hat{a}_i^\dagger\hat{a}_i^\dagger\hat{a}_i\hat{a}_i$

$$\hat{a}_1\hat{a}_1\psi_{1,2} = \sqrt{1-p}\sum_{n=0}^{\infty} p^{n/2}\sqrt{n}\sqrt{n-1}n_1 - 2, n_2 \tag{3.1.33}$$

so that

$$\begin{aligned} |\hat{a}_1\hat{a}_1\psi_{1,2}|^2 &= (1-p)\sum_{n=0}^{\infty} p^n n\,(n-1) \\ &= \frac{2p^2}{(1-p)^2} \end{aligned} \tag{3.1.34}$$

and

$$:\hat{I}_1^2: = \left(\hat{a}_1^\dagger\right)^2(\hat{a}_1)^2 = 2{:}\,\hat{I}_1\,{:}^2. \tag{3.1.35}$$

Therefore

$$g_{11} = \frac{:\hat{I}_1^2:}{:\hat{I}_1:^2} = 2 \tag{3.1.36}$$

and similarly, $g_{22} = 2$.

Now we are ready to calculate the parameter R, for the two-photon state $\psi_{1,2}$:

$$R = \frac{g_{12}}{g_{11}g_{22}} = \frac{\left(\frac{1+p}{p}\right)}{4} = \left(\frac{1+p}{2p}\right)^2. \tag{3.1.37}$$

As an example, if we consider $p \sim 0.1$, which can be a possible experimental value, then $R \sim 30$ and the smaller the probability p of find a pair of correlated photons, the higher the parameter R, that is to say, the greater the violation of the Cauchy-Schwarz inequality, as well as its quantum character.

A demonstration of the non-classical nature of correlations requires the measurement of R. However, since $g_{11} = g_{22} = 2$ the verification of $g_{12} > 2$ is, by itself, strong evidence of the quantum nature. To get $p \ll 1$, and therefore $g_{12} \gg 2$, we are going to use a very low power of the write beam, in order to try to produce excitations of a single photon with a small probability. This leads to a tradeoff which is an experimental challenge, since when the write power is decreased, there comes a threshold when noise introducing errors in the system begin to be more perceptible than the excitations written in the atomic ensemble.

A final measure to characterize the cooperative nature of the emission process is the probability of detecting a pair of photons, conditioned to the detection of the first of them, called p_c

$$p_c = \frac{p_{12}}{p_1} = \frac{\psi_{1,2}\left|: \hat{I}_1\hat{I}_2 :\right|\psi_{1,2}}{\psi_{1,2}\left|\hat{I}_1\right|\psi_{1,2}} = \frac{1+p}{1-p} \tag{3.1.38}$$

There is a problem with this estimate, since p_c becomes an unbounded quantity and, therefore not normalized. It is only valid in the $p \ll 1$ regime, where $p_c = 1$. In order to overcome this limitation for general situations, there is a more appropriate approach using POVM operators [141]. However given the magnitude of our probabilities, a POVM approach will be unnecessary.

3.2 Single-photon superradiance

As already explained above, the DLCZ scheme is devised to create quantum memories, which generates entangled states that last for long periods of time. The operation of this scheme consists of two parts, the writing of the state, which is very inefficient and is performed with a very low probability, and second, the reading process that is performed with high efficiency and with higher probability. This last part of the process is connected with the phenomenon of superradiance, which explains the increase of probability that comes from its high directionality [103]. After the first implementations of this process [113, 125, 142], a major development was introduced in 2005 by the use of the FWM configuration in the generation of photons [143, 144], which solved most of the

complications related to diffraction in the superradiant emission . In this configuration, the write pulse has a spatial mode considerably wider than field 1, which is coupled in fiber and detected at a small angle with respect to the direction of the write beam. In this way the optical fiber that captures field 1 defines the spatial mode of the collective state stored in the atomic vapor. On the other hand, the read pulse must have a large waist, same as the write pulse, and counterpropagate to it. Then field 2 is generated in the conjugate mode to field 1 [145]. The result of all this is a superradiant emission of photon 2 in a well-defined single-mode that can be coupled to an optical fiber with high efficiency [127]. It should be noted that the superradiance process in the emission of field 2 also modifies the emission rate of field 2 [145] as a function of the number of atoms involved in the process, which in turn can be controlled in the experiment by manipulating the optical depth of the medium. Since the atomic transitions involved in the process are narrow band, on the order of some MHz, it implies that the temporal size of the wave packet is sufficiently large to be resolved by photodetectors and photo-counting boards, that normally have sensitivity of the order of ns. In this section we study in detail the case of single-photon superradiance emitted in the reading process [146] and we also discuss the potential of studying the equivalent case when two or more photons are generated, clearly with much lower probabilities.

3.2.1 *Hamiltonian for atom-field interaction*

From the quantized description of the electromagnetic field, we can reconstruct the Hamiltonian that describes the light-atom interaction. In the electric-dipole approach, we have

$$\hat{H} = \hat{H}_A + \hat{H}_L - e\vec{r} \cdot \vec{E}, \tag{3.2.1}$$

where $\hat{H}_A$ and $\hat{H}_L$ are the free Hamiltonians for atoms (A) and light fields (L), respectively, and $\vec{r}$ is the position vector of the electron in the atom. Thus we have

$$\hat{H}_A = \sum_i E_i |i\rangle\langle i|, \tag{3.2.2}$$

$$\hat{H}_L = \sum_{\vec{k}} \hbar \left(\hat{a}^\dagger_{\vec{k}} \hat{a}_{\vec{k}} + \frac{1}{2} \right), \tag{3.2.3}$$

$$e\vec{r} = \sum_{i,j} \langle i|e\vec{r}|j\rangle |i\rangle\langle j| = \sum_{i,j} \vec{t}_{ij} |i\rangle\langle j|, \tag{3.2.4}$$

with $\{|i\rangle\}$ representing a complete set of atomic energy eigenstates, E_i being the eigenstate energy of $|i\rangle$, and $\vec{t}_{ij}$ being an element of the electric dipole transition matrix.

For the electric-dipole term in eq. (3.2.1), we consider, initially, a single atom at the origin, that is, we neglect the z dependence of the field because of the long wavelength

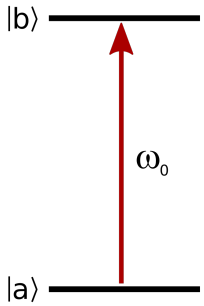

Figure 9: Two-level system with fundamental state a and excited state b. Transition frequency ω_0.

approximation. The electric field is given by $\hat{\vec{E}}(\vec{r},t) = \sum_{\vec{k}} \hat{\epsilon}_{\vec{k}} \mathcal{E}_{\vec{k}} \hat{a}_{\vec{k}} \exp\left(-i\omega_{\vec{k}} t + i\vec{k}\cdot\vec{r}\right) + H.c.$, with $\mathcal{E}_{\vec{k}} = \left(\frac{\hbar\omega_{\vec{k}}}{2\epsilon_0 V}\right)^{1/2}$, $\hat{\epsilon}_{\vec{k}}$ polariazation, and V a quantization volume. Note that the field in this equation depends on time. We introduce the field in this way to facilitate the connection with our classical view of the field, but the quantum treatment divides the description of the physical systems between operators and states. In Schrödinger representation all temporal dependence is in the quantum state and not in the operator, so that the quantized electric field operator becomes

$$\hat{\vec{E}} = \sum_{\vec{k}} \hat{\epsilon}_{\vec{k}} \mathcal{E}_{\vec{k}} \left(\hat{a}_{\vec{k}} + \hat{a}^{\dagger}_{\vec{k}}\right). \tag{3.2.5}$$

For simplicity, we also consider a basis of linear polarization and the polarization versors as being reals. Finally, let us remember that the temporal dependence of light will again emerge in the Schrödinger representation. Substituting Eqs. 3.2.2 to 3.2.5 into Eq. 3.2.1, we get

$$\hat{H} = \sum_{\vec{k}} \hbar\omega_{\vec{k}} \hat{a}^{\dagger}_{\vec{k}} \hat{a}_{\vec{k}} + \sum_i E_i |i\rangle\langle i| + \hbar \sum_{i,j} \sum_{\vec{k}} g^{ij}_{\vec{k}} |i\rangle\langle j| \left(\hat{a}_{\vec{k}} + \hat{a}^{\dagger}_{\vec{k}}\right), \tag{3.2.6}$$

where

$$g^{ij}_{\vec{k}} = -\frac{\vec{t}_{ij}\cdot\hat{\epsilon}_{\vec{k}}\mathcal{E}_{\vec{k}}}{\hbar}. \tag{3.2.7}$$

In Eq. 3.2.6, we have omitted the zero-point energy of the first term, since it implies in a constant level of energy. Also for simplicity we consider $\vec{t}_{ij}$ real.

3.2.2 *Two-level atom*

We now consider the case of a 2-level atom $\{|a\rangle, |b\rangle\}$, as depicted in figure 9. For $g^{ab}_{\vec{k}}$ real, we get

$$g_{\vec{k}} = g^{ab}_{\vec{k}} = g^{ba}_{\vec{k}}. \tag{3.2.8}$$

It follows that the Hamiltonian 3.2.6 reads

$$\hat{H} = \sum_{\vec{k}} \hbar\omega_{\vec{k}} \hat{a}^{\dagger}_{\vec{k}} \hat{a}_{\vec{k}} + E_a|a\rangle\langle a| + E_b|b\rangle\langle b| + \hbar \sum_{\vec{k}} g_{\vec{k}} \left(|a\rangle\langle b| + |b\rangle\langle a|\right) \left(\hat{a}_{\vec{k}} + \hat{a}^{\dagger}_{\vec{k}}\right). \quad (3.2.9)$$

Defining the atomic raising $\hat{\sigma}^+$ and lowering $\hat{\sigma}^-$ operators

$$\hat{\sigma}^+ = |b\rangle\langle a|, \quad (3.2.10)$$

$$\hat{\sigma}^- = |a\rangle\langle b|, \quad (3.2.11)$$

and taking $E_a = 0$, we can write

$$\hat{H} = \sum_{\vec{k}} \hbar\omega_{\vec{k}} \hat{a}^{\dagger}_{\vec{k}} \hat{a}_{\vec{k}} + E_b|b\rangle\langle b| + \hbar \sum_{\vec{k}} g_{\vec{k}} \left(\hat{\sigma}^+ \hat{a}_{\vec{k}} + \hat{\sigma}^- \hat{a}^{\dagger}_{\vec{k}} + \hat{\sigma}^+ \hat{a}^{\dagger}_{\vec{k}} + \hat{\sigma}^- \hat{a}_{\vec{k}}\right). \quad (3.2.12)$$

The interaction energy in the Hamiltonian 3.2.12 consists in 4 terms. The first one, $\hat{\sigma}^+ \hat{a}_{\vec{k}}$, represents a situation in which one atom is excited to the level $|b\rangle$ at the same time that one photon disappears from the field. The second term, $\hat{\sigma}^- \hat{a}^{\dagger}_{\vec{k}}$, represents the inverse process. Energy is conserved in both processes. Now for the third term, $\hat{\sigma}^+ \hat{a}^{\dagger}_{\vec{k}}$, we would have a process with an energy gain of approximately $2\hbar\omega_0$. In an analogous way, the term $\hat{\sigma}^- \hat{a}_{\vec{k}}$ implies in a loss of energy of $\sim 2\hbar\omega_0$. Neglecting these terms that don't conserve energy corresponds to the rotating wave approximation. The resulting Hamiltonian

$$\hat{H} = \sum_{\vec{k}} \hbar\omega_{\vec{k}} \hat{a}^{\dagger}_{\vec{k}} \hat{a}_{\vec{k}} + E_b|b\rangle\langle b| + \hbar \sum_{\vec{k}} g_{\vec{k}} \left(\hat{\sigma}^+ \hat{a}_{\vec{k}} + \hat{\sigma}^- \hat{a}^{\dagger}_{\vec{k}}\right), \quad (3.2.13)$$

will be the starting point of all the treatment that follows.

3.2.3 *Spontaneous emission in 2-level atoms (Weisskopf-Wigner Theory)*

If we want to treat the temporal evolution of the 2-level atom in free space, we need the Hamiltonian of Eq. 3.2.13:

$$\hat{H} = \sum_{\vec{k}} \hbar\omega_{\vec{k}} \hat{a}_{\vec{k}} + E_b|b\rangle\langle b| + \hbar \sum_{\vec{k}} \left[g_{\vec{k}}\left(\vec{r}_0\right) \hat{\sigma}^+ \hat{a}_{\vec{k}} + \text{H. c.}\right]. \quad (3.2.14)$$

where we come to consider $g^*_{\vec{k}}\left(\vec{r}\right) = g_{\vec{k}} \exp\left(-i\vec{k}\cdot\vec{r}\right)$ as complex to include the dependence of the spatial phase on the position of the atom.

The interaction potential in the interaction picture will then be

$$\hat{V}_I = \hbar \sum_{\vec{k}} \left[g_{\vec{k}}\left(\vec{r}_0\right) \hat{\sigma}^+ \hat{a}_{\vec{k}} e^{i(\omega_0 - \omega_{\vec{k}})t} + \text{H. c.}\right]. \quad (3.2.15)$$

We assume that in $t = 0$ the atom is on the excited level $|b\rangle$ and the field is in the

vacuum mode $|0\rangle$. The state vector then evolves into a space of eigenstates restricted in maximum to $n = 1$ for the number of photons in the field:

$$|\psi(t)\rangle_I = c_b(t)|b, 0\rangle + \sum_{\vec{k}} c_{a,\vec{k}}|a, 1_{\vec{k}}\rangle, \tag{3.2.16}$$

with

$$c_b(0) = 1 \qquad \text{and} \qquad c_{a,\vec{k}}(0) = 0. \tag{3.2.17}$$

Note that the eigenstate $|a, 0\rangle$ does not participate in the evolution either. To determine the temporal evolution of the system, we use

$$\frac{\partial|\psi(t)\rangle_I}{\partial t} = -\frac{i}{\hbar}\hat{V}_I|\psi(t)\rangle_I, \tag{3.2.18}$$

from which follows that

$$\begin{aligned}\frac{\partial c_b(t)}{\partial t} &= -\frac{i}{\hbar}\langle b, 0|\hat{V}_I|\psi(t)\rangle_I \\ &= -i\sum_{\vec{k}} g_{\vec{k}}\,(\vec{r}_0)\, e^{i(\omega_0-\omega_{\vec{k}})t} c_{a,\vec{k}},\end{aligned} \tag{3.2.19}$$

$$\begin{aligned}\frac{\partial c_{a,\vec{k}}(t)}{\partial t} &= -\frac{i}{\hbar}\langle a, 1_{\vec{k}}|\hat{V}_I|\psi(t)\rangle \\ &= -ig^*_{\vec{k}}\,(\vec{r}_0)\, e^{-i(\omega_0-\omega_{\vec{k}})t} c_{b,}(t).\end{aligned} \tag{3.2.20}$$

Let's now integrate Eq. 3.2.20 up to any instant t:

$$c_{a,\vec{k}}(t) = -ig^*_{\vec{k}}\,(\vec{r}_0)\int_0^t dt' e^{-i(\omega_0-\omega_{\vec{k}})t'} c_b(t'), \tag{3.2.21}$$

where we use the fact that $c_{a,\vec{k}}(0) = 0$. Substituting 3.2.21 in 3.2.19, we get

$$\frac{\partial c_b}{\partial t} = -\sum_{\vec{k}} |g_{\vec{k}}\,(\vec{r})\,|^2 \int_0^t dt' e^{i(\omega_0-\omega_{\vec{k}})(t-t')} c_b(t'). \tag{3.2.22}$$

So far no approximation has been made. From here we make approximations considering the distribution of vacuum modes. Assuming that the field modes are closely spaced in frequency, the sum in $\vec{k}$ may be replaced by an integral:

$$\sum_{\vec{k}} \to 2\frac{V}{(2\pi)^3}\int d^3\vec{k} \underbrace{\longrightarrow}_{\text{Sph. coord}} 2\frac{V}{(2\pi)^3}\int_0^\infty dk \int_0^\pi d\theta \int_0^{2\pi} d\varphi k^2 \sin\theta, \tag{3.2.23}$$

where V is the quantization volume. In addition, from eq. 3.2.7 and definition of $\mathcal{E}_{\vec{k}}$, we

have

$$|g_{\vec{k}}(\vec{r}_0)|^2 = \frac{\omega_{\vec{k}}}{2\hbar\epsilon_0 V} t_{ij}^2 \cos^2\theta, \tag{3.2.24}$$

where θ is the angle between the atomic dipole moment $\vec{t}_{ij}$ and the versors $\hat{\epsilon}_{\vec{k}}$ of the polarization of the electric field. Note that the integral 3.2.23 scans all possible vectors $\vec{k}$, however it is from Eq. 3.2.24 that the coordinate axis of the problem are defined. Using Eqs. 3.2.23 and 3.2.24 in 3.2.22, we have

$$\begin{aligned}\frac{\partial c_b}{\partial t} =& -\frac{t_{ij}^2}{(2\pi)^3\hbar\epsilon_0}\underbrace{\int_0^{\pi} d\theta \sin\theta\cos^2\theta}_{2/3}\underbrace{\int_0^{2\pi} d\varphi}_{2\pi}\int_0^{\infty}\underbrace{dk k^2}_{d\omega_{\vec{k}}\frac{\omega_{\vec{k}}^2}{c^3}}\omega_{\vec{k}}\int_0^t dt' e^{i(\omega_0-\omega_{\vec{k}})(t-t')}c_b(t') \\ =& -\frac{2t_{ij}^2}{(2\pi)^2\hbar\epsilon_0 3c^3}\int_0^{\infty} d\omega_{\vec{k}}\omega_{\vec{k}}^3\int_0^t dt' e^{i(\omega_0-\omega_{\vec{k}})(t-t')}c_b(t'). \end{aligned}\tag{3.2.25}$$

The time integral in Eq. 3.2.25 will lead to negligible values unless $\omega_{\vec{k}} \approx \omega_0$. Around this value $\omega_{\vec{k}}^3$ does not vary much, and the integral in $\omega_{\vec{k}}$ can be formally extended to $-\infty$. Therefore Eq. 3.2.25 reads

$$\frac{\partial c_b}{\partial t} = -\frac{2t_{ij}^2\omega_0^3}{(2\pi)^2\hbar\epsilon_0 3c^3}\int_0^t dt' c_b(t')\underbrace{\int_{-\infty}^{\infty} d\omega_{\vec{k}} e^{i(\omega_0-\omega_{\vec{k}})(t-t')}}_{2\pi\delta(t-t')} \tag{3.2.26}$$

$$\Rightarrow \frac{\partial c_b}{\partial t} = -\frac{\Gamma}{2}c_b(t), \tag{3.2.27}$$

with

$$\Gamma = \frac{1}{4\pi\epsilon_0}\frac{4\omega_0^3 t_{ij}^3}{3\hbar c^3}. \qquad \text{(spontaneous decay rate)} \tag{3.2.28}$$

It follows that

$$\rho_{bb} = |c_b(t)|^2 = e^{-\Gamma t}. \tag{3.2.29}$$

We then show that an atom initially in the excited state $|b\rangle$ in the vacuum decays exponentially with time to the state $|a\rangle$ with a lifetime of $\tau = 1/\Gamma$.

3.2.4 *Collective quantum memory*

We will now explore more "exotic" consequences of the first principles treatment of spontaneous emission. We consider a system that has memory: an ensemble of 3-level atoms in lambda-like configuration, where we initially pump all atoms to one of the fundamental levels, $|g\rangle$, see Fig. 10. The other fundamental level is $|s\rangle$ and $|e\rangle$ is the excited level. The system is excited by a "write" field $\vec{E}_W$ acting in the transition $g \to e$ and quite detuned, by Δ, with respect to resonance. This field acts in the form of a weak square pulse for ease of calculation. With a small probability, a spontaneous emission in the transition

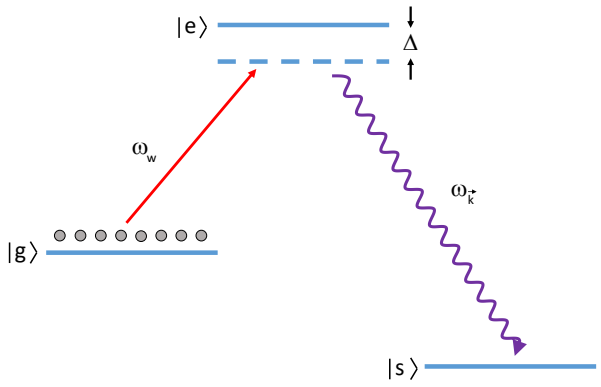

Figure 10: Lambda configuration

$e \to s$ may occur and an atom is transferred from $|g\rangle$ to $|s\rangle$. This process is often called spontaneous Raman transition. The write field can be an intense laser, so we will model it by a classical field of amplitude $\mathcal{E}_W$ inducing a Rabi frequency

$$\Omega_{W,i} = \frac{\mu_{ge}\mathcal{E}_W}{\hbar} e^{-i\vec{k}_W \cdot \vec{r}_i} \tag{3.2.30}$$

for the excitation of the transition $g \to e$. For the transition $e \to s$, each mode $\vec{k}$ of the vacuum acts with an effective Rabi frequency given by the coupling constant

$$g^*_{\vec{k},i} = \mu_{es} \left(\frac{\omega_{\vec{k}}}{2\hbar\epsilon_0 V} \right)^{1/2} e^{-i\vec{k}\cdot\vec{r}_i}, \tag{3.2.31}$$

where $\vec{r}_i$ indicates the position of the i-th atom. We therefore include the spatial phase of the fields at the respective complex Rabi frequencies. Whereas Δ is much larger than the natural decay rate Γ of level $|e\rangle$, we can then eliminate adiabatically the excited level and describe the Raman process as a direct transition $g \to s$ with the two-photon Rabi frequency

$$\Omega_{\vec{k},i} = \frac{\Omega_{W,i} g^*_{\vec{k},i}}{2\Delta} \tag{3.2.32}$$

The effective Hamiltonian of the two-photon transition is then

$$\hat{H}_f = \sum_{\vec{k}} \hbar\omega_{\vec{k}} \hat{a}^\dagger_{\vec{k}} \hat{a}_{\vec{k}} + \sum_{i=1}^{N_a} \left[E_g |g_i\rangle\langle g_i| + E_s |s_i\rangle\langle s_i| \right] + \hbar \sum_{\vec{k}} \sum_{i=1}^{N_a} \left[\Omega_{\vec{k},i} e^{i\omega_W t} \hat{\sigma}^+_i \hat{a}_{\vec{k}} + H.c. \right], \tag{3.2.33}$$

with

$$\begin{cases} \hat{\sigma}^+_i = |g_i\rangle\langle s_i|, \\ \hat{\sigma}^-_i = |s_i\rangle\langle g_i|. \end{cases} \tag{3.2.34}$$

the Stark shifts are not critical to the discussion that follows, and can be directly incorporated from redefinitions of E_g and E_s.

The first two terms of Eq. 3.2.33 then provide the free Hamiltonian $\hat{H}_F$ and the last term is the interaction potential $\hat{V}$. To work on the interaction picture, we must therefore calculate

$$\begin{aligned}\hat{V}_I &= e^{i\hat{H}_L t/\hbar}\hat{V}e^{-i\hat{H}_L t/\hbar} \\ &= \hbar\sum_{\vec{k}}\sum_{i=1}^{N_a}\left[\Omega_{\vec{k},i}e^{i\omega_W t}e^{-i\omega_{\vec{k}}t}e^{i(E_g-E_s)t/\hbar}\hat{\sigma}_i^+\hat{a}_{\vec{k}} + H.c.\right],\end{aligned} \tag{3.2.35}$$

where we used

$$\begin{aligned}&e^{i[E_g|g_i\rangle\langle g_i|+E_s|s_i\rangle\langle s_i|]t/\hbar}|g_i\rangle\langle s_i|e^{-i[E_g|g_i\rangle\langle g_i|+E_s|s_i\rangle\langle s_i|]t/\hbar} = \\ &= |g_i\rangle\langle s_i| + \frac{it}{\hbar}\left[E_g|g_i\rangle\langle g_i| + E_s|s_i\rangle\langle s_i|, |g_i\rangle\langle s_i|\right] \\ &+ \frac{1}{2!}\left(\frac{it}{\hbar}\right)^2\left[E_g|g_i\rangle\langle g_i| + E_s|s_i\rangle\langle s_i, [E_g|g_i\rangle\langle g_i| + E_s|s_i\rangle\langle s_i|\,|g_i\rangle\langle s_i|]\right] + \ldots \\ &= |g_i\rangle\langle s_i| + \frac{i\left(E_g-E_s\right)t}{\hbar}|g_i\rangle\langle s_i| + \frac{1}{2!}\left[\frac{i\left(E_g-E_s\right)t}{\hbar}\right]^2|g_i\rangle\langle s_i| + \ldots \\ &= \hat{\sigma}_i^+ e^{i(E_g-E_s)t/\hbar}.\end{aligned} \tag{3.2.36}$$

Defining $\omega_{gs} = \dfrac{E_g - E_s}{\hbar}$, Eq. 3.2.35 reads

$$\hat{V}_I(t) = \hbar\sum_{\vec{k}}\sum_{i=1}^{N_a}\left[\Omega_{\vec{k},i}e^{i(\omega_W+\omega_{gs}-\omega_{\vec{k}})t}\hat{\sigma}_i^+\hat{a}_{\vec{k}} + H.c.\right]. \tag{3.2.37}$$

The initial state of the system is given by

$$|\psi(t=0)\rangle_I = |g_1, g_2, \ldots, g_i, \ldots, g_{N_a}\rangle|0\rangle = |g, 0\rangle, \tag{3.2.38}$$

with all N_a atoms in state $|g\rangle$ and the field in the transition $e \to s$ in the vacuum state $|0\rangle$.

It follows that the state of the system in an instant t can be calculated from

$$|\psi(t)\rangle_I = \hat{U}_I(t,0)|\psi(0)\rangle_I, \tag{3.2.39}$$

with $\hat{U}_I(t,0)$ the temporal propagation operator in the interaction picture. In terms of the Dyson series for $\hat{U}(t,0)$, eq. 3.2.39 can be rewritten as

$$|\psi(t)\rangle_I = |g,0\rangle + \left(-\frac{i}{\hbar}\right)\int_0^t dt'\hat{V}_I(t')|g,0\rangle + \left(-\frac{i}{\hbar}\right)^2\int_0^t dt'\int_0^{t'} dt''\hat{V}_I(t')\hat{V}_I(t'')|g,0\rangle + \ldots. \tag{3.2.40}$$

Substituting Eq. 3.2.37 in 3.2.40, we have

$$
\begin{aligned}
|\psi(t)\rangle_I = |g,0\rangle &+ (-i)\sum_{\vec{k}}\sum_{i=1}^{N_a}\Omega^*_{\vec{k},i}\int_0^t dt' e^{-i(\omega_W+\omega_{gs}-\omega_{\vec{k}})t'}|s_i,1_{\vec{k}}\rangle \\
&+ (-i)^2\sum_{\vec{k},\vec{k}'}\sum_{i,j=1}^{N_a}\Omega^*_{\vec{k},i}\Omega^*_{\vec{k}',j}\int_0^t dt'\int_0^{t'} dt'' e^{-i(\omega_W+\omega_{gs}-\omega_{\vec{k}'})t'}e^{-i(\omega_W+\omega_{gs}-\omega_{\vec{k}})t''}|s_i,s_j;1_{\vec{k}},1_{\vec{k}'}\rangle \\
&+ (-i)^2\sum_{\vec{k},\vec{k}'}\sum_{i,j=1}^{N_a}|\Omega_{\vec{k},i}|^2\int_0^t dt'\int_0^{t'} dt'' e^{i(\omega_W+\omega_{gs}-\omega_{\vec{k}})t'}e^{-i(\omega_W+\omega_{gs}-\omega_{\vec{k}})t''}|g,0\rangle \\
&+ \ldots
\end{aligned}
\tag{3.2.41}
$$

where we define

$|s_i,1_{\vec{k}}\rangle \equiv$ state with all atoms in $|g\rangle$ except the atom i, that is in $|s\rangle$; the field is the vacuum plus a photon in mode $\vec{k}$.

$|s_i,s_j;1_{\vec{k}},1_{\vec{k}'}\rangle \equiv$ state with all atoms in $|g\rangle$ except the atoms i and j that are in $|s\rangle$; the field is the vacuum plus two photons, one in mode $\vec{k}$ and another in $\vec{k}'$.

The state of Eq. 3.2.41 presents intricate entanglement between the atomic state and the light modes. To explore many of the consequences of this kind of entanglement, it is enough to focus on the first order term on Ω. Let us then consider a physical situation in which Ω is small enough to allow us to keep only the first-order term in the series of Eq. 3.2.41:

$$
|\psi(t)\rangle \approx |g,0\rangle + (-i)\sum_{\vec{k}}\sum_{i=1}^{N_a}\Omega^*_{\vec{k},i}\int_0^t dt' e^{-i(\omega_W+\omega_{gs}-\omega_{\vec{k}})t'}|s_i,1_{\vec{k}}\rangle. \tag{3.2.42}
$$

The quantum entanglement in Eq. 3.2.42 is that of a photon in the light mode with an atomic collective state where an atom has been transferred to the state $|s\rangle$, but we do not know which one. The light mode in Eq. 3.2.42, however, is not very well defined. In principle, the photon $\left|1_{\vec{k}}\right\rangle$ can point in any direction. This problem can be overcome by concentrating on a single mode of emission, which will then be entangled with a single well-defined collective mode. For this, the first step is to use a write beam that can be approximated by a plane wave, that is, for which we can neglect the variation of $\mathcal{E}_W$ in the transverse direction to the propagation of the beam. Next, we consider the projection in a specific mode $\hat{a}_1$ of the field, which we name 1. This mode can be written as a superposition of modes $\hat{a}_{\vec{k}}$ of plane wave that we have been working up to here:

$$
\hat{a}_1 = \int d\vec{q}_1\phi_1(\vec{q}_1)\hat{a}_{\vec{q}_1+\sqrt{k_1^2-q_1^2}\hat{z}}, \tag{3.2.43}
$$

with $\vec{q}_1$ a two-dimensional vector in the transverse plane of $\vec{k}_1$, with $k_1 = \omega_1/c$. The mode

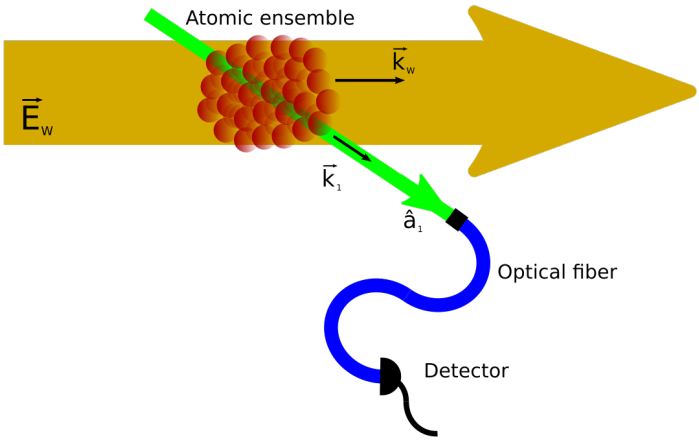

Figure 11: Gaussian mode defined by the optical fiber

$\hat{a}_1$ is, therefore, an arbitrary superposition of plane waves around the direction $\vec{k}_1$. The function $\phi_1(\vec{q}_1)$ defines the mode, that we consider to be monochromatic. A quantum state with a photon in this mode can be written as $\hat{a}_1^\dagger|0\rangle$, so that the projection in that state is made from the operator $\langle 0|\hat{a}_1$. The form of the eq. 3.2.43 allows, for example, to define $\hat{a}_1$ as a Gaussian mode within the paraxial approximation (of propagation close to an axis such as $\vec{k}_1$). Such modes can be commonly obtained from resonant cavities or optical fibers. A possible physical situation with $\hat{a}_1$ being a Gaussian mode is shown in the figure 11. In the discussion above, we assumed a well defined frequency ω_1. This frequency selection happens through the time integral of Eq. 3.2.42. Let's consider the state of the system after the action of the write pulse of temporal width T_p and already transforming the summation over $\vec{k}$ into an integral:

$$|\psi(t\rangle T_p)\rangle_I = |g,0\rangle + \frac{(-i)2V}{(2\pi)^3}\int d^3\vec{k}\sum_{i=1}^{N_a}\Omega^*_{\vec{k},i}\int_0^{T_p} dt' e^{-i(\omega_W+\omega_{gs}-\omega_{\vec{k}})t'}|s_i,1_{\vec{k}}\rangle. \tag{3.2.44}$$

From the definition of $\Omega^*_{\vec{k},i}$, Eq. 3.2.32, we have

$$\Omega^*_{\vec{k},i} = \frac{\Omega^*_{W,i}g_{\vec{k},i}}{2\Delta} = \frac{\mu_{ge}\mu_{es}\mathcal{E}_W}{(2\hbar)^{3/2}\Delta(\epsilon_0 V)^{1/2}}e^{i\vec{k}_W\cdot\vec{r}_i}\omega_{\vec{k}}^{1/2}e^{-i\vec{k}\cdot\vec{r}_i}. \tag{3.2.45}$$

Note that in the usual treatment of spontaneous emission, it was necessary to take into account an angle between the atomic polarization and an arbitrary polarization of the emitted electric field. The arbitrary direction of polarization in that case came mainly from the arbitrary $\vec{k}$. In the situation we are now considering, the direction of $\vec{k}$ is approximately fixed, so that the two possible polarization-vector directions are also fixed, parallel or perpendicular to the direction of the polarization of the write beam (which we

can take as the quantization axis). In any case, the transition to $|s\rangle$ will occur only if $g_{\vec{k},i}$ couples the polarization of the field to its atomic polarization parallel to it. We can thus consider as zero the angle between these two vectors. A more detailed description of this aspect of the problem would have required the introduction of the Zeeman structure of the atom into our model [126]. Substituting Eq. 3.2.45 in 3.2.44:

$$|\psi(t\rangle T_p)\rangle_I = |g,0\rangle + \frac{(-i)\mu_{ge}\mu_{es}\mathcal{E}_W V^{1/2}}{\hbar^{3/2}\Delta(2\epsilon_0)^{1/2}(2\pi)^3}\sum_{i=1}^{N_a} e^{i\vec{k}_W\cdot\vec{r}_i}\int d^3\vec{k}\,\omega_{\vec{k}}^{1/2}e^{-i\vec{k}_W\cdot\vec{r}_i} \int_0^{T_p} dt' e^{-i(\omega_W+\omega_{gs}-\omega_{\vec{k}})t'}|s_i,1_{\vec{k}}\rangle. \tag{3.2.46}$$

In spherical coordinates, the integral above is

$$\int_0^{\pi} d\theta\sin\theta\int_0^{2\pi} d\varphi\int_0^{\infty}\frac{d\omega_{\vec{k}}\omega_{\vec{k}}^2}{c^3}\cdot\omega_{\vec{k}}^{1/2}e^{-ik(\cos\theta z_i+\sin\theta\cos\varphi x_i+\sin\theta\sin\varphi y_i)}\times \times\int_0^{T_p} dt' e^{-i(\omega_W+\omega_{gs}-\omega_{\vec{k}})t'}|s_i,1_{\vec{k}}\rangle. \tag{3.2.47}$$

If T_p is long enough, the time integral implies that $\omega_{\vec{k}}$ have a value around $\omega_1 = \omega_W + \omega_{gs}$ and can be approximated by

$$\int_0^{T_p} dt' e^{-i(\omega_i-\omega_{\vec{k}})t'} \approx \delta(\omega_i - \omega_{\vec{k}}), \tag{3.2.48}$$

which replacing in 3.2.47 results in

$$\frac{\omega_1^{5/2}}{c^3}\int_0^{\pi} d\theta\sin\theta\int_0^{2\pi} d\varphi e^{-ik_1(\cos\theta z_i+\sin\theta\cos\varphi x_i+\sin\theta\sin\varphi y_i)}|s_i,1_{\vec{k}}\rangle. \tag{3.2.49}$$

Note that we have already chosen the axis z as the direction of the mode we want to detect. The Eq. 3.2.49 involves a general sum over modes with constant modulus of $\vec{k}$, $|\vec{k}| = k_1$. Now we have to perform the projection in the detected mode:

$$\begin{aligned}\langle 0|\hat{a}_1|\psi(t>T_p)\rangle_I =& \frac{(-i)\mu_{ge}\mu_{es}\mathcal{E}_W V^{1/2}\omega_1^{5/2}}{\hbar^{3/2}\Delta(2\epsilon_0)^{1/2}(2\pi)^3c^3}\sum_{i=1}^{N_a} e^{i\vec{k}_W\cdot\vec{r}_i}\int_0^{\pi} d\theta\sin\theta \\ &\times\int_0^{2\pi} d\varphi e^{-ik_1(\cos\theta z_1+\sin\theta\cos\varphi x_i+\sin\theta\sin\varphi y_i)}\langle 0|\hat{a}_1|s_i,1_{\vec{k}}\rangle, \\ =& \frac{(-i)\mu_{ge}\mu_{es}\mathcal{E}_W V^{1/2}\omega_1^{5/2}}{\hbar^{3/2}\Delta(2\epsilon_0)^{1/2}(2\pi)^3c^3}\sum_{i=1}^{N_a} e^{i\vec{k}_W\cdot\vec{r}_i} \\ &\int d\vec{q}_1\phi_1(q_1)e^{-i(\vec{q}_1+\sqrt{k_1^2-q_1^2}\hat{z})\cdot\vec{r}_i}|s_i\rangle,\end{aligned} \tag{3.2.50}$$

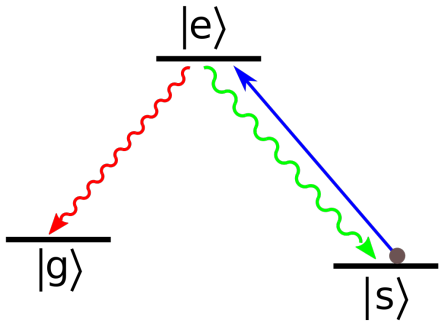

Figure 12: Reading process, a classical laser induce a superradiant emission of field 2.

or even

$$\langle 0|\hat{a}_1|\psi(t>T_p)\rangle_I = \frac{(-i)\mu_{ge}\mu_{es}\mathcal{E}_W V^{1/2}\omega_1^{5/2}\sqrt{N_a}}{\hbar^{3/2}\Delta(2\epsilon_0)^{1/2}(2\pi)^3 c^3}|1_a\rangle, \tag{3.2.51}$$

with

$$|1_a\rangle = \frac{1}{\sqrt{N_a}}\sum_{i=1}^{N_a} c_i e^{i(\vec{k}_W - k_1\hat{z})}|s_i\rangle, \tag{3.2.52}$$

and

$$c_i = \int d\vec{q}_1 \phi_1(\vec{q}_1) e^{i[-\vec{q}_1\cdot\vec{\rho}_i + z_i q_1^2/2k_1]}. \tag{3.2.53}$$

$\vec{\rho}_i$ is component of $\vec{r}_i$ in the XY plane and we have

$$\sum_i |c_i|^2 = \int d\vec{q}_1 \int d\vec{q}_1' \phi_1(\vec{q}_1)\phi_1(\vec{q}_1') \underbrace{\sum_i e^{i\left[-(\vec{q}_1-\vec{q}_1')\cdot\vec{\rho}_i + z_i\left(\frac{q_1^2}{2k_1} - \frac{q_1'^2}{2k_1}\right)\right]}}_{\approx\delta(\vec{q}_1-\vec{q}_1')}$$

$$\underbrace{\int d\vec{q}_1 |\phi_1(\vec{q}_1)|^2}_{\Downarrow \text{ mode } \hat{a}_1 \text{ normalized}} = 1. \tag{3.2.54}$$

Equation 3.2.51 provides, in a simplified way, the result of the projection of the atomic state due to the detection of a photon in mode 1. Once this detection has occurred, the resulting state needs to be normalized again, leading to the final state of the detection process

$$|\psi_f\rangle_I = |1_a\rangle. \tag{3.2.55}$$

This is a macroscopic collective entangled state, where we have an atom of the ensemble in the state s, but we do not know which one. Each atom is excited with a different amplitude and phase, given by the coefficient $c_i e^{i(\vec{k}_W - k_1\hat{z})}$, but fixed. The important point is to notice that detecting a photon in mode 1 "prepared" the ensemble in a very well defined collective state, which can be exploited in different contexts from now on.

The first important property of the state of Eq. 3.2.55 is its possibility of conversion to a second mode of the light field, field 2, with high efficiency. In what follows, we discuss

in detail this conversion process. We begin with the incidence of another intense field, the read field, in the transition $s \to e$. Just as for the write field, we can describe it as a classical field. We act with the read field in resonance because of two reasons: to increase the probability of the mapping $|s\rangle \to |e\rangle$, and to induce transparency in the medium to increase the extraction efficiency of light emitted in the transition $e \to g$, since it prevents the emission from the reabsorption effects. The read beam therefore also needs to be intense. Once excited to level $|e\rangle$, the atom can decay spontaneously to the levels $|g\rangle$ or $|s\rangle$, as depicted in Figure 12. It is important to keep in mind from the beginning that the process $s \to e \to g$ must be much more probable, because here all the atoms end in the same state of the ensemble $|g_1, g_2, \ldots, g_n\rangle$. This results in a large constructive interference reinforcing a global parametric process (same initial and final state), with conservation of momentum and energy in the atomic environment. Even so, taking into account also the $s \to e \to s$ helps in obtaining a better quantitative description of the model. The Hamiltonian of the system can then be written as

$$\hat{H} = \hat{H}_F + \hat{V}, \tag{3.2.56}$$

with the free Hamiltonian

$$\hat{H}_F = \sum_i \left[E_g|g_i\rangle\langle g_i| + E_s|s_i\rangle\langle s_i| + E_e|e_i\rangle\langle e_i|\right] + \sum_{\vec{k}} \hbar\omega_k \hat{a}_k^\dagger \hat{a}_{\vec{k}}, \tag{3.2.57}$$

being the same of the writing process and the interaction potential being constituted of three parts.

$$\hat{V} = \hat{V}_1 + \hat{V}_2 + \hat{V}_3, \tag{3.2.58}$$

$$\text{excitation by the read beam} \Rightarrow \hat{V}_1 = -\sum_i \hbar\Omega_R e^{i(\vec{k}_R, \vec{r}_i - \omega_R t)}|e_i\rangle\langle s_i| + H.c., \tag{3.2.59}$$

$$\text{spontaneous emission } e \to g \Rightarrow \hat{V}_2 = -\sum_i \sum_{\vec{k}} \hbar g_{eg,\vec{k}} e^{i\vec{k}\cdot\vec{r}_i}|e_i\rangle\langle g_i|\hat{a}_{\vec{k}} + H.c., \tag{3.2.60}$$

$$\text{spontaneous emission } e \to s \Rightarrow \hat{V}_3 = -\sum_i \sum_{\vec{k}} \hbar g_{es,\vec{k}} e^{i\vec{k}\cdot\vec{r}_i}|e_i\rangle\langle s_i|\hat{a}_{\vec{k}} + H.c., \tag{3.2.61}$$

with $\Omega_R = \mu_{se}\mathcal{E}_R/\hbar$, $g_{eg,\vec{k}} = \mu_{ge}(\omega_{\vec{k}}/2\hbar\epsilon_0 v)^{1/2}$, and $g_{es,\vec{k}} = \mu_{se}(\omega_{\vec{k}}/2\hbar\epsilon_0 V)^{1/2}$. In the

interaction picture, we have

$$\begin{aligned}\hat{V}_I(t) =& e^{i\hat{H}_L t/\hbar}\hat{V}e^{-i\hat{H}_L t/\hbar} \\ =& -\sum_i \Bigg\{ \left[\hbar\Omega_R e^{i\vec{k}_R\cdot\vec{r}_i} e^{i(\omega_{es}-\omega_R)t}|e_i\rangle\langle s_i| + H.c.\right] \\ &+ \left[\sum_{\vec{k}} \hbar g_{eg,\vec{k}} e^{i\vec{k}\cdot\vec{r}_i} e^{i(\omega_{eg}-\omega_{\vec{k}})t}|e_i\rangle\langle g_i|\hat{a}_{\vec{k}} + H.c.\right] \\ &+ \left[\sum_{\vec{k}} \hbar g_{es,\vec{k}} e^{i\vec{k}\cdot\vec{r}_i} e^{i(\omega_{es}-\omega_{\vec{k}})t}|e_i\rangle\langle s_i|\hat{a}_{\vec{k}} + H.c.\right]\Bigg\}. \end{aligned} \tag{3.2.62}$$

The initial state of the system is obtained from Eq. 3.2.55:

$$|\psi(0)\rangle = |1_a\rangle|0\rangle = \frac{1}{\sqrt{N_a}}\sum_{i=1}^{Na} c_i e^{i(\vec{k}_W - k,\hat{z})\cdot\vec{r}_i}|s_i, 0\rangle. \tag{3.2.63}$$

Since there is initially only one excitation in level $|s\rangle$, the temporal evolution remains essentially restricted to the space of a single excitation. In the interaction picture, we can write

$$|\psi(t)\rangle_I = \sum_i e^{i(\vec{k}_W - k,\hat{z})\cdot\vec{r}_i}\left[A_i(t)|s_i,0\rangle + B_i(t)|e_i,0\rangle\right] + \int d^3\vec{k} C_{\vec{k}}(t)|g,1_{\vec{k}}\rangle + \sum_i \int d^3\vec{k} D_{i\vec{k}}(t)|s,1_{\vec{k}}\rangle, \tag{3.2.64}$$

with $A_i(t)$, $B_i(t)$, $C_{\vec{k}}(t)$ and $D_{i\vec{k}}(t)$ coefficients of slow variation to be determined from the Schrödinger equation. There are four possibilities of evolution, first term represents the case when the state $|s_i, 0\rangle$ remains unchanged, the second considers the atomic state in the excited level, so there isn't any photon involved in the process, third and fourth terms regard the emission of one spontaneous photon, in the case of third term we have that the atomic state has decayed from the excited level to the g level and the emission of one photon in the $e \to g$ transition. The fourth term considers that the atomic state has decayed from the excited level to the s level and a photon with frequency associated to the transition $e \to s$ is emited. We have also isolated the write spatial phase of the coefficients A_i and B_i. So we have

$$i\hbar\frac{\partial|\psi(t)\rangle_I}{\partial t} = \hat{V}_I|\psi(t)\rangle_I,$$

and

$$\begin{aligned} i\hbar\frac{\partial}{\partial t}\langle s_i,0|\psi(t)\rangle_I =& i\hbar\frac{\partial A_i}{\partial t} \\ =& -\hbar\Omega_R^* e^{-i\vec{k}_R\cdot\vec{r}_i} e^{-i(\omega_{es}-\omega_R)t}B_i(t); \end{aligned} \tag{3.2.65}$$

$$
\begin{aligned}
i\hbar\frac{\partial}{\partial t}\langle e_i,0|\psi(t)\rangle_I =& i\hbar\frac{\partial B_i}{\partial t}\\
=& -\hbar\Omega_R e^{i\vec{k}_R\cdot\vec{r}_i}e^{i(\omega_{es}-\omega_R)t}A_i(t)\\
&-\sum_{\vec{k}}\hbar g_{eg,\vec{k}}e^{i(\vec{k}_W+k_1\hat{z}+\vec{k})\cdot\vec{r}_i}e^{i(\omega_{eg}-\omega_{\vec{k}})t}C_{\vec{k}}(t)\\
&-\sum_{\vec{k}}\hbar g_{eg,\vec{k}}e^{i(\vec{k}_W+k_1\hat{z}+\vec{k})\cdot\vec{r}_i}e^{i(\omega_{eg}-\omega_{\vec{k}})t}D_{i\vec{k}}(t);
\end{aligned}
\tag{3.2.66}
$$

$$
\begin{aligned}
i\hbar\frac{\partial}{\partial t}\langle g,1_{\vec{k}}|\psi(t)\rangle_I =& i\hbar\frac{\partial C_{\vec{k}}}{\partial t}\\
=& -\sum_i\hbar g^*_{eg,\vec{k}}e^{i(\vec{k}_W-k_1\hat{z}-\vec{k})\cdot\vec{r}_i}e^{-i(\omega_{eg}-\omega_{\vec{k}})t}B_i(t);
\end{aligned}
\tag{3.2.67}
$$

$$
\begin{aligned}
i\hbar\frac{\partial}{\partial t}\langle s_i,1_{\vec{k}}|\psi(t)\rangle_I =& i\hbar\frac{\partial D_{i,\vec{k}}}{\partial t}\\
=& -\hbar g^*_{es,\vec{k}}e^{i(\vec{k}_W-k_1\hat{z}-\vec{k})\cdot\vec{r}_i}e^{-i(\omega_{es}-\omega_{\vec{k}})t}B_i(t).
\end{aligned}
\tag{3.2.68}
$$

Grouping Eqs. 3.2.65, 3.2.66, 3.2.67 and 3.2.68, we have

$$
\frac{\partial A_i}{\partial t} = i\Omega^*_R e^{-i\vec{k}_R\cdot\vec{r}_i}B_i(t),
\tag{3.2.69}
$$

$$
\begin{aligned}
\frac{\partial B_i}{\partial t} =& i\Omega_R e^{i\vec{k}_R\cdot\vec{r}_i}A_i(t) + i\sum_{\vec{k}}e^{i(-\vec{k}_W+k_1\hat{z}+\vec{k}\cdot\vec{r}_i)}\Big[g_{eg,\vec{k}}e^{i(\omega_{eg}-\omega_{\vec{k}}t)}C_{\vec{k}}(t)\\
&+ g_{es,\vec{k}}e^{i(\omega_{es}-\omega_{\vec{k}})}D_{i\vec{k}}(t)\Big],
\end{aligned}
\tag{3.2.70}
$$

$$
\frac{\partial C_{\vec{k}}}{\partial t} = i\sum_i g^*_{eg,\vec{k}}e^{i(\vec{k}_W-k_1\hat{z}-\vec{k}\cdot\vec{r}_i)}e^{-i(\omega_{eg}-\omega_{\vec{k}})t}B_i(t),
\tag{3.2.71}
$$

$$
\frac{\partial D_{i\vec{k}}}{\partial t} = ig^*_{es,\vec{k}}e^{i(\vec{k}_W-k_1\hat{z}-\vec{k}\cdot\vec{r}_i)}e^{-i(\omega_{es}-\omega_{\vec{k}})t}B_i(t).
\tag{3.2.72}
$$

To solve this system of equations, we assume the following tentative form to $B_i(t)$ [145]:

$$
B_i(t) = \beta_i(t)b_i(t)e^{i\vec{k}_R\cdot\vec{r}_i},
\tag{3.2.73}
$$

such that

$$
\beta_i(t) = \frac{\partial b_i(t)}{\partial t} = i\Omega_R A_i(t),
\tag{3.2.74}
$$

$$\frac{\partial \beta_i(t)}{\partial t} \cdot b_i(t) = i \sum_{\vec{k}} e^{i(-\vec{k}_W + k_1\hat{z} + \vec{k} - \vec{k}_R)\cdot \vec{r}_i} \left[g_{eg,\vec{k}} e^{i(\omega_{eg} - \omega_{\vec{k}} t)} C_{\vec{k}}(t) + g_{es,\vec{k}} e^{i(\omega_{es} - \omega_{\vec{k}})} D_{i\vec{k}}(t) \right]. \tag{3.2.75}$$

The advantage of taking the solution 3.2.73 is that we now have two systems of equations with clearly distinct roles in the problem. The system 3.2.69 + 3.2.74 describes a dynamics of Rabi oscillations. The system 3.2.71 + 3.2.72 + 3.2.75 describes a spontaneous emission dynamics. Let's start by solving the second set of equations. In integral form, Eqs. 3.2.71 and 3.2.72 reads

$$C_{\vec{k}}(t) = i \int_0^t dt' \sum_j g^*_{eg,\vec{k}} e^{i(\vec{k}_W - k_1\hat{z} - \vec{k} + \vec{k}_R)\cdot \vec{r}_j} e^{-i(\omega_{eg} - \omega_{\vec{k}} t')} \beta_j(t') b_j(t'), \tag{3.2.76}$$

$$D_{i\vec{k}}(t) = i \int_0^t dt' g^*_{es,\vec{k}} e^{i(\vec{k}_W - k_1\hat{z} - \vec{k} + \vec{k}_R)\cdot \vec{r}_i} e^{-i(\omega_{es} - \omega_{\vec{k}} t')} \beta_i(t') b_i(t'), \tag{3.2.77}$$

where we already applied the initial conditions $C_{\vec{k}}(0) = D_{i,\vec{k}}(0) = 0$. Substituting Eqs. 3.2.76 and 3.2.77 in 3.2.75, we have

$$\begin{aligned} \frac{\partial \beta_i(t)}{\partial t} = &- \int_0^t dt' \sum_{\vec{k}} \left\{ |g_{es,\vec{k}}|^2 e^{i(\omega_{es} - \omega_{\vec{k}})(t-t')} \frac{b_i(t')}{b_i(t)} \beta_i(t') \right. \\ &\left. + \sum_j |g_{es,\vec{k}}|^2 e^{i(\vec{k}_W - k_1\hat{z} - \vec{k} + \vec{k}_R)\cdot(\vec{r}_j - \vec{r}_i) + i(\omega_{eg} - \omega_{\vec{k}})(t-t')} \frac{b_j(t')}{b_i(t)} \beta_j(t') \right\}. \end{aligned} \tag{3.2.78}$$

Now we turn the sum over $\vec{k}$ in an integral in spherical variables:

$$\sum_{\vec{k}} \to 2\frac{V}{(2\pi)^3} \int d^3\vec{k} \to 2\frac{V}{(2\pi)^3} \int_0^{2\pi} d\phi \int_0^{\pi} d\theta \sin\theta \int_0^{\infty} d\omega_{\vec{k}} \frac{\omega_{\vec{k}}^2}{c^3} \tag{3.2.79}$$

As in Weisskopf-Wigner's theory, we use

$$\int_0^{\infty} d\omega_{\vec{k}} \omega_{\vec{k}}^2 e^{i(\omega_0 - \omega_{\vec{k}})(t-t'))} \approx 2\pi\delta(t-t')\omega_0. \tag{3.2.80}$$

From the Eqs. 3.2.79 and 3.2.80, Eq. 3.2.78 can be rewritten as

$$\begin{aligned} \frac{\partial \beta_i(t)}{\partial t} = &- \frac{2V}{(2\pi)^2} \int_0^{2\pi} d\phi \int_0^{\pi} d\theta \sin\theta \left\{ \frac{\omega_{es}^2 |g_{es,\vec{k}}|^2}{2c^3} + \frac{\omega_{eg}^2 |g_{eg,\vec{k}}|^2}{2c^3} \right. \\ &\left. + \frac{\omega_{eg}^2 |g_{eg,\vec{k}}|^2}{2c^3} \sum_{j \neq i} e^{i(\vec{k}_W - k_1\hat{z} - \vec{k} + \vec{k}_R)\cdot(\vec{r}_j - \vec{r}_i)} \frac{b_i(t)\beta_j(t)}{b_i(t)\beta_i(t)} \right\} \beta_i(t). \end{aligned} \tag{3.2.81}$$

Recalling the discussion of the Weisskopf-Wigner's theory, we have

$$|g_{es,\vec{k}}|^2 = \frac{\mu_{se}^2 \omega_{es}}{2\hbar\epsilon_0 V}\cos^2\theta, \tag{3.2.82}$$

$$|g_{eg,\vec{k}}|^2 = \frac{\mu_{ge}^2 \omega_{eg}}{2\hbar\epsilon_0 V}\cos^2\theta. \tag{3.2.83}$$

Then defining the rates of spontaneous decay Γ_{eg} and Γ_{es}, of e to g and s, respectively:

$$\Gamma_{eg} = \frac{1}{4\pi\epsilon_0}\frac{4\omega_{eg}^3\mu_{ge}^2}{3\hbar c^3}, \tag{3.2.84}$$

$$\Gamma_{es} = \frac{1}{4\pi\epsilon_0}\frac{4\omega_{es}^3\mu_{se}^2}{3\hbar c^3}, \tag{3.2.85}$$

eq. 3.2.81 reads

$$\frac{\partial\beta_i(t)}{\partial t} = -\frac{1}{2}\left\{\Gamma_{eg} + \Gamma_{es} + \frac{2\omega_{eg}^3\mu_{ge}^2}{2(2\pi)^2\epsilon_0\hbar c^3}\sum_{i\neq i}\int_0^{2\pi} d\phi\int_0^{\pi} d\theta\sin\theta\cos^2\theta \right.$$
$$\left.\times e^{i(\vec{k}_W - k_1\hat{z} - \vec{k} + \vec{k}_R)\cdot(\vec{r}_j - \vec{r}_i)}\frac{b_i(t)\beta_j(t)}{b_i(t)\beta_i(t)}\right\}\beta_i(t).$$

$$\frac{\partial\beta_i(t)}{\partial t} = -\frac{\Gamma}{2}\left\{1 + \frac{3}{4\pi}\frac{\Gamma_{eg}}{\Gamma}\sum_{i\neq i}\int_0^{2\pi} d\phi\int_0^{\pi} d\theta\sin\theta\cos^2\theta e^{i(\vec{k}_W - k_1\hat{z} - \vec{k} + \vec{k}_R)\cdot(\vec{r}_j - \vec{r}_i)}\right.$$
$$\left.\times\frac{b_i(t)\beta_j(t)}{b_i(t)\beta_i(t)}\right\}\beta_i(t). \tag{3.2.86}$$

where we consider the total rate of spontaneous decay of the level as

$$\Gamma = \Gamma_{eg} + \Gamma_{es}. \tag{3.2.87}$$

3.2.5 *Uniform excitation approximation*

If the atoms are illuminated approximately uniformly both by the write beam and by the read beam, the atomic dynamics for the optical excitation $s \to e$ should not vary appreciably from one atom to another. Because of this, we can approximate $b_i(t) \approx b_j(t)$ and $\beta_i(t) \approx \beta_j(t)$. Then defining the superradiance parameter:

$$\chi_i = 1 + \frac{3}{4\pi}\frac{\Gamma_{eg}}{\Gamma}\sum_{i\neq i}\int_0^{2\pi} d\phi\int_0^{\pi} d\theta\sin\theta\cos^2\theta e^{i(\vec{k}_W - k_1\hat{z} - \vec{k} + \vec{k}_R)\cdot(\vec{r}_j - \vec{r}_i)}, \tag{3.2.88}$$

eq. 3.2.86 becomes

$$\frac{\partial\beta_i(t)}{\partial t} = -\frac{\chi_i\Gamma}{2}\beta_i(t), \tag{3.2.89}$$

$$\Rightarrow \beta_i(t) = e^{-\chi_i \Gamma t/2}, \tag{3.2.90}$$

considering $\beta_i(0) = 1$ and $\beta_i(\infty) = 0$.

If $\chi_i > 1$,we have an increase in the rate of spontaneous decay induced by the presence of other atoms, a phenomenon known as superradiance [147]. At the level of a single photon, as discussed above, the purely quantum nature of the effect becomes quite explicit. Note that this increase in the emission rate is not the result of stimulated emission since only one photon is emitted by the ensemble. It's an effect that depends on the coherent distribution of excitation by the atoms of the ensemble, that is, it depends on a strong constructive interference of the atoms induced by the entanglement of the system. Substituting eq. 3.2.90 in 3.2.69 and 3.2.74, we get

$$\begin{cases} \dfrac{\partial A_i}{\partial t} = i\Omega_R^* e^{-\chi_i \Gamma t/2} b_i(t), \\ \\ \dfrac{\partial b_i}{\partial t} = i\Omega_R e^{\chi_i \Gamma t/2} A_i(t). \end{cases} \tag{3.2.91}$$

Derivating 3.2.91:

$$\frac{\partial^2 b_i}{\partial t^2} = \frac{\chi_i \Gamma}{2}\frac{\partial b_i}{\partial t} + i\Omega_R e^{\chi_i \Gamma t/2}\left(i\Omega_R^* e^{-\chi_i \Gamma t/2} b_i\right)$$

$$\Rightarrow \frac{\partial^2 b_i}{\partial t^2} - \frac{\chi_i \Gamma}{2}\frac{\partial b_i}{\partial t} + |\Omega_R|^2 b_i = 0$$

with $b_i = Ae^{\lambda t}$, we have

$$\lambda^2 - \frac{\chi_i \Gamma}{2}\lambda + |\Omega_R|^2 = 0 \Rightarrow \lambda\pm = \frac{\dfrac{\chi_i \Gamma}{2} \pm \sqrt{\dfrac{\chi_i^2 \Gamma^2}{4} - 4|\Omega_R|^2}}{2}$$

and therefore

$$b_i(t) = A_+ e^{\lambda_+ t} + A_- e^{\lambda_- t}.$$

With the initial conditions

$$b_i(0) = 0,$$

$$\frac{\partial b_i(0)}{\partial t} = i\Omega_R A_i(0) + \frac{i\Omega_R c_i}{\sqrt{N_a}},$$

where $c_i/\sqrt{N_a}$ comes from the constant in Eq. 3.2.63, we get

$$b_i(t) = \frac{2i\Omega_R c_i e^{\lambda_i \Gamma/4}}{\sqrt{N_a}\sqrt{\dfrac{\chi_i^2 \Gamma^2}{4|\Omega_R|^2}}} \sin h\left(\sqrt{\frac{\chi_i^2 \Gamma^2}{4} - 4|\Omega_R|^2 t}\right), \tag{3.2.92}$$

and

$$B(t) = i\frac{c_i\Omega_R e^{-\lambda_i\Gamma/4}}{\sqrt{N_a}\sqrt{\frac{\chi_i^2\Gamma^2}{4|\Omega_R|^2}}}\sin h\left(\sqrt{\frac{\chi_i^2\Gamma^2}{4}-4|\Omega_R|^2}t\right). \tag{3.2.93}$$

Eq. 3.2.93 gives us the evolution of the probability amplitude of the excited state of the atoms of the system over time. We then see clearly the Rabi oscillation behavior superposed with the spontaneous emission. Unlike the semiclassic treatment, however, we now have a spontaneous superradiant emission with a single photon being emitted collectively by the ensemble of atoms.

3.2.6 *Wave function of the emitted photon in the reading process*

So far we have focused our analysis on the time evolution of the atomic state, we can now come back to the spatial mode and time dependence of the photons emitted in the reading process. In this case, we have two possibilities for the generation of a photon from the spontaneous emission of the level $|e\rangle$. It can be generated in the transition $e \to s$ or in $e \to g$. In case of transition $e \to s$, we necessarily have that the atom that was in s_i will return to s_i. When realizing the trace over the atomic degrees freedom, we have an expression of the type $\sum_i |D_{i,\vec{k}}(t)|^2$ for each component $\vec{k}$ of the field. The dependence of $D_{i,\vec{k}}$ on the spatial phase $e^{i(\vec{k}_W - k_1\hat{z} - \vec{k} + \vec{k}_R)\cdot\vec{r}_i}$ does not affect the photon emitted in that transition, which thus has no preferential direction of emission. After the photon emission in the transition $e \to s$, all the spatial coherence information of the state originally stored is lost, and this can no longer be efficiently extracted from the atomic ensemble into field 2. In the case of the transition $e \to g$, all atoms will end up in the same state $|g, 1_{\vec{k}}\rangle$.When tracing out over atomic degrees of freedom, we have then an expression such as $|\int d^3\vec{k} c_{\vec{k}}(t)|^2$, highly sensitive to the spatial phase $e^{i(\vec{k}_W - k_1\hat{z} - \vec{k} + \vec{k}_R)\cdot\vec{r}_i}$ of each atom. Note that both $c_{\vec{k}}$ and χ_i have sums over this spatial phase of the atoms, implying that the limit of superradiant behavior manifests in parallel in these two quantities. The constructive interference on the spatial phases in $c_{\vec{k}}$ leads to the directionality of the superradiant emission, while its manifestation on χ_i leads to the acceleration of the emission. When N_a begins to grow, the process $e \to g$ of spontaneous emission dominates, because χ_i is increased and the process $e \to g$ occurs before $e \to s$. In addition, the probability of $e \to g$ increases with $N_a^2(|\sum_i|^2)$, while the probability of $e \to s$ increases with $N_a(|\sum_i|^2)$. Let us, therefore, focus only on the calculation of the emission of a photon in $e \to g$. The decomposition into wave vectors of the state of the emitted photon is given by $\lim_{t\to\infty} C_{\vec{k}}(t)$, with $C_{\vec{k}}(t)$ given by Eq. 3.2.76. To find the temporal dependence of the emitted photon we must apply a Fourier transform over its frequency spectrum. Let's define the photonic mode ψ_2 in terms of $\vec{q}$, the wave vector component of photon 2 extracted in the XY plane. We

have thus

$$\psi_2\left(\vec{q},t\right) \propto \int d\omega_{\vec{k}} e^{-i\omega_{\vec{k}}t} \lim_{t'\to\infty} C_{\vec{k}}(t'). \tag{3.2.94}$$

In order to obtain an analytical expression for the photonic wave packet extracted from the memory, we consider another important approximation: χ_i will have the same value for all atoms in the ensemble, that is, $\chi_i \approx \chi$. Equation 3.2.93 then becomes

$$\beta_i(t) = c_i e^{i\vec{k}_R\cdot\vec{r}_i}\beta(t), \tag{3.2.95}$$

with

$$\beta(t) = i\frac{2\Omega_R e^{-\chi\Gamma t/4}}{\sqrt{N_a}\sqrt{\dfrac{\chi^2\Gamma^2}{4} - 4|\Omega_R|^2}} \sin h\left(\sqrt{\frac{\chi^2\Gamma^2}{4} - 4|\Omega_R|^2}t\right) \tag{3.2.96}$$

being the same for all atoms in the ensemble. Replacing eq. 3.2.76 in 3.2.94 and using Eqs. 3.2.92, 3.2.90 and 3.2.53, we get

$$\psi_2(\vec{q},t) \propto \sum_j g^*_{eg,\vec{k}} e^{i(\vec{k}_W - k_1\hat{z} - \overbrace{\vec{k}}^{-\vec{q}\cdot\vec{\rho}-k_z z_j} + \vec{k}_R)\cdot\vec{r}_j} e^{-i\omega_{eg}t} c_j B(t).$$

Assuming $\vec{k}_W = -\vec{k}_R$

$$\psi_2(\vec{q},t) \propto B(t)e^{-i\omega_{eg}t}\int d\vec{q}_1\phi_1(\vec{q}_1)\sum_j e^{-i(\vec{q}+\vec{q}_1)\cdot\vec{\rho}_j}e^{-i[k_{1z}+k_z]z_j}. \tag{3.2.97}$$

To introduce the distribution of atoms in the medium, we define the atomic density $\rho(\vec{r}) \propto e^{-z^2/(2L^2)}$, with L the length of the ensemble in the direction z. In the directions x and y, we assume a uniform density, since we consider the transverse mode in these directions as defined by c_i, with the distribution of atoms being much more extensive in these directions than the width of the Gaussian mode ϕ_1. From this density function the sum over j can be transformed into an integral:

$$\begin{aligned}
\psi_2(\vec{q},t) &\propto B(t)e^{-i\omega_{eg}t}\int d\vec{q}_1\phi_1(\vec{q}_1)\int d\vec{\rho}\int_{-\infty}^{\infty} dz e^{z^2/(2L^2)}e^{-i(\vec{q}+\vec{q}_1)\cdot\vec{\rho}}e^{-i(k_{1z}+k_z)z} \\
&\propto B(t)e^{-i\omega_{eg}t}\int d\vec{q}_1\phi_1(\vec{q}_1)\delta(\vec{q}+\vec{q}_1)e^{-L^2(k_{1z}+k_z)^2/2} \\
&\propto \phi_1(-\vec{q})e^{-L^2(k_{1z}+k_z)^2/2}B(t)e^{-i\omega_{eg}t}.
\end{aligned} \tag{3.2.98}$$

This expression then shows that the second photon is extracted in the conjugated mode to the field 1, with $k_z \approx -k_{1z}$ and the corresponding transverse mode ϕ_1. Note that we also see that its wave packet oscillates with a central frequency ω_{eg}. The probability $p_c(t)$

of detecting a photon around the instant t is then

$$p_c(t) = F|B(t)|^2, \tag{3.2.99}$$

with F being a proportionality constant including, among other factors, the detection efficiency and the temporal width of the detection window. Obviously, in Eq. 3.2.99 we assume a very small detection window, so we can assume $B(t)$ constant throughout its duration. Another important quantity is the integral of 3.2.99 over all times

$$P_c = \int_0^\infty p_c dt, \tag{3.2.100}$$

which provides the total probability of extracting the information stored in the medium, maping it in a photon in mode 2. To compare theory and experiment, the normalized conditional probability is particularly important:

$$\frac{p_c(t)}{P_c} = \frac{|B(t)|^2}{\int_0^\infty |B(t)|^2 dt}, \tag{3.2.101}$$

which is independent of F. So, finally, we get

$$\frac{p_c(t)}{P_c} = \alpha\, e^{-\chi\Gamma t/2} \sin^2\left(\frac{\Omega t}{2}\right) \Delta t\,, \tag{3.2.102}$$

with $\alpha = \chi\Gamma\Omega_0^2/\Omega^2$, $\Omega = \sqrt{\Omega_0^2 - \chi^2\Gamma^2/4}$, $\Gamma/2\pi = 6.065$ MHz the natural linewidth for level $|e\rangle$, Ω_0 the Rabi frequency for the transition $|s\rangle \rightarrow |e\rangle$, and χ the superradiant enhancement for the decay $|e\rangle \rightarrow |g\rangle$, in case of the Rb atoms considered in this thesis.

3.2.7 *Superradiant amplification*

Let's now look for an expression for the superradiant amplification factor χ. Let's start by Eq. 3.2.88:

$$\chi_i = 1 + \frac{3}{4\pi}\frac{\Gamma_{eg}}{\Gamma} \sum_{j\neq i} \int_0^{2\pi} d\varphi \int_0^{\pi} d\theta \sin\theta \cos^2\theta e^{i(\vec{k}_W - k_1\hat{z} - \vec{k} + \vec{k}_R)\cdot(\vec{r}_j - \vec{r}_i)} \tag{3.2.103}$$

Now we approximate $\Gamma_{eg}/\Gamma \approx 1/2$ and neglect the pattern of dipole radiation, considering it isotropic, which is equivalent of doing $\cos^2\theta \approx 1$ in the integral. With this we have

$$\chi_i = 1 + \frac{3}{8\pi} \int\int d\varphi d\theta \sin\theta \sum_{j\neq i} e^{i(\vec{k}_W - k_1\hat{z} - \vec{k} + \vec{k}_R)\cdot(\vec{r}_j - \vec{r}_i)}, \tag{3.2.104}$$

where we have already used $\vec{k}_W = -\vec{k}_R$ and $k_1 \approx k$. Let us note now that we can write

$$d\Omega = d\varphi d\theta \sin\theta = \frac{dq_x dq_y}{k^2}, \tag{3.2.105}$$

with $\vec{q}$ the component of $\vec{k}$ perpendicular to the Z axis. Using 3.2.105 and assuming the constraint $k^2 = q_x^2 + q_y^2 + k_z^2$, Eq. 3.2.104 becomes

$$\begin{aligned}\chi_i = 1+\frac{3}{8\pi k^2}\int_{-k}^{k} dq_x \int_{-\sqrt{k^2-q_x^2}}^{\sqrt{k^2-q_x^2}} \sum_{j\neq i} \Big[& e^{i\left(-k\hat{z}-q_x\hat{x}-q_y\hat{y}+\sqrt{k^2-q_x^2-q_y^2}\hat{z}\right)\cdot(\vec{r}_j-\vec{r}_i)} \\ & + e^{i\left(-k\hat{z}-q_x\hat{x}-q_y\hat{y}-\sqrt{k^2-q_x^2-q_y^2}\hat{z}\right)\cdot(\vec{r}_j-\vec{r}_i)}\Big]\end{aligned} \tag{3.2.106}$$

where we use that each pair of values (q_x, q_y) implies in two possible values for k_z : $\pm\sqrt{k^2-q_x^2-q_y^2}$. We now introduce the atomic density function

$$\rho(\vec{r}) = \frac{N}{(2\pi)^{3/2}W^2 L} e^{-\left(x^2+y^2\right)/\left(2W^2\right)} e^{-z^2/(2L^2)}, \tag{3.2.107}$$

Which describes an atomic ensemble with atoms distributed in Gaussian modes of width W in the X, Y directions (given by the width of the detection mode ϕ_1) and length L in the direction Z (given by the total length of the ensemble). From that atomic density, Eq. 3.2.106 can be written as

$$\begin{aligned}\chi_i = 1+\frac{3}{8\pi k^2}\int_{-k}^{k} dq_x \int_{-\sqrt{k^2-q_x^2}}^{\sqrt{k^2-q_x^2}} dq_y \int d^3\vec{r}\rho(\vec{r}) e^{-i[q_x(x-x_i)+q_y(y-y_i)]} \\ \times \left[e^{-i\left(k-\sqrt{k^2-q_x^2-q_y^2}\right)(z-z_i)} + e^{-i\left(k+\sqrt{k^2-q_x^2-q_y^2}\right)(z-z_i)}\right].\end{aligned} \tag{3.2.108}$$

using

$$\int \frac{ds e^{-s^2/(2\omega^2)} e^{-iqs}}{(2\pi)^{1/2}} = \omega e^{-\omega^2 q^2/2}, \tag{3.2.109}$$

we get therefore

$$\begin{aligned}\chi_i = 1+\frac{3N}{8\pi k^2}\int_{-k}^{k} dq_x \int_{-\sqrt{k^2-q_x^2}}^{\sqrt{k^2-q_x^2}} dq_y e^{-W^2(q_x^2+q_y^2)/2} e^{i(q_x x_i+q_y y_i)} \\ \times \Bigg[e^{-L^2\left(k-\sqrt{k^2-q_x^2-q_y^2}\right)^2/2} e^{i\left(k-\sqrt{k^2-q_x^2-q_y^2}\right)z_i} \\ + e^{-L^2\left(k+\sqrt{k^2-q_x^2-q_y^2}\right)^2/2} e^{i\left(k+\sqrt{k^2-q_x^2-q_y^2}\right)z_i}\Bigg].\end{aligned} \tag{3.2.110}$$

Typical values for the quantities k, W and L for atomic systems used in quantum memories are $k \approx 10^7 m^{-1}$, $W \approx 100\mu m = 10^{-4}m$ and $L \approx 1mm = 10^{-3}m$. From there we see that the function $e^{-W^2(q_x^2+q_y^2)/2}$ has a width $1/W \ll k$ in q_x and q_y, so that the integrals in

those quantities can be extended to $-\infty$ and $+\infty$. We can still approximate

$$k - \sqrt{k^2 - q_x^2 - q_y^2} \approx \frac{q_x^2 + q_y^2}{2k},$$

$$k + \sqrt{k^2 - q_x^2 - q_y^2} \approx 2k,$$

and rewritre 3.2.110 as

$$\chi_i = 1 + \frac{3N}{8\pi k^2} \int_{-\infty}^{\infty} dq_x \int_{-\infty}^{\infty} dq_y e^{-W^2(q_x^2+q_y^2)/2} e^{i(q_x x_i + q_y y_i)} \times \left[e^{-L^2(q_x^2+q_y^2)^2/(8k^2)} e^{i(q_x^2+q_y^2)z_i/2k} + \underbrace{e^{-2L^2k^2}}_{0} e^{2ikz_i} \right]. \tag{3.2.111}$$

In addition to the fact that the second term in the second line of Eq. 3.2.111 is zero, note that $1/W^2 \ll \sqrt{2}k/L$, so that the width of the function $e^{-W^2(q_x^2+q_y^2)/2}$ is much smaller than the width of the first term in the second line of 3.2.111. With this, we can approximate

$$e^{-L^2(q_x^2+q_y^2)/(8k^2)} e^{i(q_x^2+q_y^2)z_i/2k} \approx 1$$

in the integral. Equation 3.2.111 then reads

$$\chi_i \approx 1 + \frac{3N}{8\pi k^2} \underbrace{\int_{-\infty}^{\infty} dq_x \int_{-\infty}^{\infty} dq_y e^{-W^2(q_x^2+q_y^2)/2} e^{i(q_x x_i + q_y y_i)}}_{2\pi/W^2 e^{-(x_i^2+y_i^2)/2W^2}}$$

$$\Rightarrow \chi_i = 1 + \frac{3N}{4W^2k^2} e^{-(x_i^2+y_i^2)/2W^2} \tag{3.2.112}$$

Finally, defining [145]:

$$\chi = \langle \chi_i \rangle = 1 + \frac{3N}{4W^2k^2} \underbrace{\left[\frac{1}{N} \cdot \int d^3\vec{r} \rho(\vec{r}) e^{-(x^2+y^2)/2w^2} \right]}_{1/2}$$

$$\Rightarrow \chi \approx 1 + \frac{N}{2W^2k^2}. \tag{3.2.113}$$

An important point to note in this expression is the independence of χ on L, typical of a superradiant emission from a cigar-shaped ensemble. Optical depth (OD) is defined as the natural logarithm of the ratio of incident to transmitted radiant power through a material. From an experimental point of view, as we have $N \propto OD$. In this way, optical depth parameterize the modification of χ in the sample.

3.2.8 *Next step*

As discussed above, there is already a fairly well-established technology for the study of quantum memories of a single photon. In addition there are some works involving fundamental studies on the quantum nature of superradiance in the reading process, at least for the regime of a single excitation [146, 148–150].

However, if we look again at the need for quantum repeaters in the context of implementing a real quantum network, we see that there are a number of other challenges to overcome. There are reviews [151–155] devoted to explaining which the main ideal characteristics are to have different quantum memories to execute all type of tasks in an ambitious picture of a general quantum communication. Characteristics such as efficiency, fidelity, bandwidth, storage time and number of excitations are the most frequent in the debate. Depending on the platform used, that is, type of atomic medium and trapping mechanism, etc., different quantum memory models have proven to be better or worse in different aspects. It is always interesting that one platform presents the greatest versatility in terms of these characteristics. Until now the DLCZ scheme has always been exploited in the single photon regime. However, in principle this is not an inherent limitation. In fact, other numbers of excitations [156] are deliberately excluded, either by simplicity, to model the phenomena, or by the low probability that would lead to large measurement times. In the following chapters, we are interested in studying the phenomenon of superradiance in the 2-photon regime, under conditions practically identical to those that have already been applied to a single excitation in various articles [146, 148–150, 157, 158]. We thus demonstrate that the DLCZ scheme is a more versatile alternative than what has been done so far, at least in its multiple-excitation storage feature.

4 Experimental apparatus

The mechanisms of neutral atom trapping use the interaction of an atom with a laser beam, with a static magnetic field, or a combination of both [159]. A single laser beam can be used to trap atoms through the dipolar force, proportional to the intensity gradient of the beam. On the other hand, a single static magnetic field can also be used to trap atoms through the interaction between the field and the magnetic dipole moment of the atom [160]. However, optical traps as well as magnetic traps suffer some limitations. They are extremely inefficient without some other prior cooling mechanism to help load colder atoms into the trap.

This problem is usually solved thanks to the magneto-optical trap (MOT) (see examples in [161–163]). This is a very efficient technique to produce a dense ensemble of cold atoms that can be used in a variety of atomic physics experiments [164,165]. The magneto-optical trap consists of six circularly polarized laser beams, as in a three-dimensional array of optical molasses, in combination with a magnetic field, and was originally demonstrated by Raab et al. [166].

In the MOT region, an atom experiences a force typical of a damped harmonic oscillator, due to the optical molasses forces created by the intersection of the cooling laser beams. It occurs by detuning the laser beam to a frequency smaller than the resonant frequency (also known as red detuning), since laser light is only absorbed if the light is frequency up-shifted by the Doppler effect, which occurs whenever the atom is moving towards the laser source. Then, for total confinement we need lasers in any set of three orthogonal directions. As an atom at room temperature has many thousands times the momentum of a single photon, the cooling of an atom must involve many cycles of absorption and spontaneous emission, with the atom losing up to $\hbar k$ of momentum in each cycle. Because of this, if an atom is to be laser cooled, it must have a specific energy level structure known as a closed optical loop, where after an excitation-spontaneous emission event, the atom always returns to its original state. Sometimes either the atom doesn't contain closed optical loops or we are interested in certain levels of its energy structure that makes the atom to decay to a "dark" state, which would stop the cooling process. However, this atom can also be laser-cooled by using a second laser beam that re-excites

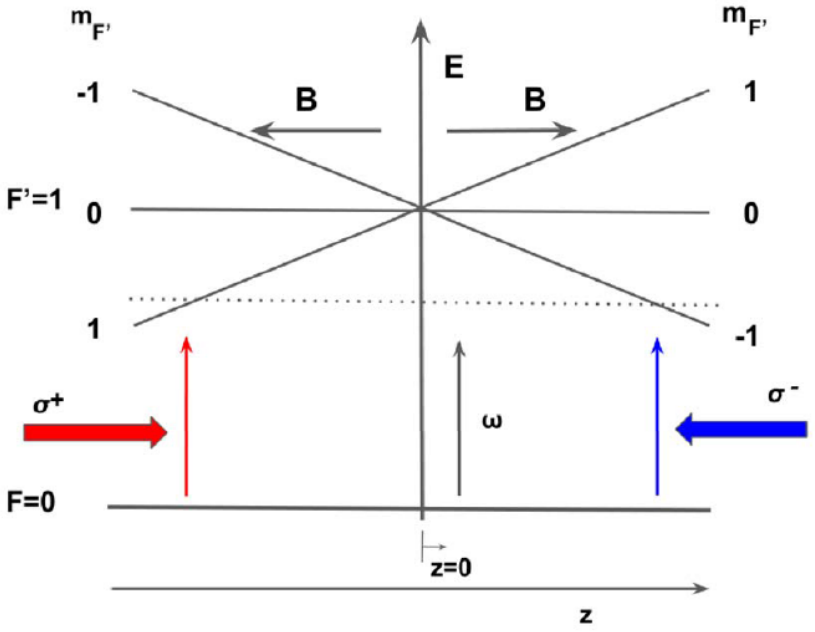

Figure 13: A conceptual scheme for a general one-dimensional MOT with two counterpropagating beams with frequency ω and circular polarizations σ^+ and σ^- are shown. The separation between the Zeeman sub-levels m_F of the hyperfine energy level $F' = 1$ increases proportional to the magnetic field B, this field increases linearly from $z = 0$ in the positive and negative Z-axis directions.

the population back to the optical loop after it has decayed to an out-of-cycle state. This is called a repumping laser.

On the other hand, the magnetic field varies linearly causing a Zeeman shift in the magnetic-sensitive levels. This magnetic field increases with the radial distance from the center of the trap, so that as an atom moves away from the center of the trap, the atomic resonance moves closer to the frequency of the trapping light, beacuse of the doppler effect, and the atom becomes more susceptible to interact with a photon in the direction towards the center of the trap, as depicted in Fig. 13. In this way, the magnetic field together with the optical molasses provides the restoring force to confine the atoms at the zero point of the magnetic field. The MOT is highly robust and insensitive to power imbalances between different laser beams.

In short, we know that a MOT must have, in general, 3 basic components already mentioned above, i.e. atoms, cooling lasers and a magnetic field. A fourth condition is the vacuum, since the trapping potential is small in comparison to the thermal energies of atoms at room temperature and most collisions between trapped atoms and the background gas supply enough energy to the trapped atom to kick it out of the trap. Finally, in some cases, like the one in this thesis, it will be necessary to incorporate a fifth component, the repumping laser to return the population of atoms to the optical cycle.

The experimental setup used in this thesis follows the standard of several experiments performed for fundamental studies in the DLCZ scheme in the literature [113, 125–131, 144, 146, 167–172]. In particular, some modifications have been made with respect to

the traditional one in the stage in which the superradiance of two photons emitted in the reading process is studied. The core of the experiment is a magneto-optical trap of neutral atoms of ^{87}Rb. In this chapter we are going to explain all the components that allow the creation of a confined cloud of atoms, which we call "sample". In the next section we focus on the writing and reading processes, which basically correspond to the laser system with which the sample is illuminated in the experiment, giving rise to the interaction between light and atoms. In this section we will also detail not only the spatial distribution of the write and read pulses, but also delving into their temporal configuration. From the write and read pulses, fields 1 and 2 are generated, respectively, which lead to the need to explain the detection scheme, i.e. the photo-counting of these 2 fields. We emphasize the modifications made to the scheme, when we go from the regime of a single-photon to the one of two photons stored. In the latter, higher order correlations are required, and therefore a higher number of detectors. To increase the number of detectors in the reading process, a time-multiplexed detector (TMD) system is set up, in which 2 APD's can be exploited as 4, in the time domain.

4.1 Creation of the atomic ensemble

In this section we are going to explain the processes involved in the formation of a cloud of atoms by a MOT. First we detail the energy structure of any general Hydrogen-like atom, and particularly our Rb atom, and how the polarization scheme is related to it. After that we describe the principal parts of the setup related to the creation of the ensemble of atoms, and how they are combined to operate as a MOT.

4.1.1 *Structure of energy levels*

Let's start with a simplified model of a hydrogen-like atom where we will only take into account the structure due to the main quantum number n and orbital angular momentum ℓ.

Here the notation we use is $n\ell$, where n is related to the potential energy of the electron with respect to the nucleus, and ℓ is the azimuthal quantum number that relates to the shape of the electronic orbitals and we find that for a level n there are n possible values of ℓ, counting from 0 to $n-1$. In spectroscopic notation for $\ell = 0$ we use s, for $\ell = 1$ we denote p, d for $\ell = 2$, f in case of $\ell = 3$ and for the rest we continue alphabetically from g onwards (see Fig. 14).

This simplified model can take many corrections, but here we focus on 3 main corrections, adding the spin of the electron, the spin of the nucleus, and an external magnetic field.

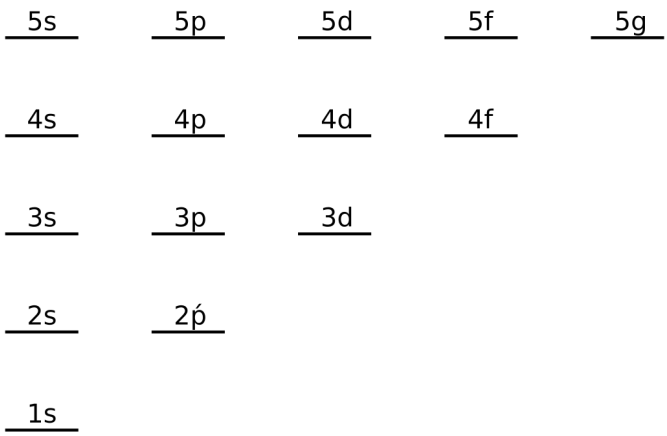

Figure 14: Levels from principal quantum number

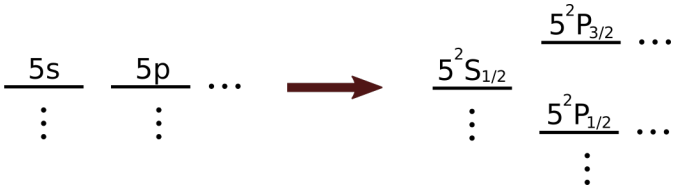

Figure 15: Fine structure of ^{87}Rb, example of levels 5s and 5p. When introducing the spin of the electron only 5p is going to split in two fine levels.

Introducing the electron spin

The orbital motion of the electron around the nucleus results in an effective magnetic field acting over the electron. Since the electron has an intrinsic magnetic moment, the energy levels that we were considering in the section above will be altered depending on whether the electron is aligned with this effective magnetic field or if it is in the opposite direction. In the latter case the energy should be higher.

This consideration gives rise to the so-called fine structure, where the levels with $\ell \neq 0$ are affected because they have a magnetic nature. Its name comes from the fact that the involved energy differences are very small.

The notation here is the "modified spectroscopic notation" or "Russel-Saunders notation", which labels energy states as $^{2S+1}L_J$ with, in our case $S = 1/2$ being the spin of the single optical electron. In this way, the superscript will be 2 in our entire structure. L represents the orbital angular momentum in spectroscopic notation with the difference that now it is in capital letters, and finally J corresponds to the total electronic angular momentum that can vary from $|L - S|$ to $|L + S|$, which will be our new degree of freedom.

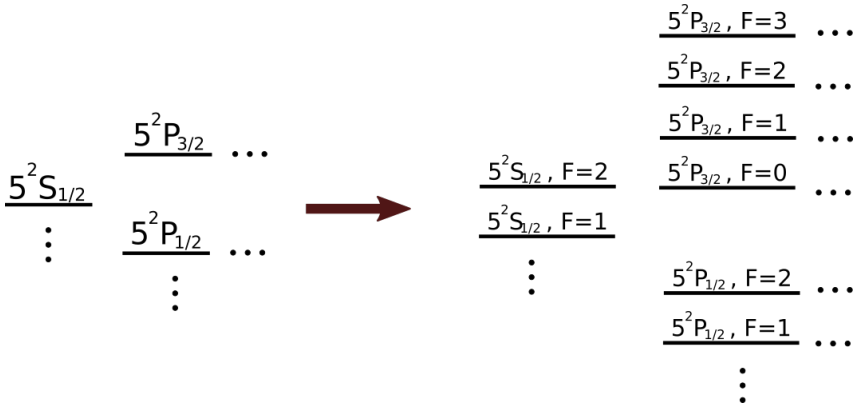

Figure 16: Hyperfine structure of levels 5s and 5p. We see that 5s turns into two hyperfine levels and 5p into 6 hyperfine levels.

Introducing the nuclear spin

Now we move on to a new level unfolding scale, which involves the addition of the nuclear spin, forming a new quantity we call "total magnetic momentum" $F = I + J$, which maintains a close analogy to the fine structure. Now our degree of freedom varies from $F = |I - J|$ to $F = |I + J|$. It is called hyperfine structure and its name is due to the fact that the levels are even closer than in the case of the fine structure.

It is interesting to observe a specific case to have a better intuition of what happens. We take ^{87}Rb, where $I = 3/2$, and in Fig. 16 we see that for $5s$ the fine structure $5^2S_{1/2}$ does not present unfolding as opposed to its hyperfine structure that has 2 levels $F = 3/2 - 1/2 = 1$ and $F = 3/2 + 1/2 = 2$. In the case of $5p$, we see 6 hyperfine levels, the 2 first levels come from the fine level $5^2P_{1/2}$, where we have $J = 1/2$, with a hyperfine spectrum of $F = 3/2-1/2 = 1$ and $F = 3/2+1/2 = 2$. On the other hand we have $5^2P_{3/2}$ with $J = 3/2$, which leads to $F = 3/2 - 3/2 = 0$, $F = 3/2 - 1/2 = 1$, $F = 3/2 + 1/2 = 2$ and $F = 3/2 + 3/2 = 3$, as shown in figure 16.

Introducing an external magnetic field

Our last consideration to the energy structure of hydrogen-like atoms involves the application of an external magnetic field. Under the action of this external field, the atom will suffer what is known as the "Zeeman effect", which is an effect analogous to that of fine and hyperfine structures, but has an external origin. In this case, the energy dislocation for the different Zeeman levels, E_z, is

$$E_z = g_F \mu_0 B M,$$

where the magnitude of the applied magnetic field is B, μ_0 is the Bohr magneton and g_F is the Landé g factor. M is known as the projection number, which is the degree of freedom in this structure. It is important to mention that g_F is different in each hyperfine

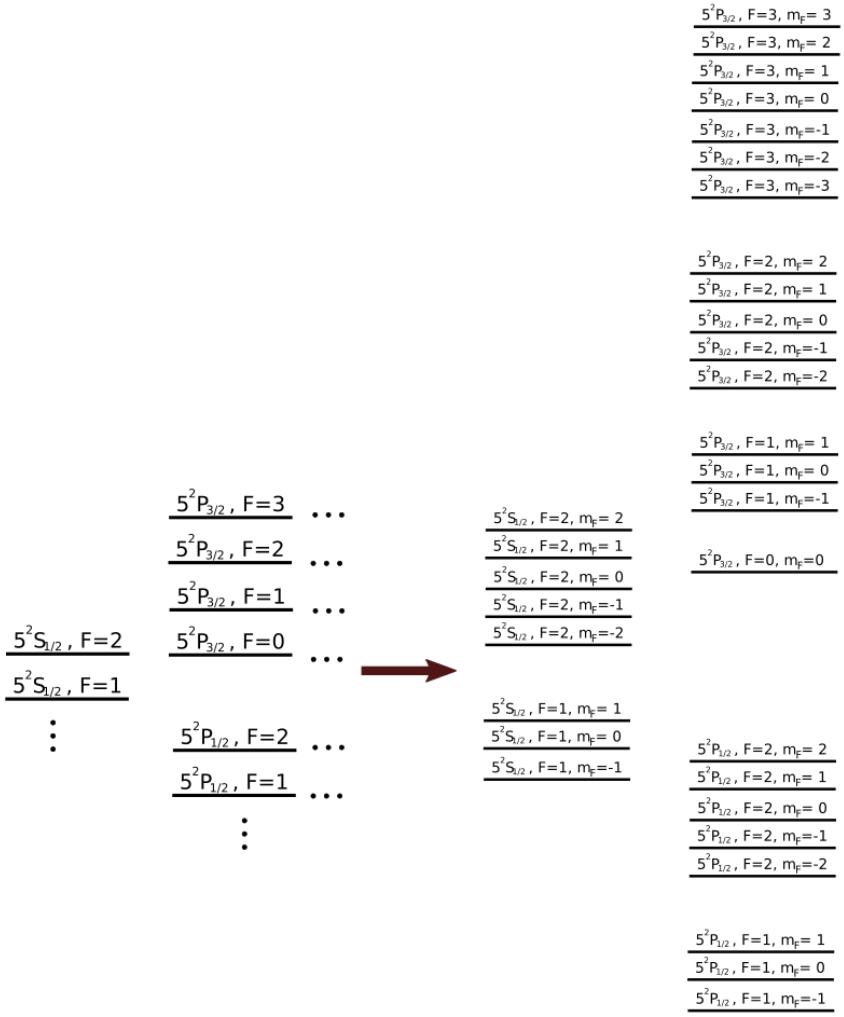

Figure 17: Zeeman structure for Rb, levels $5^2S_{1/2}$, $5^2P_{1/2}$ and $5^2P_{3/2}$. It presents 8 Zeeman levels for $5^2S_{1/2}$, 8 for $5^2P_{1/2}$ and 16 for $5^2P_{3/2}$.

level

$$g_F = g_J \frac{F\left(F+1\right) + J\left(J+1\right) - I\left(I+1\right)}{2F\left(F+1\right)}$$

where

$$g_J = 1 + \frac{J\left(J+1\right) + S\left(S+1\right) - L\left(L+1\right)}{2J\left(J+1\right)}$$

Here, for a hyperfine level F, these are $2F+1$ possible Zeeman levels, ranging from $M = -F$ to $M = F$, always passing through zero, so that in the example mentioned above, there will be 5 Zeeman levels for $F = 2$ and 3 Zeeman levels for $F = 1$. See Fig.

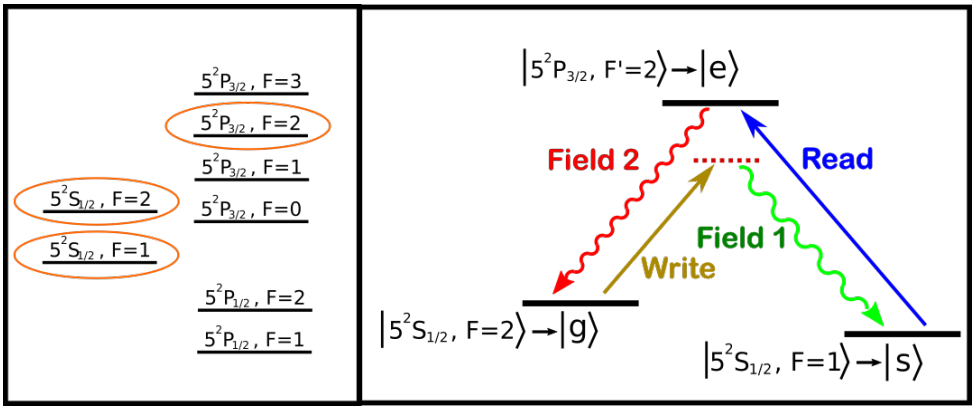

Figure 18: Hyperfine picture of λ configuration. In left panel, selected hyperfine levels to be used in configuration.

	$m_F = -1$	$m_F = 0$	$m_F = 1$
σ^+	$\sqrt{1/24}$	$\sqrt{1/8}$	$\sqrt{1/4}$
π	$-\sqrt{1/8}$	$-\sqrt{1/6}$	$-\sqrt{1/8}$
σ^-	$\sqrt{1/4}$	$\sqrt{1/8}$	$\sqrt{1/24}$

Table 1: Dipole matrix elements for transition $F = 1 \rightarrow F' = 2$

17 for complete Zeeman structure of levels $5^2S_{1/2}$, $5^2P_{1/2}$ and $5^2P_{3/2}$.

Zeeman structure for the experiment

The Λ configuration of atoms of our experiment has two fundamental levels g and s and one excited e, which are those shown in figure 18. As explained above, this description corresponds to the hyperfine structure which still comprises some level degeneracy. As seen in the previous examples, in fact, this Λ configuration is actually a family of Λ configurations when the Zeeman structure is taken into account.

We must also regard the polarization of the lasers, since it determines the possible transmitions between Zeeman sub-levels. The elements of the dipole matrix [173] for the transition $F = 1 \rightarrow F' = 2$ are given in table 1 and for the transition $F = 2 \rightarrow F' = 2$ are given in table 2. We see that for right-handed circularly polarized light, σ^+, there is a case $F = 2, m_F = 2 \rightarrow F' = 2$ that no value appears on the table. This occurs because there is no level to connect with $F = 2, m_F = 2$ in which $m'_F = m_F + 1$, which is required for a σ^+ transition, since we are at the highest Zeeman level of the fundamental state. Similarly, for the fact that we have no value for the σ^- transition $F = 2, m_F = -2 \rightarrow F' = 2$. To calculate these matrix elements, it is useful to factor out the angular dependence and write the matrix element as a product of a Clebsch-Gordan coefficient and a reduced matrix element, using the Wigner-Eckart theorem [173].

	$m_F = -2$	$m_F = -1$	$m_F = 0$	$m_F = 1$	$m_F = 2$
σ^+	$\sqrt{1/12}$	$\sqrt{1/8}$	$\sqrt{1/8}$	$\sqrt{1/12}$	
π	$-\sqrt{1/6}$	$-\sqrt{1/24}$	0	$\sqrt{1/24}$	$\sqrt{1/6}$
σ^-		$-\sqrt{1/12}$	$-\sqrt{1/8}$	$-\sqrt{1/8}$	$-\sqrt{1/12}$

Table 2: Dipole matrix elements for transition $F = 2 \rightarrow F' = 2$

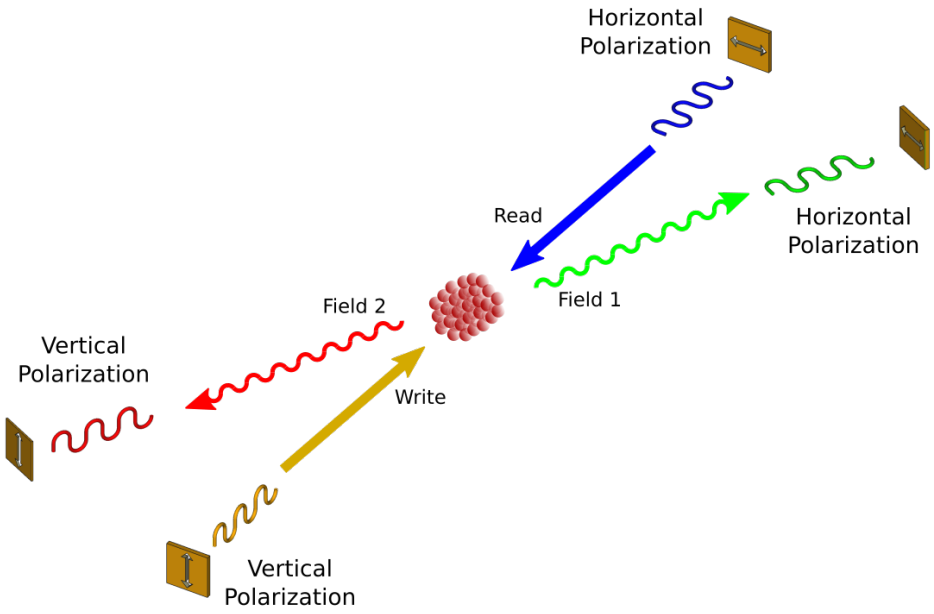

Figure 19: DLCZ scheme with linear polarizations. Write and Field 2 have vertical polarization, Read and Field 1 have horizontal polarizations. Field 1 and Field 2 have orthogonal polarizatons and are conjugated modes of a four-wave mixing process.

Linear Polarization

Consider the case where the write, read, field 1 and field 2 polarizations are all linear as shown in Fig. 19.

Here the write beam has vertical polarization and read laser has horizontal polarization, while field 1 and field 2 are detected, by means polarizers, in polarizations orthogonal to them, respectively. The diagram of levels of the Λ configuration will be unfolded in Fig. 20. Note that if a vertical polarization induces π transitions, then the horizontal polarization induces σ^+ and σ^- transitions.

We see that the elements of the dipole matrix are different for the read frequency on the different FWM processes. Thus, in the wave packets, we may have different Rabi frequencies and a beating between them. As this situation is not ideal we consider now a scheme using circular polarizations.

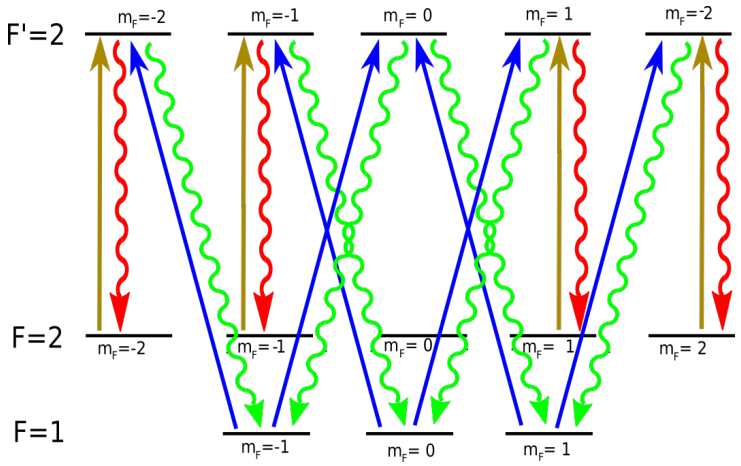

Figure 20: Λ configuration considering the Zeeman structure for linear polarizations.

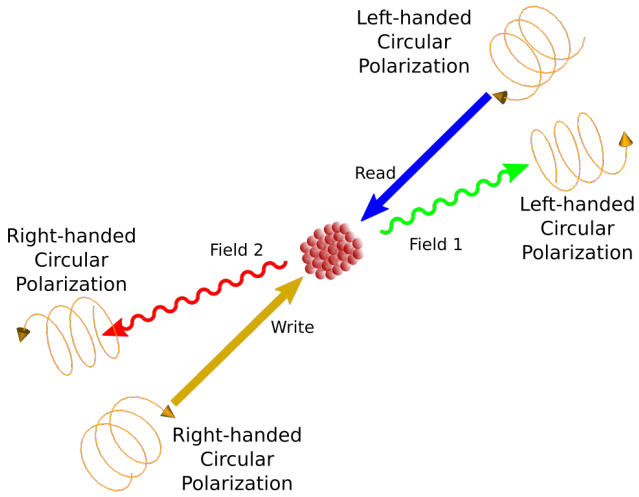

Figure 21: DLCZ scheme with circular polarizations. Write and Field 2 have Right-handed cricular polarization, Read and Field 1 have Left-handed cricular polarization. Field 1 and Field 2 have orthogonal polarizatons.

Circular polarization

In the experimental setup shown in Fig. 25, with which the final superradiance measurements were made, we have the polarization scheme presented in Fig. 21. In this case we see that the write and field-2 transitions employ right-handed circularly polarized light (σ^+), which largely limits the transition possibilities we had before. On the other hand the read beam and field 1 employ left-handed circularly polarized light (σ^-). It is important to note that the polarizations of both field 1 and field 2 are defined by construction, through polarizers placed in the detection channel. Considering all the above, the Λ scheme of levels turns into that shown in Fig. 22.

As we know that Rabi frequency is proportional to the dipole matrix element in each transition, we see that the 2 FWM processes that we have in Fig. 22, generate 2 different Rabi frequencies in the read process, with a possible beat between them. It is then necessary to use some method to simplify the model: this is the optical pump presented

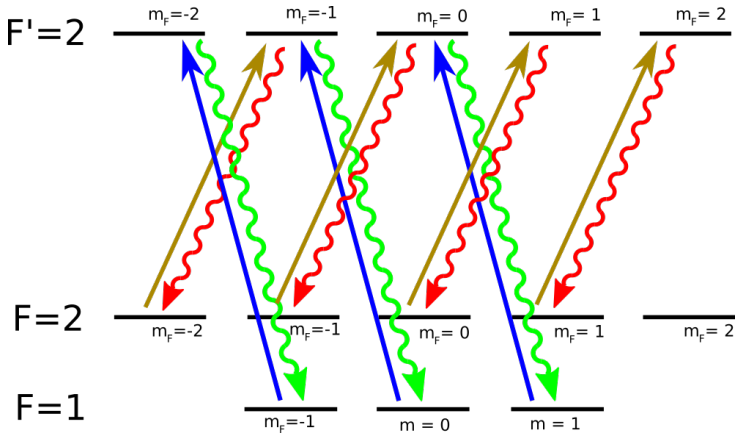

Figure 22: Λ configuration considering Zeeman structure for all possible circular polarizations, not only the 2 FWM processes we are interested in.

in section 5.3.

4.1.2 *Atom source*

As a source of atoms we use a rubidium dispenser (Alvatec AS-Rb-60-S) consisting of a small stainless steel tube filled with 60 mg of rubidium metal. The tube is crimped closed at one end, and the other end is sealed by an indium plug since alkali metals are highly reactive. Flattened tags are provided at each end for mounting and electrical connection. With the indium seal intact, the dispensers can be easily handled under ambient conditions. Once mounted in the cell and under vacuum, the dispenser is heated by passing an electrical current through the steel tube. During a preliminary activation step, the dispenser is heated until the indium seal melts. After activation, passing a larger current through the dispenser causes the rubidium to evaporate and a broad, weakly collimated atomic jet is emitted from the unsealed end.

4.1.3 *Lasers: Doppler cooling and repumping*

In order to generate the cooling and the repumping beams we used two diode lasers, so-called TICO and TECO, respectively. The diode lasers used in the experiment are THORLABS DL7140-201S and emit at a wavelength around 785 nm. The power of the TICO laser after the optical isolator is 40 mW when we supply it with a current of approximately 100 mA, and the TECO laser, approximately 59 mW for a current of 114 mA. For the frequency stabilization of the lasers a servo lock-in circuit is used, which takes the signal obtained in the saturated absorption experiment as a frequency reference.

The complete saturated absorption spectrum for line D_2 of ^{87}Rb and ^{85}Rb is shown in figure 23, where we can observe the 4 Doppler absorption wells. The TICO (cooling) laser is locked in the cross-over $F_c = 1 - 3$ (between the transitions $F = 2 \rightarrow F' = 1$ and $F = 2 \rightarrow F' = 3$), represented by the third peak of the fourth well, with decreasing

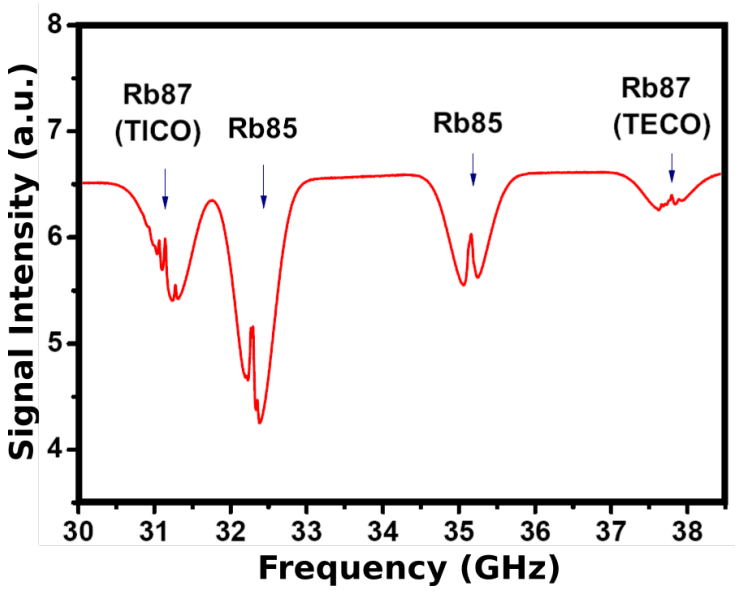

Figure 23: Rubidium spectrum obtained via saturated absorption measurement in a vapor cell of rubidium atoms at room temperature. It is empoyed as frequency reference of lasers TICO and TECO, which generate all beams of the experiment.

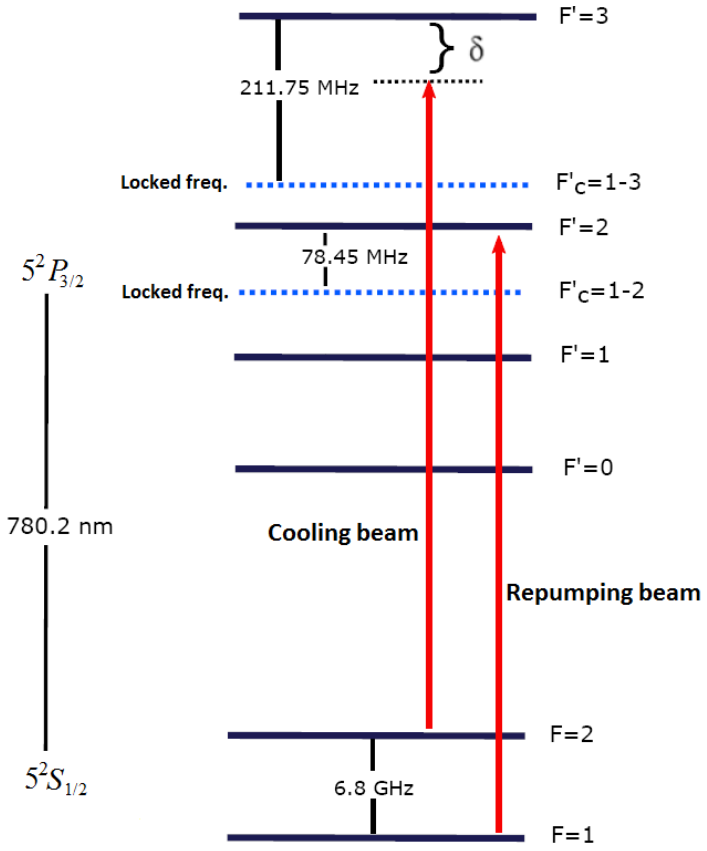

Figure 24: Rubidium scheme of energy levels showing transitions used for cooling and repumping lasers. In the case of the cooling and trapping system we employ lasers red detuned from the $F = 2 \rightarrow F' = 3$ transition. The repump laser is resonant with the $F = 1 \rightarrow F' = 2$ transition.

frequency. The TECO (repumping) laser was locked in the second peak of the first well, which corresponds to the cross-over $F_c = 1 - 2$ (between the transitions $F = 1 \rightarrow F' = 1$ and $F = 1 \rightarrow F' = 2$). These two beams are then tuned to the desired frequencies, using Acoustic-Optical Modulators (AOM). We tune the cooling beams near the resonance with the $F = 2 \rightarrow F' = 3$ transition, through an AOM with a central frequency at 200 MHz which detunes the locked frequency in about 211.75 MHz. As shown in Fig. 24, this detuning can be modified in order to produce the negative δ needed for the optical molasses. The atoms excited to the level $F' = 3$, can only decay to the ground state $F = 2$, which corresponds to a cyclic transition. However, there is a small probability for the atoms to be excited to the $F' = 2$ level. Thus, they can decay to the fundamental level F =1, accumulating atoms at this level, which would interrupt the cooling cycle. This creates the need for using a repumping beam, for which we use a AOM with a central frequency of 110 MHz in order to achieve a 78.45 MHz detuning from the frequency at which it was locked, leaving it resonant with the $F = 1 \rightarrow F' = 2$ transition.

4.1.4 *Magnetic trapping*

There is a pair of coils in order to generate a magnetic field gradient in anti-Helmholtz configuration, in which the currents are running through the two coils in opposite directions. Thus, we will have a magnetic field equal to zero in the center and increasing approximately linearly in all directions in its closest neighborhood. Their diameter is 10.5 cm, being composed of 207 turns of copper wire. The current is around 4 A passing through the coils, so we estimate a gradient of 10 G/cm in the MOT region.

Due to spurious magnetic fields from different sources, such as the earth magnetic field, other magnetic elements within the experimental setup, or imperfections in the creation of the magnetic field gradient, etc. we require, then, the use of a compensation-field system capable of generating a constant field in any direction by the superposition of three fully controllable orthogonal components. In order to find exactly the best compensation magnetic field vector, a microwave spectroscopy experiment is performed exploiting the Zeeman spectral splitting [174]. The compensation coils are three pairs of square coils in Helmholtz configuration, each composed of 52 turns of 1 mm diameter copper wire. Its size is 22.5 cm at each side. When a current of 1A passes through one pair of coils, a magnetic field of 1 G is generated in the middle point. Each coil has an independent current control circuit with a current stability around 1 mA, therefore the magnetic field stability is about 1 mG.

4.1.5 *Vacuum system*

The potential well generated by the MOT is not very deep so that the atoms easily escape from it. The rubidium atoms, that despite being under the influence of the cooling lasers

and the magnetic field, can easily reach speeds sufficient to escape from the confinement region if they collide with fast atoms of the background gas, so it is essential to find a way to isolate them from all material medium that can influence them. From the experimental point of view, this can mean only one thing: a sufficient level of vaccum. For this purpose, we use a system consisting of three different pumps: an ion pump (VacIon plus 20), a mechanical (Varian Mechanical Vacuum Pumps sd 40) and a turbomolecular pump (Agilent Turbo V81-AG), which are connected to the vacuum chamber system. In this system, there is also a valve separating the tube where the mechanical and turbomolecular pumps are connected from the rest of the system. Before assembling the parts, they were washed thoroughly with acetone and isopropanol to remove any dirt. Flanges using a copper ring gasket were used in the fittings to join the assembly components. In this assembly, we also coupled the dispensers (getters) of Rubidium atoms. These getters release Rubidium atoms when a current between 4 and 8 A is applied. After complete assembly of the system, two steps were performed to achieve the desired vacuum level of the order of 10^{-8} mbar. In the first stage, we connect the mechanical pump, which initially can reach 10^{-3} mbar. When the pressure reaches a suitable level, the turbomolecular pump starts to operate automatically. This pump has a rotary turbine that is controlled by an electric motor that reaches a speed of 81000 rpm and a pumping speed of 50 L/s for Nitrogen. Under these conditions, the pump reaches approximately $1,4 \times 10^{-7}$ mbar, from where the ionic pump can be connected. The latter has a pumping rate of 20 L/s for Nitrogen and a maximum initial operating pressure of 5×10^{-2} mbar. The ion pump results in a pressure of about 1×10^{-8} mbar. From that moment, the chamber valve is closed and the mechanical and turbomolecular pumps are disconnected from the system. The vacuum chamber for the MOT is made of glass, with dimensions of 5.5 cm in height and 11.0 cm in diameter. The side walls have 8 windows with a diameter of 5.0 cm each. The pressure is measured by means of the ionic pump current and it is mapped into pressure through a chart provided in the manufacturer datasheet.

Formation of the cloud

The elements mentioned above are combined in the manner shown in figure 25. The vacuum chamber is suspended and connected directly to the vacuum system (pumps). The process of creating the atomic cloud begins precisely from the release of rubidium atoms into one of the tubes of the vacuum system, nexto to the valve that maintains the vacuum, although ionic pump remains in operation. A current of approximately 9 A is applied over the dispensers (getters) through a feedthrough to proceed with the release of atoms. This liberation of rubidium is going to circulate, by free diffusion, through all the tubes that are open for circulation, arriving quickly at the glass chamber, with an inhomogeneous concentration, since the dispenser is oriented towards the chamber and not towards the ion pump.

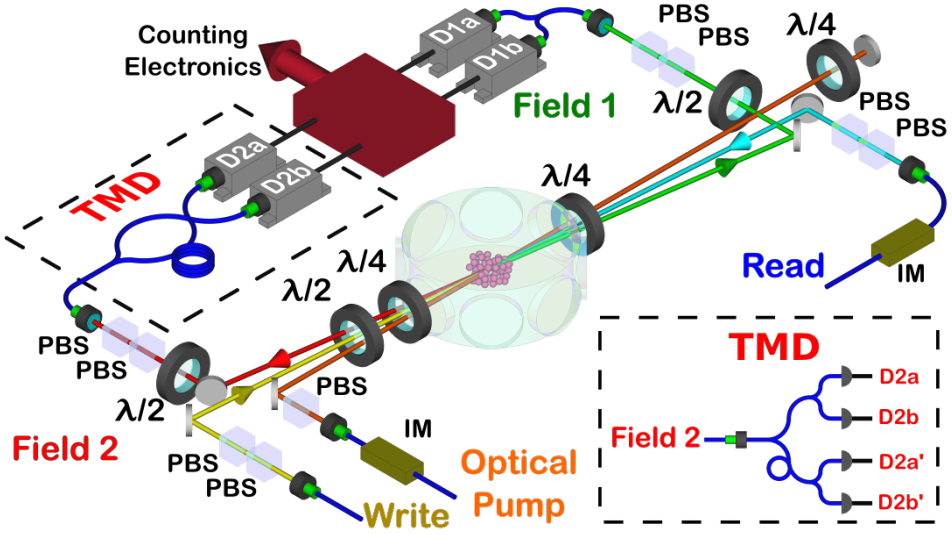

Figure 25: Experimental setup. TMD must be removed for standard DLCZ scheme.

When rubidium vapor enters the science chamber, through it there are 3 pairs of lasers crossing orthogonally to each other near the geometric center of the chamber. These 6 lasers are arranged as counterpropagating pairs, there being 2 pairs in the horizontal plane, each of them with a power around 13 mW, and a pair in the vertical axis through the large circular, upper and lower windows, with a power around 26 mW. All these powers are attained by means a laser amplifier.

In practice, the 6 lasers are usually constructed and arranged, for simplicity, like 3 lasers retroreflected in mirrors that make them return over themselves. This arrangement usually presents the problem that the reflected beam carries the shadow produced by the cloud of atoms, although this drawback is more critical when working with high optical depths. During the development of our experiments we started with the basic scheme of 3 retroreflected beams. However, the optical depths measured was limited to 2, mainly due to the lack of independence in the directions of the beams. Another reason that explains the problem of not reaching sufficiently high optical depths was the unbalance of the powers, since the reflected beams not only carries the shadow, but also were attenuated by the diverse losses in transmissions and reflections in the system. In a second stage we decided to replace the arrangement of the trapping beams in the horizontal plane. In the new configuration, the beams of the horizontal plane are now independent of each other, and only the vertical axis remained retroreflected. In order to obtain the 4 beams for the horizontal plane, it was necessary to divide the old retroreflected lasers with a polarizing beam splitter (PBS) cube prior to arrival in the vicinity of the chamber. The transmitted beam is carried to one of the windows of the science chamber, while the reflected beam goes to the opposite window. The disadvantage of this scheme is that the powers are now about half of the originals. Under this configuration, the optical depth has reached, without much difficulty, values greater than 3. However, the new limitation is now the

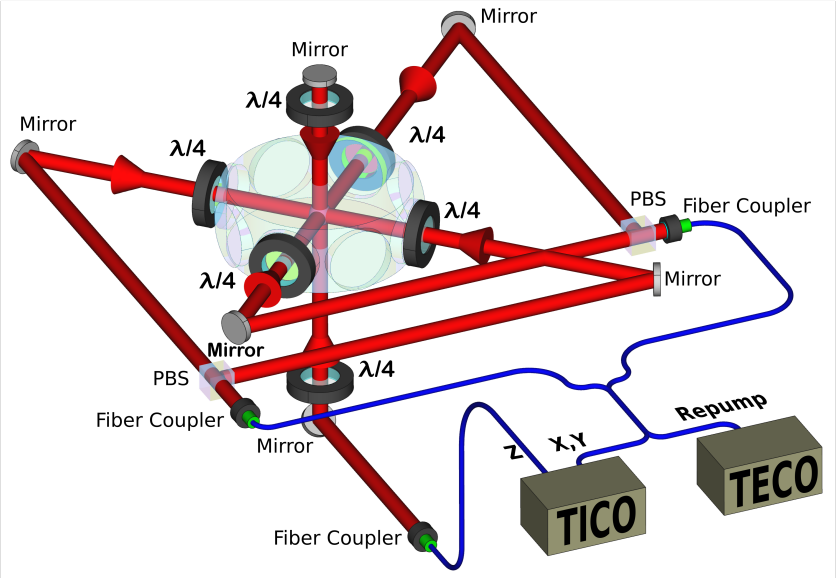

Figure 26: Experimental setup for the magneto-optical trap.

power because it is important to achieve a tighter confinement, so it was not possible to reach $OD = 4$. The measurements of OD were made through the absorption of light at resonance.

Figure 26 shows that the 4 beams of the horizontal plane, actually come from 2 beams through PBS cubes, as explained above. However, these 2 beams, in turn, come from the 2 outputs of a beam splitter in fiber, whose two inputs are, on the one hand a laser tuned at the cooling frequency and, on the other input, the repump laser. In this way we see that the repump is going to be involved in the 4 beams of the horizontal plane, all being bichromatic.

So far we have described the arrival of the atoms in the region where the laser beams cross one another. Considering only these elements, what we have is a very small region of the atomic vapor where the atoms have slowed their speed. The 3 pairs of detuned lasers, via Doppler effect, produce an effective viscous frictional force on the atoms (optical molasses). Then the magnetic field comes into play. As described above, through 2 coils in anti-Helmholtz configuration, we generate a magnetic field gradient, with zero field just in the center of the intersection of the lasers. Thanks to the presence of the field, atoms become sensitive to polarization, either to the right-handed circularly polarized light, σ^+, or left-handed circularly polarized light, σ^-, of the lasers that illuminate them (Zeeman effect). Like each pair of counterpropagating lasers consists of a laser with polarization σ^+ and the other with σ^-, then those atoms (slowed by the molasses) that travel away from the center of the trap, feel a magnetic field that increases linearly, at least in the neighborhood of the cloud. As the magnetic field grows, the Zeeman sublevels become more and more separate. On the other hand, by doing a one-dimensional analysis, these atoms are still illuminated by two lasers (one in each direction); however,

the laser propagating in the same direction as the atom is no longer of interest in our model, since its Doppler frequency decreases and it goes further away from the resonance than it already was because of the detuning. Let us now concentrate on the laser that propagates opposite to the direction in which the atom travels. If this laser is σ^+, then the atom will only have the $\Delta m_F = 1$ transition available. Since the Zeeman levels separate in energy proportional to the distance due to the magnetic field, it is enough that the atom moves away from the center of the trap so that the frequency of the transition tunes to the frequency of the laser and produces the absorption of a photon, and an exchange of momentum. If this happens many times in each atom, the net effect will be that of a restoring force that increases linearly with distance, similar to the case of a simple harmonic oscillator.

4.2 Experimental setup for the write-read process

Now we have prepared a sample of cold atoms. What we need to do is to turn off all the elements that allowed us to create the ensemble and perform the writing process, with its simultaneous detection of field 1, as well as the subsequent reading process accompanied by the detection of field 2. This process is very fast, write and read can be done in less than 1 μs, and on the other hand, the atoms in the cloud, comparatively, are very slow to leave the trap region, thus allowing us to make several repetitions of the write-read process before the cloud disappears. Below we detail the timing of the pulses.

4.2.1 *Setup*

Let's start with the explanation of the spatial distribution and polarizations of the pulses involved in the process. For simplicity we say that the pulses involved are 5, although in fact 2 of them are spontaneous photons emitted by the atoms themselves. These 5 pulses are, optical pumping, write, field 1, read and field 2.

As can be seen in figure 25, the optical pumping (OP) comes from an optical fiber that passes through an intensity modulator to perform its time-switching. It then passes through a PBS cube that cleans its polarization, leaving it as linear (horizontal). In a first stage its polarization is rotated to vertical through a half-wave plate, and then passes through a quarter-wave plate that turns it circular (σ^-) inside the science chamber. As soon as it leaves through the other window, it passes through another $\lambda/4$ plate which makes its polarization horizontal. It propagates through the free space approximately 50 cm and passes through another $\lambda/4$ plate, being reflected in a mirror and finally going back through the same $\lambda/4$ plate, so that the double pass acts as an effective $\lambda/2$ plate. The OP beam has been aligned so that it returns over itself in order to reduce the mechanical effect over the atoms. The beam passes back through the same optical elements, although this time, as is obvious, in reverse order, generating thus a σ^- light in opposite direction

over the ensemble of atoms.

The write beam is born from the same end of the optical table as the optical pump with horizontal polarization, opposite to the OP. Until reaching the ensemble of atoms, it passes through the same optical elements so that its polarization in this direction is σ^+, although they have an angle of approximately 3^{o} among them. Once on the other side of the chamber, the write beam also becomes horizontal and couples in the read optical fiber, thus ensuring the mode coupling between read and write (coupling efficiency$\sim$ 80%). The write beam focused by a lens of focal length 1 m is used near its exit from the optical fiber in order to smoothly focus the beam in the region of the MOT with a diameter of approximately 420 μm. The Rayleigh lenght is approximately 17 cm, which guarantees that, at least in the MOT region, the beam is practically collimated and Gaussian. For its part the OP has no lens and is noticeably wider than the write beam, thus covering almost the entire atomic cloud that has a diameter around 1 mm.

Field 1, although ultimately a field born in the atomic cloud, is going to be coupled in an optical fiber and detected. We need to define and characterize it. To do this we place a laser beam in the opposite direction, that is, we use the optical fiber with which we collect field 1 to emit a laser beam. With this beam, in the opposite direction, we can make the relevant alignments, and determine its waist and position within the cloud. As can be seen in figure 25, we have that this field is born in the atoms and detected with an angle of 3^o, and opposite polarization to the write laser, i.e. σ^-, then passes through a $\lambda/4$ plate close to the window where it leaves the science chamber, becoming vertically polarized. It is interesting to mention that the 3^o angle is defined for experimental simplicity since the emission is generated in all directions. In the next stage, it is reflected perpendicularly to take away from the transmitted write beam and avoid contamination, despite being in opposite polarizations. Finally it is passed through another $\lambda/2$ plate which turns it into horizontal polarization, the polarization is cleaned via 2 PBS and it is finally coupled in the optical fiber that will take it to the detection system.

The test laser for alignment serves to determine the collimation that is wanted to have at the center of the MOT. Through a lens of focal length of 1m also, we get a diameter of field 1 of approximately 150 μm. The reason why this waist is smaller, having used a lens similar to the one of the write beam, is because the diameter of the beam before the lens is greater in the case of field 1.

The read beam, as in the case of the OP, first passes through an on-fiber intensity modulator, which is responsible for its switching. It then passes through 2 PBS cubes and reaches a $\lambda/4$ plate, which is responsible for converting its original horizontal polarization into σ^-, with which the atoms are illumminted. Once on the other side of the MOT, this beam becomes vertically polarized by the $\lambda/4$ plate on the other side of the chamber. Then it passes through a $\lambda/2$ plate that leaves it with horizontal polarization, passes through 2 PBS cubes and is coupled in the optical fiber that emits the write pulse with

good efficiency, to guarantee the mode coupling.

Finally, the field 2 pulse is born in the atoms with polarization σ^+. Thanks to the $\lambda/4$ plate that is just at the exit of the chamber, its polarization becomes horizontal. Then it goes through a $\lambda/2$ plate that leaves it with vertical polarization. It is then reflected perpendicularly to separate from the read beam. Once away from the read laser optical axis, it is passed through another $\lambda/2$ plate that converts it to horizontal polarization, and then enters a polarization filter. The polarization is filtered through another set of 2 PBS cubes. Finally, this field is coupled in a optical fiber to guide to the detection system. The read and field-2 pulses have the same alignment and collimation process as the write beam and field 1, respectively, as detailed above, generating the same waists and positions in the cloud.

Detection system

When the photons in fields 1 and 2 are coupled in the optical fibers, they enter directly into one of the two arms of a single mode on-fiber beam splitter, while the other arm is unused and is covered to avoid contamination by spurious light. The beam splitter outputs have approximately the same power, for both the beam-splitters of fields 1 and 2. These beam-splitter arms are connected directly to an APD. Therefore we have 4 APD's in total, 2 for field 1 and 2 for field 2. The APD's are turned on and off through a logic pulse that is generated by an Arduino board. This pulse, which will be explained in more detail below, remains on for approximately the time the trapping lasers are off, so that the APD is ready to detect the approximately 1000 write and read trials. The APD's also have an output, which is a TTL logic pulse. Each output pulse of the APD corresponds to a photon that fired it. This electronic signal then passes through a TTL-NIM converter and then enters a photo-counting board. The converter is necessary since the board only receives the NIM (Nuclear Instrumentation Module) standard, also known as fast logic standard, a current-based logic with negative true, commnonly used in experimental particle and nuclear physics. The board used is FAST ComTec model MCS6A. Its temporal resolution is 0.1 ns, in the mode of operation employed in our experiments, and through it we can have the complete record of everything that happened during the experiment. In order to avoid storing more information than necessary, as the APD's are continuously on throughout the pulse train, it is necessary to remove the photocount information in the periods when no photons are expected coming from fields 1 or 2, which actually is most of the measurement time. For this purpose the electronic signal coming out of the APD's passes through an electronic switch, which is also controled by the Arduino board. Finally what we get is a computer file that contains all the information of the experiment encoded as a list of numerals in hexadecimal language. This file is decoded and analyzed by programs home-made specifically for these tasks, extracting both the general statistics of how many pulses were counted in each APD, as well as the histogram

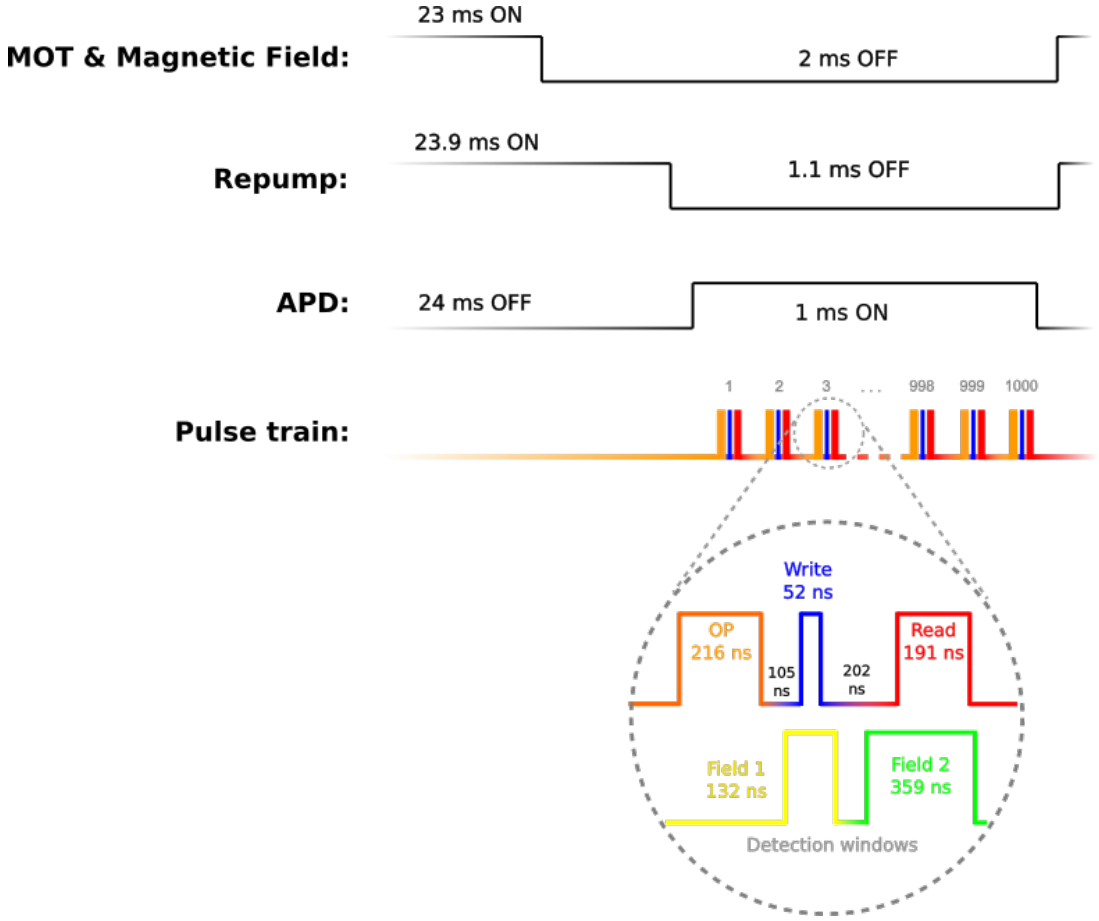

Figure 27: Timing for DLCZ scheme experiment, for both single-photon and two-photon generation.

as a function of the time of the singles (one click), doubles (2 APD's clicks), triples (three clicks) or quadruples (all APD's clicks). The most important thing is that, from this file, it is possible to get all the information to plot the wave packets we want, or any other parameter that we want investigate a posteriori.

In a second phase of the experiment, when we want to detect the generation of 2 photons in field 2, it will be necessary to make some modifications. Basically the simplest would be to place 4 APD's in the fiber that couples field 2, using a pyramidal array of 3 on-fiber beam splitters, i.e. 2 beam splitters connected to the outputs of a third beam splitter. However, another equivalent approach is the use of a Time-Multiplexed Detector (TMD), which is basically a modified on-fiber beam splitter, where one of the output arms is elongated by, in our case, ~ 20 m, then recombine both arms until the two outputs are again opened. In this way two simultaneous pulses are to be, with certain probability, temporarily separated, and thus with only 2 APD's we can access the capabilities of a system of 4 effective APD's in a totally equivalent way, with smaller efficiency, though, see Fig. 25 and its inset. The fact of needing 4 APD's, when we are only interested in a maximum of 2 clicks on field 2, is to analize the suppression of the 3-photon component.

4.2.2 *Pulse system*

The experiment is carried out in a pulsed manner, similar to the presented in [66], i.e. a sampling of write and read pulses is repeated several times in a very short time interval in order to achieve sufficient statistics on the experimental results, see figure 27.

Switching is performed on two time scales, which we call fast switching and slow switching. In the fast one we have the generation of a train of short pulses, in groups of 3 pulses, which are repeated a thousand times within a range of 1ms. In slow switching we have 4 quasi-simultaneous pulses that are repeated at a rate of 40 Hz.

It is worth noting that the fast pulse train fits entirely within a small portion of the slow switching, so we see that fast pulses are not uniformly distributed over time as the slow pulses are.

Slow switching

Slow pulses control the trapping lasers, the magnetic field, the APD pulses and the repump laser. Next we detail the functioning of each one of them.

- Trapping lasers and magnetic field

As discussed above, for the conformation of the cloud of atoms it is necessary to create a MOT. Two essential components are the trapping (cooling) lasers, as well as the magnetic field.

Since the realization of our experiment must be in absence of these two factors because they introduce decoherence to the system, we need to turn them off for a period of time long enough to perform all possible sampling before the cloud expands apreciably and then restart the MOT for another period to recover the cloud and repeat the cycle once again.

The time interval in which the trap is off must be short enough to prevent the escape of a significant number of atoms from the region of interaction with the trapping beams. Then we must determine the longest time that a peripheral atom needs to cross the interaction region of the MOT. Considering the temperature of the MOT as 1 mK, according to the Maxwell-Boltzmann distribution the mean velocity of the atoms is around 30 cm/s, so the atoms will take approximately 3 ms to cross the trap region of diameter 1 mm, which is even considerably smaller than the cloud dimensions. Therefore we need to make sure that the MOT must be turned off over a period of time less than 3 ms, so that almost none of the initially trapped atoms will be able to get out of the interaction region. In view of the above, we decided to use a 2 ms interval with the trap off and 23 ms with the trap on, giving a total period of 25 ms, i.e. a slow frequency of 40 Hz. These times are valid for both the cooling lasers and the magnetic field .

- Repump

In order to make the molasses we use the trapping lasers slightly detuned ($\sim$ 20 MHz). This detuning, on the other hand, generates the possibility of populating not only the level F'=3, but also the level F'=2. Once an atom is in $F' = 2$, it can spontaneously decay to $F = 2$ as well as to $F = 1$ (see figure 24). If it decays to $F = 2$ there is no problem, because it will be back to the optical cycle of cooling again. However, if it falls to the level $F = 1$, these atoms will no longer be able to get out of there simply through the cooling lasers. Then, it will be necessary to "repump" them back into the optical cycle. That's when the repump laser comes in acting on the transition $F = 1 \longrightarrow F' = 2$. Its switching will be very similar to that of the trapping lasers and magnetic field, except that in this case we leave the repump on for 900 μs after turning off the other pulses so as to ensure that once the optical cycles are finished, all the atoms that have been accumulated in $F = 1$ can return to the excited state $F' = 2$.

- APD Pulse

Our system of detection of fields 1 and 2, generated from the write-read process, is performed through ultra-sensitive Avalanche Photodiodes (APD). In this way, as the fast pulse train acts while the MOT and repump are off, it is necessary to have the detectors on during this time period. The APD's are turned on 50 μs after the repump is switched off and are turned off 50 μs before the repump and the MOT are turned on again. The period of time while the APD's remain on is 1 ms and being sufficient time for the complete train of fast pulses. As each trial (made of three different pulses) has an approximate duration of 1 μs , we can estimate that we will have about 1000 fast trials in each train within the period in which the APD's are on. Once the pulse train is complete, the APD pulse is turned off and remains off for the remaining 24 ms.

Fast switching

In a first round of measurements we realized that our wave packet for field 2, did not show sharp Rabi oscillations. After several measures to solve this problem we ended up finding that the problem was because the read pulse and optical pump were rising very slowly since they used to be switched on by acusto-optical modulators (AOM), with minimum rising time of 20 ns. To solve this problem, two fiber-coupled intensity modulators (IM) were added to the scheme, in addition to the AOM's, so read and optical pump lasers now are switched twice. IM's are much faster, indeed they operate within the duration of AOM pulses. In this way, in the remainder of this section, when we talk about the read and OP pulses, we are referring to the IM's switching.

Fast switching consists of two time periods, during the first one, the pulses remain off for 24 ms and during the second interval, there is a pulse train that lasts 1 ms. Approximately, fast switching has the inverse behaviour of the APD slow pulse.

The pulses that make up the fast switching are 4: optical pump, write, read and start pulse. However, hereinafter we will talk about a trio (or simply trial), since the start is just an electronic reference pulse and do not control any laser. This trio of pulses is performed in sequence within a period about 1 ms, then this trio is repeated again to complete about 1000 trials. Next we will detail how each pulse works.

- Optical pump pulse

As already explained in subsection 4.1.1, there are many Zeeman levels in the same configuration of the atoms under study. This is, basically, because the configuration is described based on hyperfine levels. As a result, more than a single Rabi frequency may appear in the experimental results, making them harder to interpret. To solve this problem we have added a laser, called optical pump (OP) that is going to pump the atoms to an extreme Zeeman level, and thus no more than a single Rabi frequency will be involved in each process. However the application of the OP can not be at any random time, it must be performed just before the write and read lasers. On the other hand, it can't be switched on so close to the write pulse, otherwise the detection of field 1, which is simultaneous with the write, can be contaminated with photons of OP. This fast pulse will have a duration of 216 ns, has a repetition period of 1 μs , for 1000 times, and after that it remains off for 24 ms.

- Write pulse

The write pulse turns on 105 ns after turning off the OP and has a duration of 52 ns. This pulse is responsible for turning on and off the AOM that tunes the frequency of the write laser. When the write pulse is turned off, we let 202 ns pass before continuing with the next pulse corresponding to the read pulse. Almost simultaneously with the arrival of the write laser on the cloud, we detect spontaneously emitted photons from the excited state in which the atoms are. This field 1 is to be detected by the APD's, which as explained above, are switched on throughout the pulse train. In order to the photo-counting board not to accumulate too much information, we apply electronic switches to the photo-counts emitted by the APD's, in such a way that these switches will only let pass the counts in the intervals in which the switch is on, and will show zero counts in the periods when it is off. These switches will be also controlled by rapid pulses that basically cover the sensing regions of field 1 (and also of field 2). The pulse that controls the electronic switch of field 1, has a duration of 132 ns.

- Read pulse

The read pulse turns on 202 ns after the write pulse is turned off, although this time could be much longer if the quantum memory properties of the system were to be exploited (up to μs), however it wasn't explored in this thesis. The reading pulse duration is 191 μs

and, once it is turned off, the three fast laser pulses are left off for a sufficient time for the period to be 1 μs . This means that after the reading pulse is turned off, it will remain off by 234 ns until we meet the next OP pulse. Similar to the case of the write pulse, here we will have the generation of field 2 simultaneously with the read pulse, so that its detection by the APD's will be guaranteed by the fact of having an APD pulse on, permanently throughout the train of 1000 read pulses. Now this will generate unnecessary detections, in times when no photons are expected from field 2, and that in the case of detecting something its source will evidently be spurious, so we will see that our photo-counting board will be forced to record much more information than necessary. The solution will be, as in the case of the write laser, the use of an electronic switch that filters the counts and let the photo-counting board to get only counts coming from the temporal regions in which it is expected to have photons of field 2. This pulse is called "detection 2" and will be turned on 31 ns after the "detection 1", for field 1, is off, and its duration is 359 ns. As we can calculate, in this way we are going to turn off this pulse before the read pulse is off, and this is because the read is longer than necessary to generate the field 2. The read laser has a double function, in its first 50 or 60 ns it generates the excitation that produces the photons of field 2, where the information stored in the atomic ensemble is extracted. The next 130 or 140 ns have been intentionally left to pump the atoms back to $F = 2$, in the same way as the repump laser does, since the read is tuned in the same transition as the repump ($F = 1 \longrightarrow F' = 2$).

- Start

The Start pulse is a time reference pulse that goes directly to the photo-counting board, where it serves as a trigger to indicate the relative delay of all pulses with respect to it. The photo-counting board only needs a pulse that goes from off to on, at a certain time. In order to be ready to turn on again, in the next trial of the fast pulse train, it will have to be turned off at some point, despite that the exact moment in which it is turned off does not matter. This pulse is switched on simultaneously when the OP is switched off, which gives us the time reference ($t = 0$) from that point on, and until the next start pulse.

With the experimental setup and all pulses described above, we can realize the experimental measurements for coincidences and wavepackets as detailed in the next chapter.

5 Heralded two-photon generation

As can be verified in the literature, the state-of-the-art in the area of single-photon quantum repeaters has a well-established foundation, particularly in the case of the DLCZ protocol [113, 125–131, 144, 146, 167–172]. Additionally, it is also possible to find fundamental studies [146, 148–150] on the reading process, which as we currently know is characterized by a superradiant phenomenon, which justifies the high efficiency of the stage. However, scaling up the discussion, when it comes to overcoming the challenges of building a quantum network, there are several aspects to consider. The specialized scientific community has been concerned with studying the various specific functions that quantum memories should eventually render as fundamental pieces of different kinds of repeater nodes in the long distance quantum communication scenario. It is possible to find that a single type of quantum memory could become insufficient to execute the diversity of tasks and it is, therefore, desirable to investigate different platforms, usually atomic. The variety of atom-light interfaces for the storage of quantum information will obviously go hand in hand with a diversity of characteristics, in which some systems will be better than others. Some reviews have already focused on it, and certain groups of features have been classified as the most common to several types of quantum memories. These characteristics are, among others, efficiency, fidelity, bandwidth, storage time and number of excitations, etc. To date, the DLCZ quantum-memory scheme has performed well compared to others in several of these features, but always in a single excitation regime. It is important to say that the fact that the DLCZ protocol has so far exploited only the storage of quantum information in a single excitation does not respond to a natural limitation of the system, but simply to a technical decision. What we propose in this thesis is to take the next step, that is, to explore for the first time the DLCZ scheme in the two-photon regime. This regime brings with it some limitations and difficulties that are worth mentioning. The probability of two photons being able to write quantum information in the atomic system, that is, inducing an atomic transition in two atoms of the ensemble simultaneously, is much lower than in the case of a single photon. On the other hand, the process of reading these two excitations is also more complex, although, as we detail in this chapter, it presents a superradiant behavior. In the present chapter

we begin by presenting some features for both the case of the single-photon superradiance and for the case of two-photon superradiance. An important characterization is the suppression of components of two excitations, in the case of the single-photon regime, thus ensuring that the power region used in those experiments makes the single excitation more likely than two or more. As a natural extension of this characterization we also present the suppression of components of 3 or more photons in the case of two photon superradiance. Our experimental results were developed for two different optical depths, which allows us to compare how superradiance behaves according to this parameter. Zeeman splitting also generates an important technical difficulty affecting our wave packets, so in this chapter we also detail the need to pump all the atoms to a specific Zeeman level. In the second section we focus specifically on the temporal behavior of the wave packets of the photon(s) emitted in field 2. Through these observations we can unveil several characteristics of both single-photon and two-photon superradiance processes . We are going to explore various possibilities when studying the storage of 2 excitations, then wave packets conditioned in various ways in this new regime are presented.

5.1 Measurement implementations

Next we will detail how we use the information provided by the photon counting board in the experiments. This method will be the same used in all the measurements considered in this chapter, except those in which a TMD has been used, for which there are specifications that will be explained later. At the end of any measurement, whether it's a test or an official measurement, we obtain a file where all data is recorded. From this file we can find the number of clicks of each of the 4 detectors, in two different ways. The first way is for each trial, that is, this file will provide us the information of which detectors clicked on every trial. However, the level of detail is very high, since this file gives us the information for each of the trials (there can be millions), one by one, and in addition it informs us in what time (with resolution of 0.1 ns) each detector fired, considering time equal to zero at the beginning of each trial. For this reason, the file that stores this information is typically large and grows proportionally to the measurement time. With this information it is possible to construct a histogram of the number of events in which one detector of field 1 and one of field 2 fired, as a function of the detection time of field 2, which represents the wave packet of the extracted photon, and which will be of fundamental importance in what follows for this chapter. The second way of studying the number of clicks is in a global way, that is, it is rather a summary of the previous way. In this case, what we have is a number of clicks for the entire measurement, in every possible way. Using a notation $N_{1a,1b,2a,2b}$, where the subscripts represent the different APD's in the way they were named in figure 28, and the possible values that these subscripts can take are only 0, 1 and X. It takes the value 0 when the detector corresponding to the

subscript has not fired, the value 1 when the detector detects a photon, and we use the value X to indicate that we are not interested in this information, i.e. we are going to count here both cases, when the corresponding APD fires and when it does not. For example, N_{10XX} means that the detector $1a$ detected a photon, while we are sure that the other detector of field 1 ($1b$) hasn't detected anything and that both detectors of field 2 ($2a$ and $2b$) may have clicked or not. Analogously to this case, there are a large number of combinations that can be explored, and some will be more useful than others. What is done to obtain these values is to count the number of trials in which this combination of detections occurred throughout the whole measurement. As during a measurement, even of the order of only a few minutes, there are many many trials, these values $N_{1a,1b,2a,2b}$, are usually large numbers. These statistical measurements are completely dispossessed of time information. However, as part of an initial characterization, they are very useful. Finally, it will also be interesting to know what is the total number of trials, N_{TOT}, performed during the whole measurement time, which is obtained directly, as well as the total measurement time in seconds, t_{TOT}.

To obtain the probability of detection of only one photon in field 1, regardless of what happened on field 2, we will use the relation

$$p_1 = \left(N_{10XX} + N_{01XX}\right)/N_{TOT}.$$

Similarly we have the probability of detecting only 1 photon on field 2

$$p_2 = \left(N_{XX10} + N_{XX01}\right)/N_{TOT},$$

and the probability of having 2 photons, but only 1 photon in each field

$$p_{12} = \left(N_{1010} + N_{1001} + N_{0110} + N_{0101}\right)/N_{TOT}.$$

The generation rate of photon pairs will represent the number of trials with a click on only one of the detectors in each field, for 1 second of measurement time. On an average over the whole time of measurement, this number will be called the "Twin Generation Rate" (TGR), given by

$$TGR = \left(N_{1010} + N_{1001} + N_{0110} + N_{0101}\right)/t_{TOT},$$

and is measured in units of Hz.

5.2 Without optical pump

The experimental setup of our first round of experiments is that shown in Figure 28, where an optical pumping laser was not used yet, so that we will not have the atoms on

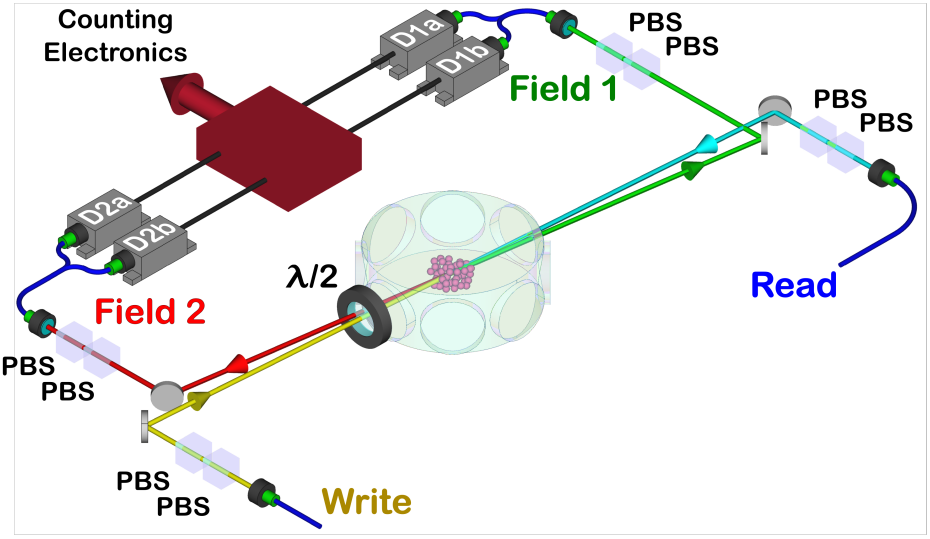

Figure 28: Setup with linear polarizations. There is no optical pump. The half wave plate is placed to rotate the transmitted polarizations by 90°.

a single Zeeman level. Here we can see that linear polarizations were used both in the write and read beams, as well as in the detected fields. We use a write pulse of 48 ns and a read pulse of 350 ns duration. The remaining characteristics are the same as those described in Chapter 4.

The most traditional characterizations for observing the behavior of the system are the optical depth, g_{12}, p_c, and TGR. These characterizations are basically focused on analyzing the single-photon regime. However, once this regime gets well defined, we are going to start moving to the 2-photon regime.

We first conduct a survey of the experimental conditions before starting a longer measurement. For this we are going to make a series of measurements for different values of p_1. In order to be able to vary p_1 in a controlled way, which corresponds to the probability that a photon is detected by one of the APD's of field 1 regardless of how many photons were detected on field 2, and without worrying about what happens to detections of field 2, it is necessary to vary the power of the write laser. The way in which we vary the power of the write beam is by using different filters before the coupling of this beam into its optical fiber.

Before beginning any experiment, we need to know some basic statistics of our system, so we need to run our experiment in different conditions. This measurement is performed for a tentative amount of time, typically about 10 minutes. The exact duration of the measurement will be inversely proportional to the power of the write laser used, since the lower this power is, the smaller the number of registered counts and therefore the errors are more significant.

The first characterization of the system presented in figure 29(b) corresponds to the cross-correlation function g_{12}. Different values of write power correspond to different

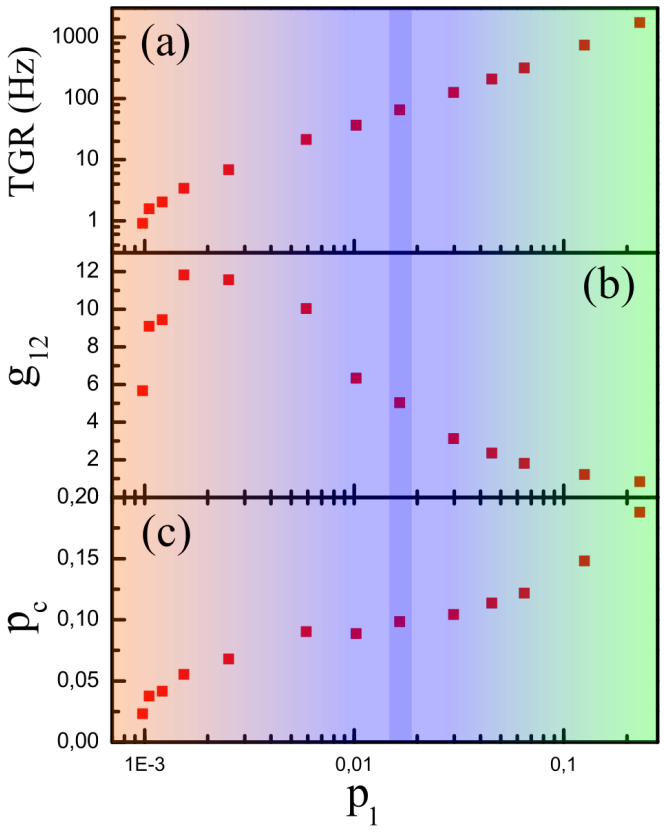

Figure 29: Characterization of first round of measurements, without optical pump and without intensity modulator as a function of p_1. Panel (a) shows TGR (twin generation rate), panel (b) is g_{12}, and (c) plots the conditional probability p_c. The actual measurement is realized with $p_1 = 0.0164$, highlighted on a blue vertical bar, where $p_c = 0.0951$, $g_{12} = 5.25$ and $TGR = 62.5$Hz. The region $p_1 \to 0$, where noise is dominant, is in orange background. The many-excitations region is in green. In the middle, there is the few (single or two) excitation regime with a blue background.

values of p_1. Recall from Chapter 3 that $g_{12} = p_{12}/(p_1 p_2)$, so we can generate the different points on the curve 29 simply from the set of counts already described above, i.e. N_{1010}, N_{1001}, N_{0110}, N_{0101}, , N_{10XX}, N_{01XX}, N_{XX10}, N_{XX01}, N_{XX01} and N_{TOT}. We can see in this curve that for very low values of p_1 the value of g_{12} becomes small, as well as for very high values of p_1. The region in which we will be interested in realizing the measurement is close to the higher values of g_{12}, since these indicate a greater correlation between the pair of photons. However, it should also be noted that the probability of detecting a photon pair conditioned upon the detection of a photon in field 1, explained in Chapter 3, and denoted as p_c, must be within reasonable values for this measurement as well.

It is for this reason that our second characterization will be precisely p_c as a function of p_1, for the same values of p_1 we showed in g_{12}, since in fact, we obtain these results from the same set of measurements. As we see in figure 29(b), there are three regions, for small values of p_1 we have that p_c grows approximately linearly, in the intermediate region of p_1 we have that p_c remains almost constant, and finally in the a third region, for high values of p_1 where again p_c grows again approximately linearly. The explanation for this is because in the region of $p_1 \to 0$ the write power is so low that the detectors click more frequently because of spurious light than for the photons emitted in the write-read process. As the spurious light has no correlation, the coincidence detections are much less likely than the singles ($p_{12} \ll p_1$), in this way $p_c \to 0$. Already in the intermediate region, which we call "single-photon region", we have that p_c becomes practically independent of p_1, and this is justified by observing that the term of a single photon in the expansion that defines our "two-mode squeezed vacuum state" is independent of the parameter p (see Eq. 3.1.18), where theoretical p is related to the experimental p_1 through the detection efficiency η_1, so $p_1 \approx \eta_1 p$. In the third region, again we see an increase proportional to p_1 since here we are not only observing a single excitation in the write field but the power is so high that the components due to several excitations appear, getting closer and closer to the classical regime. By observing together the curves of g_{12} and p_c we can determine a trade-off between these two parameters. The best region of p_1 to perform the experiment will be where g_{12} is as large as possible but without leaving the region of a single photon at p_c.

A third curve is shown in figure 29(a), which corresponds to the "twin generation rate". This measurement tells us about the generation efficiency of pairs in Hz units. It is notorious that it is monotonically increasing as a function of the write power. Through the analysis of this measurement we can predict if the write power that we are going to use is going to lead us to a measurement time excessively long. A typical measurement time in these conditions must be around some tens of hours at maximum. We try to always take the value of TGR as high as possible, although always respecting the optimization criteria for the other two curves first.

Considering all of the above, we have chosen that the point to make this measurement

would be $p_1 \approx 0.0164$, where we can see that $g_{12} = 5.25$, $p_c = 0.0951$ and $TGR = 62.5$ Hz. The choice for these values corresponds finally to the choice of a certain write power. On the other hand we have that the read power has been left fixed in a much greater value, since the extraction of the photon in field 2 is a process that must be realized with greater efficiency. The variation in the read power will lead to a modification of the Rabi frequency in the photonic wave packet, so for now it is not critical.

As explained above, the file given by the photon counting board provides us much more information than the global parameters with which we have done the characterization that led us to choose a certain write power. Through programs made in C++ language, specifically for this task, we are able to review each of the millions of trials that were recorded during a measurement. Just to get an idea, if we consider that during one of the fast pulse train we have 1000 trials, and that train is sent towards the ensemble with a rate of 40 Hz, we can estimate that there are approximately 40000 trials per second, that is about 2.6 billion trials during the 18 hours that lasted the present measurement. The most interesting thing is that we are able to access the information of each of the trials specifically, knowing exactly which detectors fired and at what time, with respect to a time origin that is set at the beginning of each new trial. With this detailed information, we were able to do a statistical study of the different detectors that clicked at each instant of time, with a resolution of 0.1 ns. That is, we can know how many trials presented a photon pair coincidence detection ($N_{1010} + N_{1001} + N_{0110} + N_{0101}$), always satisfying the condition that the photon detected in field 2 clicked at time 0.1 ns from the beginning of the trial. Then we determine the number of trials that presented photon pair coincidence, but now the condition is when the detector of field 2 fired in 0.2 ns from the beginning of the trial, and so on until completing all possible times. From this big set of numbers, we can calculate the conditional probability as a function of time, $p_c(t)$, using the ordinary definition of p_c for each time bin. By making a histogram of $p_c(t)$ as a function of the clicking time of field 2, we get precisely the wave packet of a single-photon emitted in field 2. This wave packet must be normalized, so what is done is to calculate $P_c = \sum p_c(t)\,\Delta t$ over the entire time spectrum, where the factor Δt comes from the time interval between one time bin and the next, with $\Delta t = 0.1$ ns. Then we plot the wave packet as $p_c(t)/P_c$, as seen in Fig. 30.

By doing a detailed analysis of the wave packet of figure 30, we can see that the Rabi oscillations are not sharp enough and we also observe that there are some structures within them that do not correspond to a single frequency. Anyway, we are going to be interested to see what happens when we consider the generation of 2 photons in this same regime of p_1. Analogously to the case of the single-photon wave packets, in the case of the emission of 2 photons in field 2 we take advantage of the detailed information in each of the trials. First it will be necessary to count every single trial in which the four detectors fired, this must be done for each time bin, which will allow us to find

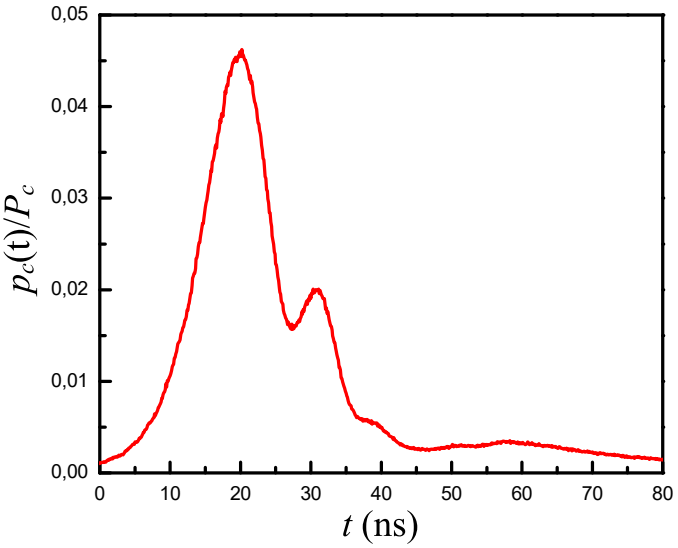

Figure 30: Single-photon wave packet, over 40 hours of measurement time, without optical pump and without intensity modulator.

the probability $p_{1122}(t_1) = N_{1111}(t_1)/N_{TOT}$ as a function of the detection time t_1 of the first of the two photons of field 2. Secondly we will need to find the probability that both APD's of field 1 have clicked, no matter what happened in field 2, let's call this probability $p_{11} = N_{11XX}/N_{TOT}$, which is a global probability and doesn't depend on time, since we are not interested in what happens to the field 2. Finally, in order to determine a histogram similar to that of a single-photon emitted in field 2, we must compute $p_{c1}(t_1) = p_{1122}(t_1)/p_{11}$. This histogram is normalized by $P_{c1} = \sum p_{c1}(t_1) \times 0.1$ and we finally get the 2-photon wave packet shown in Fig. 31, error bars correspond to poissonian statistics.

As can be noted in the graph of figure 31, the 2-photon wave packet, resembles the single-photon wave packet 30 and this is due to an effect which will be explained below, related to the theoretical model of superradiance of 2 photons when interaction effects between the excitations are neglected. Although we found interesting curves to study the generation and storage of 2 excitations in an atomic ensemble, as our aim is to study the phenomenon of superradiance in the reading process of the emitted photons, we see that the current configuration is unsatisfactory. The main reason is because we have not used optical pumping, so that more than a single Rabi frequency is found, leading to the appearance of structures due to beat-note frequencies. We also suspected that the lack of definition in Rabi oscillations is enhanced due to decoherence, leading to the loss of quantum information during the storage time. In the next sections we will try to overcome these problems. On the other hand, in figure 32 we observe the 2-photon wave packet as a function of the period of time between the first emitted photon and the second one in field 2.

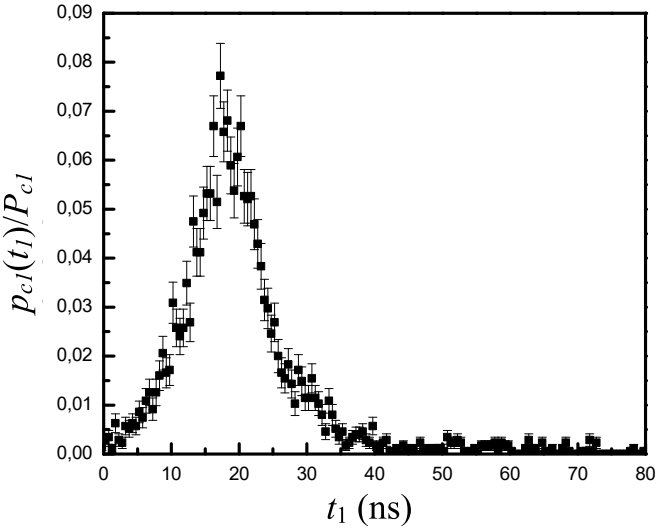

Figure 31: Two-photon wave packet for the same data set of single-photon wave packet shown in Figure 30, considering only the time of the first of the two photons.

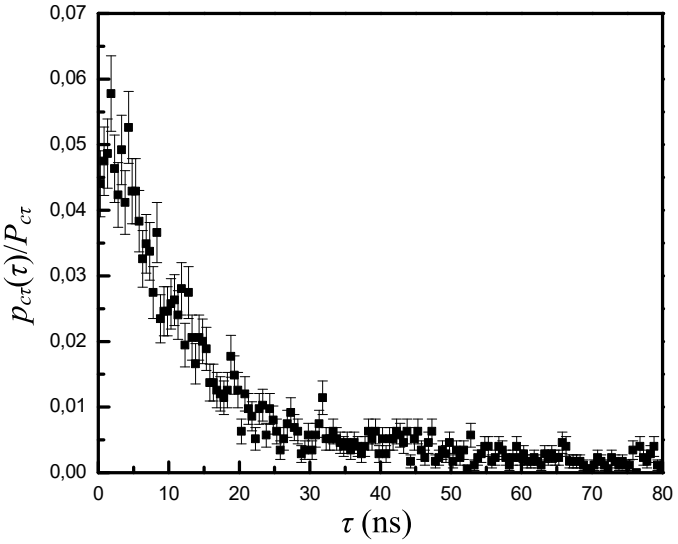

Figure 32: Two-photon wave packet as function of the time difference τ between the two emitted photons.

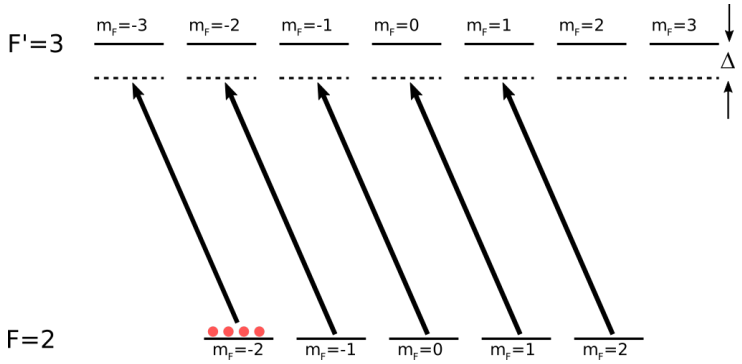

Figure 33: Optical pump process. σ^- transitions are induced for excitation in every Zeeman level of $F = 2$, however spontaneous emissions are not forced to be in any particular polarization, thus atoms tend to accumulate on the cyclic transition $F = 2, m_F = -2 \rightarrow F' = 3, m_F = -3$.

5.3 Optical pump

A well-known way to simplify the structure of levels of our system is to "pump" the atoms to a certain level in order to depopulate all other Zeeman levels and only one Λ configuration be present. Through the optical pump, we will polarize the medium, i.e. we will have the atoms at a certain extreme Zeeman level, either maximum or minimum, so that the spontaneous emission will also have a certain polarization, see Fig. 33.

If our atomic gas is illuminated by a polarized σ^- laser, the absorption will force $\Delta M = +1$ transitions. However, the emission will present, on average, $\Delta M = 0$. As we can see in figure 33, spontaneous emissions are unbalanced only in $F = 2, m_F = -2 \rightarrow F' = 3, m_F = -3$, since there is not any other level to go. Because of that, it is called a cyclic transition and, if this process is repeated a considerable number of times, the net effect will be that the electrons will populate completely the $F = 2, m_F = -2$ level. The final state is not a dark state, so there will be an effective mechanical force over the atoms in the wave vector direction. In order to cancel out this effect, it is necessary that atoms experience the same process in opposite directions, i.e. another beam with σ^- polarization from the other side. The polarization must be σ^- in the atom's frame, so in our laboratory's frame, this beam must be σ^+. With this process, our Λ configuration now is unique because the level $|g\rangle$ now can only be $\left|5^2S_{1/2}, F = 2, m_F = -2\right\rangle$, and by the polarizations and FWM condition the other levels involved now are unique as well, see Fig. 34. This will have important consequences on our wave packets, since we see that the Rabi oscillations will be much better defined, because we have only one element of the dipole matrix in the read process, which will consequently lead to a single Rabi frequency in the wave packets.

As previously explained, a consequence of the optical pump is that the medium is polarized, because all the atoms are going to stay with the electrons in the same extreme Zeeman level. One way of observing some characteristics of the experimental application of the optical pump, is through the measurement of this polarization of the medium. In a

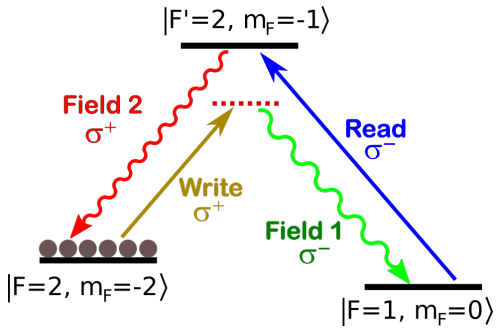

Figure 34: Λ configuration after optical pump. It pumps atoms to the $F = 2, m_F = -2$ state, which selects uniquely the other two states involved on the induced transitions by the chosen polarizations, σ^+ and σ^- for write and read beams, respectively. On the other hand, since we are considering a FWM process, the conjugated modes 1 and 2, are considered in the same transitions.

traditional optical pump scheme, we can measure the polarization of the light emitted by the medium, that in the case where the OP has been effectively carried out, will be highly polarized. As our optical pump is not the the most standard scheme, we will explain below that, in fact we observe the medium apparently less polarized than without OP, but this is related to the possible allowed transitions in each case.

We can consider the write pulse acts as a low, but effective, optical pump, since with its σ^+ polarization it induce the population to be accumulated on the levels with higher m_F values. When a measurement is done without the use of the optical pump, population is more concentrated in levels $m_F = 1$ and $m_F = 2$. The ensemble, when polarized in this way, can't emit photons of field 2 in a σ^- polarization, because it doesn't have any level to go to, then the spontaneous emissions are mostly pure σ^+. After the action of the optical pump this situation changes considerably. As a consequence of the optical pump, most of the atoms tends to populate mainly the level $F = 2, m_F = -2$, and a subsequent write pulse is applied preparing the state $F' = 2, m_F = -1$. With this we have 3 possible spontaneous emissions in the circular polarization basis. First $F' = 2, m_F = -1 \rightarrow F = 2, m_F = 0$, second we have, with a different transition frequency, $F' = 2, m_F = -1 \rightarrow F = 1, m_F = 0$, both with σ^- spontaneous emissions. Finally we have $F' = 2, m_F = -1 \rightarrow F = 2, m_F = -2$ which is σ^+ polarized. So what we have is a set of two σ^- and just one σ^+ spontaneous emission that we can detect.

At the emission direction of field 2, let's place a quarter-wave plate ($\frac{\lambda}{4}$ plate), a half-wave plate ($\frac{\lambda}{2}$ plate), a polarizing beam splitter cube (PBS) and finally a photodetector. It is important to mention that this characterization is done with only write beam. We have fixed the $\frac{\lambda}{4}$ plate in such a way the light that arrives circularly polarized turns into linearly polarized light, and we have control to rotate the $\frac{\lambda}{2}$ plate, in order to rotate that linear polarization in any direction.

If the optical pump is not performed, as shown in figure 35a, we see that the light emitted by the ensemble will be highly σ^+ polarized thanks to the write pulse. However, as we can see in figure 36, this situation is not optimal since we have a considerable

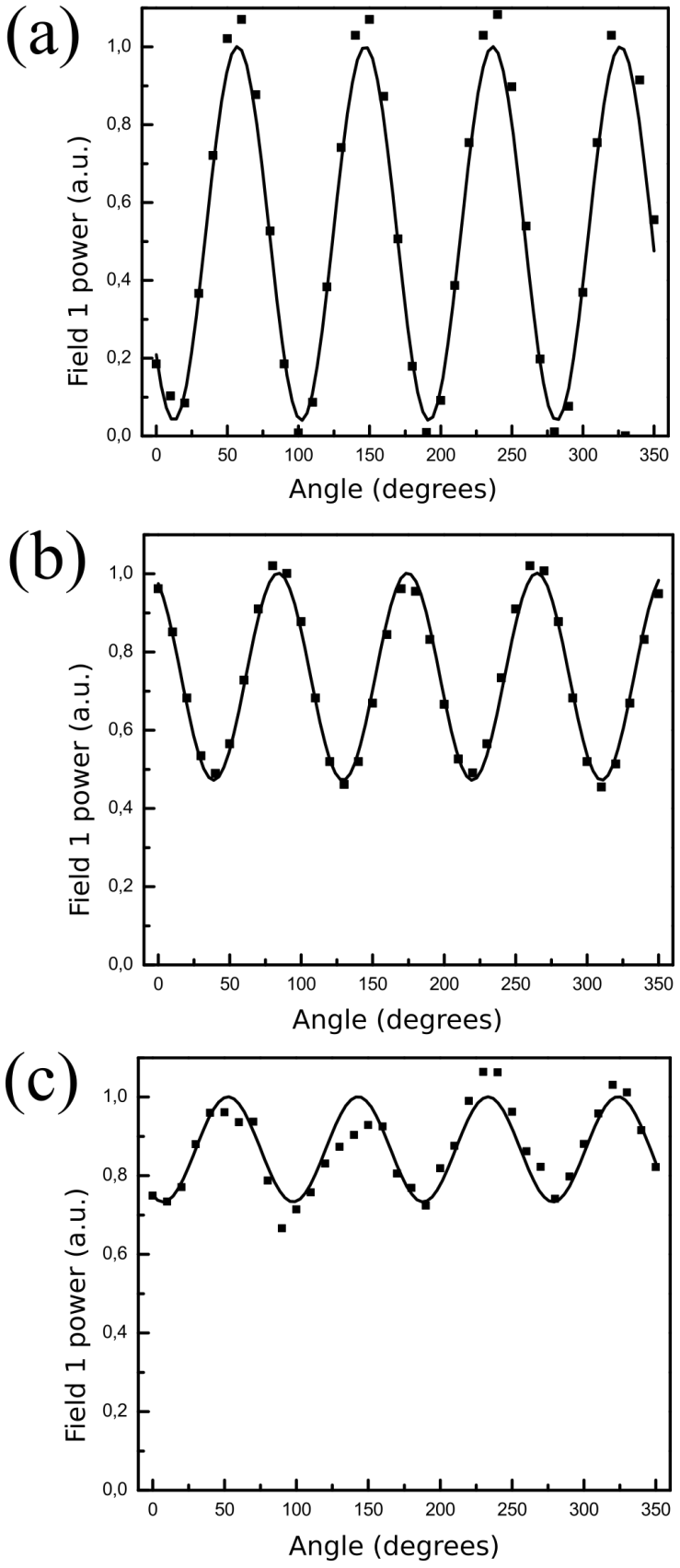

Figure 35: Study of the polarization of the atomic medium as a function of the $\lambda/2$ angle. Panel (a) shows the case without OP, (b) with two counter-propagating OP beams in orthogonal circular polarizations in the laboratory frame, and (c) with two counter-propagating σ^- OP beams in the laboratory frame.

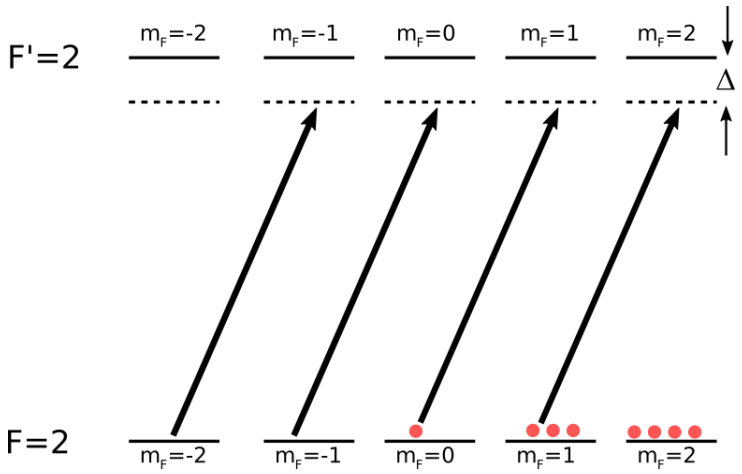

Figure 36: The action of write pulse polarizing the medium

amount of population stuck in level $F = 2, m_F = 2$, after applying the write pulse, that will be invisible for the rest of the process. If we use an OP beam, our polarization will have two components, σ^+ and σ^-, in a proportion of $1 : 2$ respectively. What we measure in figure 35b is the competition of these two components, so it explains why we observe an oscillatory behaviour that is not going to zero. In this case we have that most of the population is being taken into account because they are located at $F = 2, m_F = -2$. In figure 35c we show the situation when the counter-propagating OP beam is σ^- (in our frame). The medium is then less polarized since the counter-propagating laser is viewed as σ^+ by the ensemble, in such a way it tends to cancel the effect of the forward OP, and finally the write pulse pumping wins. As we can observe in figures 35a and c, compared with figure 35b, we have an opposite phase of the oscillatory behaviour which means exactly the change in the polarization from σ^+ to σ^-, respectively.

5.4 With optical pump but without intensity modulator

In a second round of experiments we incorporate the optical pump laser to perform the same measurements that were made before. In order to use this OP we have to move from linear polarizations to another basis of circular polarizations for all the beams of the experiment, i.e. write, read, field 1 and field 2. To achieve this change we use a quarter wave plate in each arm, before and after the atomic cloud, as shown in figure 37. In this way the fields detected at the APD's, remain linearly polarized. The OP laser is obtained by taking advantage of a mode deflected by one of the acusto-optical modulators (AOM) that generate the write laser, so that it is not necessary to install new light sources.

In this new configuration we perform the same characterizations as mentioned in the previous section, i.e. p_c, g_{12} and TGR, for different powers of the write beam. With this set of measurements we can plot the curves as a function of p_1, as can be seen in figure 38. By observing these characterizations, we find the value of p_1 to be used in the final

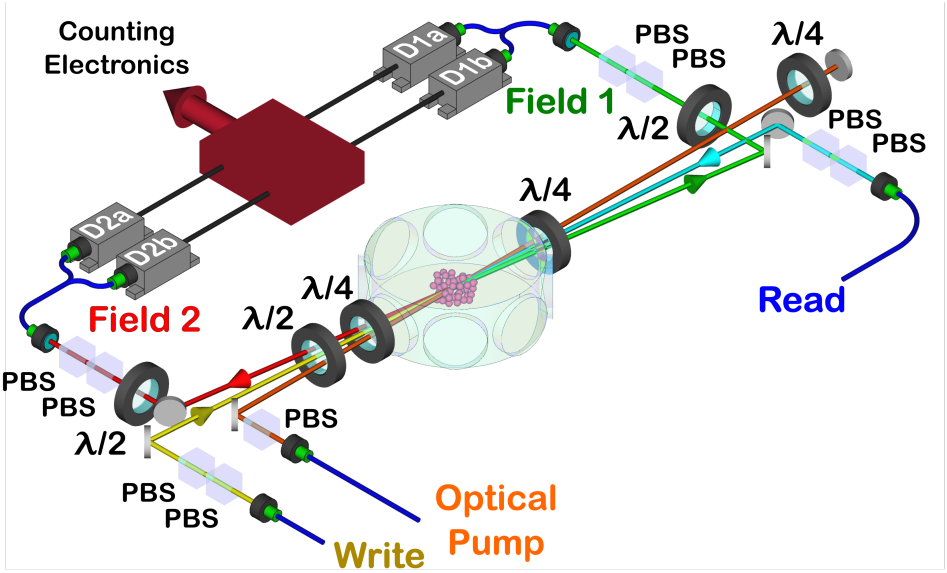

Figure 37: Experimental setup using optical pump and circular polarizations in all beams.

measurement as $p_1 = 0.018$.

In Figure 39 we can see the single-photon wave packet of the measurement made with circular polarizations, and with optical pumping polarization σ^-. Problems still exist to be able to correctly interpret this curve, mainly by the fact of not having a sharp enough Rabi frequency. One of the suspicions we had at this point, in our study, was that we were experiencing leakage radiation problems in our system. This decoherence could be due to the fact that our switching is always done through AOM's, these AOM's have an extinction ratio of 1000 to 1, as reported by the manufacturer. However, for more powerful beams this can be insufficient, since the light that is not perfectly canceled passes from one trial to the next, contaminating the stored information. In order to solve this problem, we will place in the next stage some intensity modulators (IM), whose cancellation ratio should be multiplied with the ratio of the AOM, since we will make the pulse to be switched by both devices at the same time.

Some characteristics of single-photon wavepackets are completely replicated in 2-photon wavepackets, e.g. shape of the Rabi oscillations. Since the TGR is always much greater than the generation rate of four coincidences, it is convenient to infer the overall behaviour of 2-photon wavepacket based on the single-photon one. We decided to stop the measurement when half an hour has passed by. It was simply not necessary to perform a 2-photon wave packet analysis, since the expected behaviour of the single-photon wavepacket was inappropriate to our purposes, due to switching problems that still had to be solved.

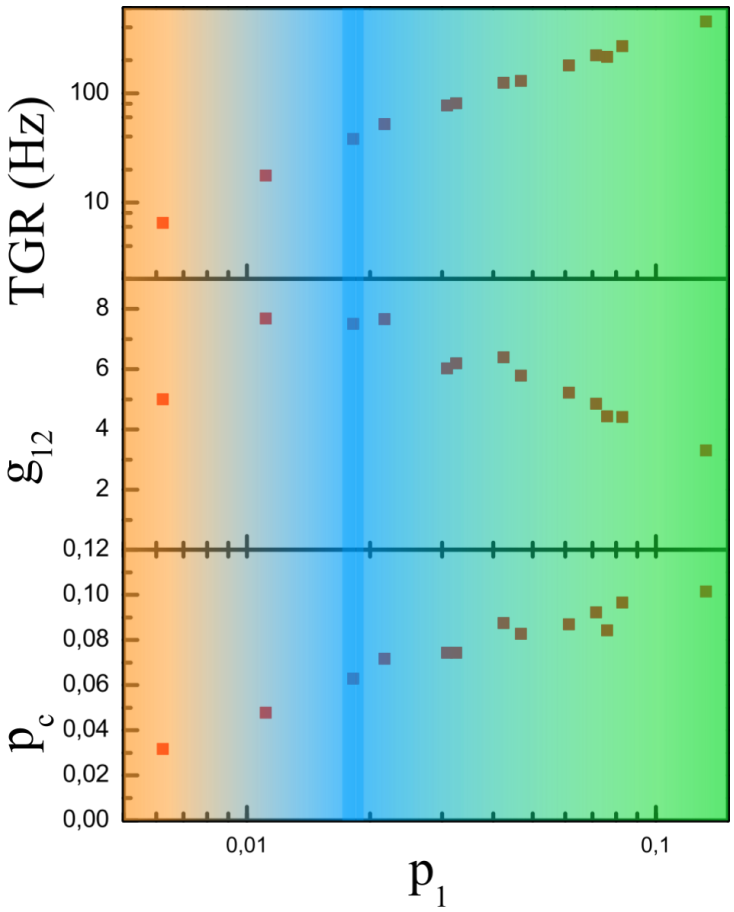

Figure 38: Characterization of measurements with optical pump but without intensity modulator as a function of p_1. Panel (a) shows TGR (twin generetion rate). Panel (b) is g_{12}, and (c) plots the conditional probability p_c. The actual measurement is realized with $p_1 = 0.018$, highlighted on a blue vertical bar. Here $p_c = 0.063$, $g_{12} = 7.5$, $TGR = 38$ Hz.

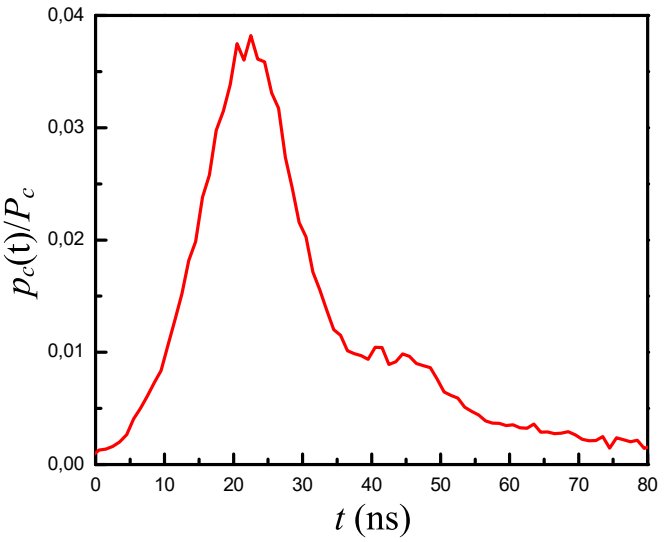

Figure 39: Single-photon wave packet using optical pump but still without the intensity modulators. We have a short measurement, just for showing the lack of definition in Rabi flops, but at least without multiple frequency components.

5.5 With optical pump and with intensity modulator

Finally, let's start the last stage of our experiment. Here we have exactly the same configuration shown in the previous section, but now we are going to improve the switching. The pulses of highest power that we are using are the read pulse and optical pumping, both of the order of mW. We have installed two on-fiber intensity modulators, one in the read laser and another in the optical pump, to help with the switching of these fields, in order to increase the coherence time of the quantum state. These IM have an interferometric nature, so they must be thermally insulated in order to prevent fluctuations of their transmission during a long measurement. These devices must be switched by a logical electronic pulse. Like all other pulses used in the experiment, we control this IM by means of the same Arduino board. Another caution that we must have with the IM is that the bias DC voltage modify the quality of the switching, that is to say, there is a specific voltage for which this device generates the greatest ratio between power of the IM pulse turned on and power of the IM pulse off. This ratio can be altered by temperature variations as well.

The characterizations for this configuration are the same as presented in the case without intensity modulator shown in figure 38, but in this case we determine that the best value to perform the measurement is $p_1 = 0.0152$, where we expect values of $p_c = 0.0627$, $g_{12} = 7.50$ and $TGR = 38$ Hz. Single-photon and a 2-photons superradiance measurements were realized during a period of 43 hours. The optical depth used in this measurement was the same as that used in all previous measurements, of the order of $OD = 3.4$. In addition, a second measurement was made equivalent to the previous one, but modifying the optical depth to $OD = 2.0$, where we used $p_1 = 0.0152$, $p_c = 0.0449$, $g_{12} = 6.35$ and $TGR = 27$ Hz. The way in which the optical depth is controlled, is altering the power of the trapping beams [146]. To modify the power of these beams, the current supply of the laser amplifier that generates the trapping beams is altered. In figure 40 we can see how the optical depth varies as a function of the current of the amplifier, when measurements are performed at the peak of the atomic resonance.

The decision to perform two measurements of single-photon and two photons wave packets, for optical depths of $OD = 3.4$ and $OD = 2.0$, is due to the fact that when we compare the parameters that are used to adjust the theoretical curve on the experimental data, it will be interesting to observe the dependence with the optical depth. This is a characteristic that we already knew from the standard single-photon superradiance experiments [146], and according to the theory developed to explain the two-photon superradiance, see section 3.2, optical depth must remain a key parameter in the behavior of the phenomenon.

We acquired three wavepackets for the state conditioned on one detection on field 1, i.e. single-photon wavepackets, all plotted on Fig. 41. The black curve on both Figs. 41a

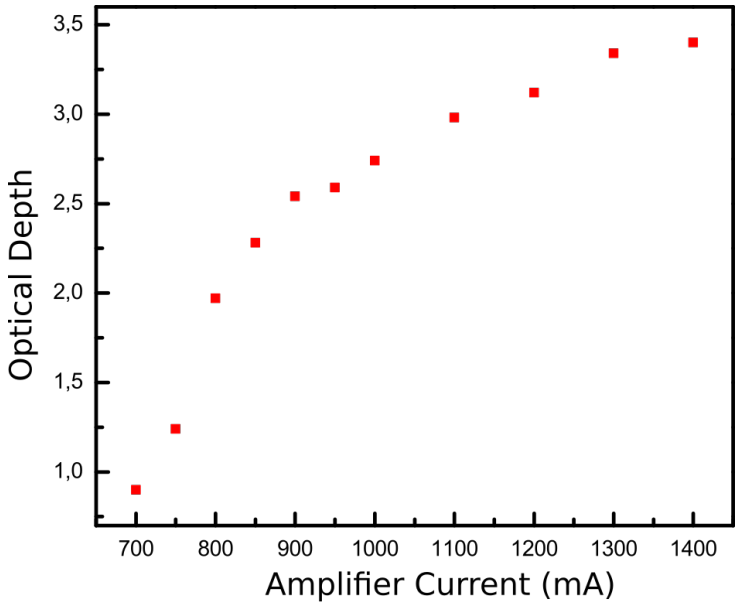

Figure 40: Relation of optical depth on current of the optical amplifier for the trapping beams.

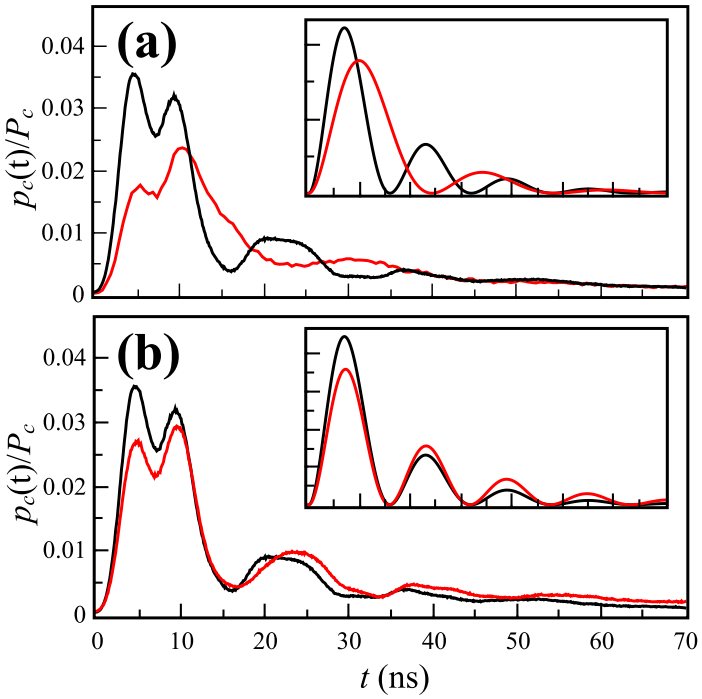

Figure 41: Single-photon wavepackets. Conditional probability $p_c(t)$ to detect a single photon on field 2 at time t once a single detection was registered on field 1, normalized by the total conditional probability P_c to detect a single-photon in field 2 at any time. (a) For $OD = 3.4$, wave packets for $I_R = 3.95$ mW (black curve) and $I_R = 1.76$ mW (red curve). (b) For $I_R = 3.95$ mW, wave packets for $OD = 3.4$ (black curve) and $OD = 2.0$ (red curve). The insets plot the corresponding theoretical curves according to Eq. 3.2.102.

and 41b is the single-photon wavepacket for an optical depth of 3.4 and a peak read power of $I_R = 3.95$ mW. This single-photon wavepacket is given by the conditioned probability $p_c(t)$ to detect a single photon on field 2 on time t after turning on the read pulse [146], with an integration window of $\Delta t = 0.5$ ns, conditioned on the detection of a single photon in field 1. The curve is normalized by the total probability $P_c = 6.3\%$ to detect a single photon on field 2 after detecting a single photon on field 1. Other important parameters for this curve are $p_1 = 0.015$ and a suppression of two-photon component $g_2 = 0.405 \pm 0.004 \approx P_{1,2}/P_{1,1}^2$, significantly below the poissonian level of 1 [175]. The red curves on panels (a) and (b) modifies the situation of the black curve to $I_R = 1.76$ mW and $OD = 2.0$, respectively.

The inset in panels (a) and (b) of Fig. 41 provide the corresponding theoretical predictions as coming from the expression 3.2.102 with $\alpha = \chi\Gamma\Omega_0^2/\Omega^2$, $\Omega = \sqrt{\Omega_0^2 - \chi^2\Gamma^2/4}$, $\Gamma/2\pi = 6.065$ MHz the natural linewidth for level $|e\rangle$, Ω_0 the Rabi frequency for the transition $|s\rangle \rightarrow |e\rangle$, and χ the superradiant enhancement for the decay $|e\rangle \rightarrow |g\rangle$. The horizontal and vertical scales are the same for the insets as for panels (a) and (b). For the black curve on the insets we assumed $\chi = 4.0$ and $\Omega_0 = 0.4 \times 10^9$rad/s. For the red curve on the inset to panel (a) we modify the Rabi frequency to 0.27×10^9rad/s, consistent with the read-power relation $\sqrt{1.76/3.95} \approx 0.67$ between the red and black experimental curves. On the inset of panel (b) the red curve is for $\chi = 2.76 = 1 + (4.0 - 1)(2.0/3.4)$, since $\chi - 1$ and OD are both proportional to the number of atoms [145, 146].

Figure 41 shows that the experimental curves for the single-photon wavepackets follow qualitatively well the previously introduced theoretical treatment of the problem, as observed in Ref [146], with a few remarks. For start, the first minimum of the experimental curves, at $t = 7$ ns, has no relation to the underlining dynamics we are investigating, and thus it is not affected by the variation of the control parameters. It comes from a small oscillation on the beginning of the read pulse that we were not able to fully eliminate due to the switching made by the intensity modulator. Second, we now have a larger background for the single-photon wavepacket, when compared to previous results [146], and it now reaches a small plateau for long times. This probably comes from a larger noise level due to the removal of a frequency filter in field 1 used on Ref. [146]. The removal of this filter resulted in a significant increase in photon-pair generation rate, up to 40 Hz. Finally, the number of atoms was changed by a relatively small amount in Fig. 39b, so as to not decrease significantly the rate of four-photons detections. Both compromises to improve the count rates were crucial for the two-photon wavepackets measurements.

Our measurements for the superradiant two-photon wavepackets, in which we detect two photons on field 2 conditioned on the detection of two photons on field 1, are shown in Fig. 42. They were obtained for two different optical depths, from the same data that generated the two curves on Fig. 41b. Figures 42a and 42c, then, were obtained on the same conditions of the black curve in Fig. 41b, and Figs. 42b and 42d on the same

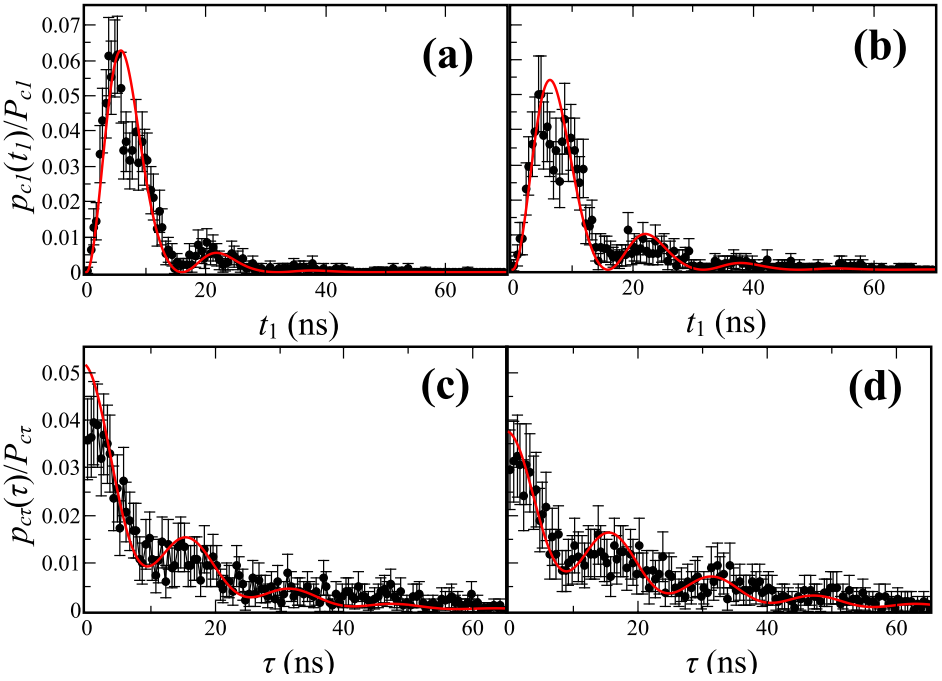

Figure 42: Two-photon wavepackets with read pulse intensity $I_R = 3.95$ mW. Panels (a) and (b): Probability $p_{c1}(t_1)$ to detect the first photon of a pair on field 2 at t_1 conditioned on two detections on field 1, with an integration window of $\Delta t_1 = 0.5$ ns and normalized by the area P_{c1} of the curve. Panels (c) and (d): Probability $p_{c\tau}(\tau)$ of detecting a second photon on field 2 at time τ after the first detection shown on panels (a) and (b), respectively, and normalized by the area $P_{c\tau}$ of the curve. Data on panels (a) and (c) , with $OD = 3.4$, resulted from the same measurements as for the experimental black curves on Fig. 41. Panels (b) and (d), with $OD = 2.0$, came from the measurements of the red curve on Fig. 41b. Red curves are the theoretical fittings.

conditions of the red curve. Since we have now two photons on field 2, the information on each wavepacket was divided on two parts. In panels (a) and (b) of Fig. 42 we plot the probability $p_{c1}(t_1)$ of detecting the first photon of the pair in field 2 at a time t_1 after turning on the read field, conditioned on two detections on field 1. In panels (c) and (d) we plot the conditional probability $p_{c\tau}(\tau)$ of detecting the second photon of the pair at a time τ after the first one. Our largest rate of four-photon generation, for the largest OD, was 14 mHz.

It is interesting to find out that effectively the 2-photon superradiance of both optical depth values, is well explained by what is expected on the theoretical model, both when it is done as a function of the detection time of the first photon on field 2, t and the other one which depends on the difference between the detection time of both photons on field 2, τ. In particular, it is worth noting that the use of optical pumping helped to define the Rabi frequency, but more important was the use of a intensity modulator so that the Rabi flops were sharpened enough to better fit the model. The explanation of this isn't related to the original purpose of installing the IM, which was decoherence reduction, but with the speed increase of the IM. Previously the read pulse was generated via just an AOM. However, in practice this pulse was not really rectangular. When the IM was installed, the pulse now became more similar to a rectangular pulse, at least on a certain scale of observation, and this rate of increase of the read pulse was crucial in order to better define the wavepackets.

5.6 Theoretical model for two-photon superradiance

If we neglect the reabsorption of the photons by the atomic ensemble, a theoretical analysis of the reading process starting with a two-photon Fock state $|2_a\rangle$ stored in the atomic ensemble leads to a simple result for the two-photon wavepacket [176]:

$$p_{cc}(t_1, t_2) = p_c(t_1)p_c(t_2). \tag{5.6.1}$$

This approximation is well justified in our system since the read process occurs in a condition of Electromagnetically Induced Transparency (EIT) [177], in which the read pulse induces a transparency in the medium for the outgoing photons. As highlighted in Ref. [146], this is an interesting feature of the present system to study superradiance, since it eliminates various complications coming from propagation effects mixed with the superradiant dynamics [178]. Figure 43 presents the level scheme and fields for the two-photon superradiance process, outlining how two excitations are mapped on the atomic ensemble, and the extraction of two photons in the superradiant reading process.

From Eq. (3.2.102) and the simple expression above relating it to the two-photon wavepacket, we derive then the theoretical functions [176] to directly compare to the experimental results of Fig. 42. By having $t_2 = t_1 + \tau > t_1$, we can integrate over τ to

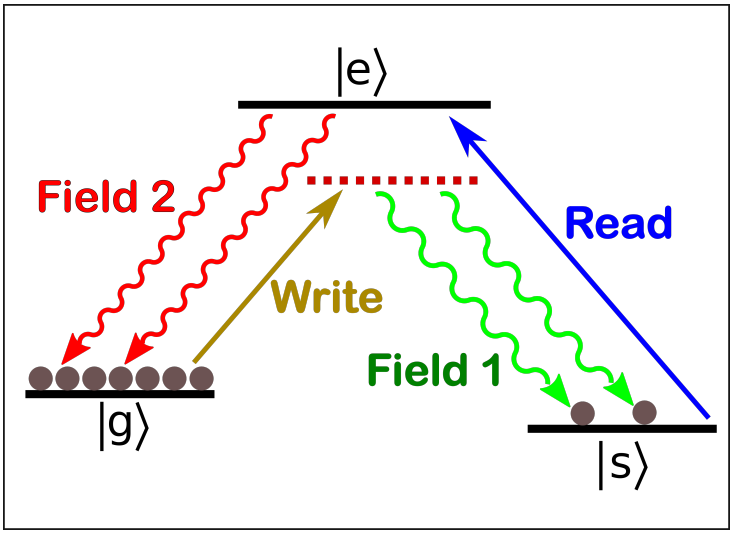

Figure 43: Level scheme and fields for two-photon superradiance.

obtain the normalized probability to detect in t_1 the first photon of the pair in field 2:

$$\frac{p_{c1}(t_1)}{P_{c1}} = 2\,\alpha\Delta t\, e^{-\chi\Gamma t}\sin^2\left(\frac{\Omega t}{2}\right)\times \\ \times\left[1+\frac{\chi\Gamma\Omega}{2\Omega_0^2}\sin(\Omega t)-\left(\frac{\chi\Gamma}{2\Omega_0}\right)^2\cos(\Omega t)\right], \tag{5.6.2}$$

where P_{c1} is a constant equal to the area under the curve for $p_{c1}(t_1)$. Equation (5.6.2) is plotted as the red curves on Fig. 42a and 42b, for the same parameter, respectively, as the black and red curves of Fig. 41b. On the other hand, if the integration run over t_1, we obtain the probability to detect the second photon in field 2 at a time τ after the first one was detected:

$$\frac{p_{c\tau}(\tau)}{P_{c\tau}} = \frac{\chi\Gamma\Omega_0^4\Delta\tau}{2\Omega^4}e^{-\chi\Gamma\tau/2}\left\{\frac{\Omega^2}{\Omega^2+\chi^2\Gamma^2}+\right. \\ \left.+\left(\frac{\Omega}{\Omega^2+\chi^2\Gamma^2}-\frac{\Omega}{2\Omega_0^2}\right)\left[\Omega\cos(\Omega\tau)+\chi\Gamma\sin(\Omega\tau)\right]\right\}, \tag{5.6.3}$$

with $P_{c\tau}$ another normalization constant to keep the area under the curve equal to one. Equation (5.6.3) provides the theoretical curves on Fig. 42c and 42d, for the same parameters as Figs. 42a and 42b, respectively. The results of Eqs. (5.6.2) and (5.6.3) clearly capture the essential aspects of the two-photon wavepackets, with the decay of $p_{c1}(t_1)$ with twice the rate of $p_{c\tau}(\tau)$ and the observation of Rabi oscillation in both curves.

5.7 Suppression of higher order components

The second term in the "two-mode squeezed vacuum" series is related to the single-photon state. To know if this state is really what we need, it is necessary to study how important

the next terms of the series are, in order to really know that we are in a write power region in which the single-photon component predominates over the 2-photons regime. We have to perform a similar analysis in the case of a state of 2 excitations. To verify that the next terms, i.e. three excitations component and higher, in the series has a low probability, it is also important to analyze certain conditional probabilities.

For the experimental realization of this characterization, we must use a slightly different scheme from the one of a normal measurement. First of all, in order to measure conditional probabilities for 3 and 4 photons, it is necessary to have, at least in field 2, more than 2 detectors. In practice, we employed 2 detectors in field 1 and 4 detectors in field 2, so we can have several types of conditional probabilities, using all combinations of clicks that can be given in this setup. To have 4 detectors in field 2, it is not always necessary to have 4 APD's, what we do is to use the 2 APD's of the standard scheme as if they were 4, by using a TMD system. This TMD is nothing more than 2 fiber beam-splitters, arranged in a cascade configuration (see Fig. 25 and its inset), but with the optical path of one of the two arms being much larger than the other. In this way, the 2 APD's act as if they were 4 APD's but in the temporal domain.

Let's recall that, using non-number-resolving detectors with an overall low efficiency (the usual case), the detection of a single photon in field 1 ideally projects the atomic ensemble in a state

$$|\psi_1\rangle \propto |1_a\rangle + p^{1/2}|2_a\rangle + p|3_a\rangle + \cdots . \tag{5.7.1}$$

On the other hand, the detection of two photons in field 1 would result in the state

$$|\psi_2\rangle \propto |2_a\rangle + p^{1/2}|3_a\rangle + \cdots . \tag{5.7.2}$$

During this characterization, we have also modified the reading pulse size for a very short duration of only 20 ns. A series of measurements is performed, for different values of the reading power, similar to what was done when characterizing p_c. As measurements were made for lower write powers, the measurement times increase rapidly, up to tens of hours in some cases.

The photon-number analysis of field 2 conditioned on one or two detections in field 1 are presented in Figs. 44a and 44b, respectively, as a function of the probability p_1 to detect a single event in field 1. $P_{i,j}$ indicates the probability to detect j photons in field 2 conditioned to the detection of i photons in field 1. In this way, Fig. 44a plots the values of $P_{1,j}$, related to $|\psi_1\rangle$, and Fig. 44b the values of $P_{2,j}$, related to $|\psi_2\rangle$. They represent average values for the various configurations of detectors in field 2 connected to each quantity. For example, $P_{1,1}$ is the average over the corresponding results for each of the four detectors in our TMD apparatus, but conditioned on the firing of either of the two detectors for field 1. $P_{1,2}$ is an average over six different configurations of pair of detectors in field 2, and so on for all the other quantities. The results for the two panels

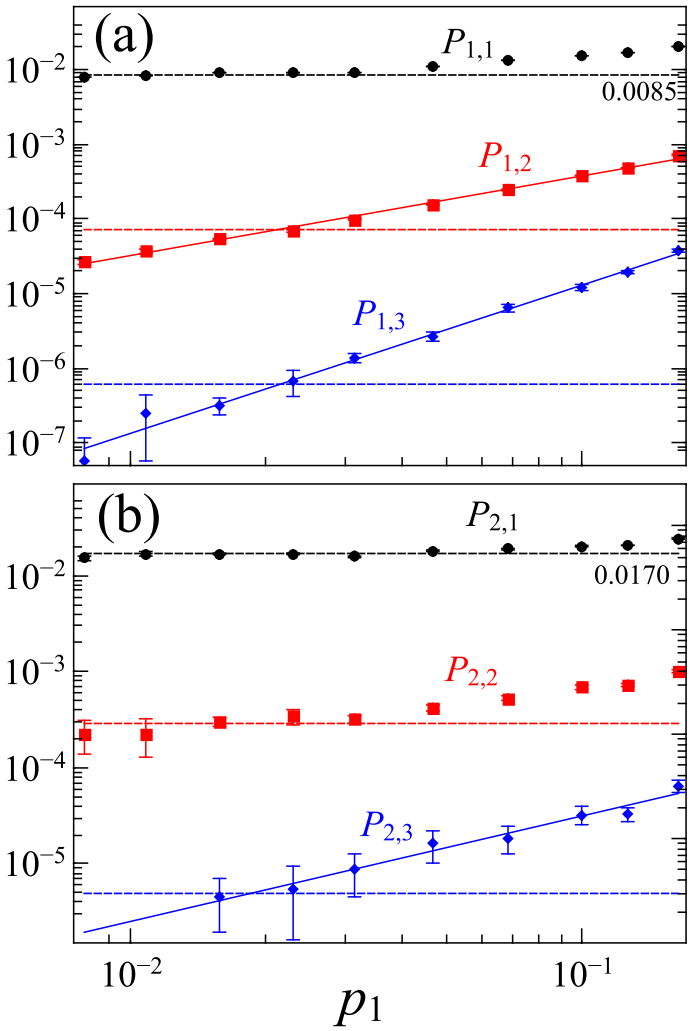

Figure 44: Probabilities $P_{i,j}$ to detect j photons of field 2 conditioned on the detection of i photons in field 1 as a function of the probability p_1 to detect one photon in field 1. (a) Probabilities conditioned to one detection in field 1. (b) Probabilities conditioned to two detections on field 1. Circles, squares, and diamonds plot the probabilities for the detection of one, two, and three photons on field 2. The solid lines are linear fits. The black dashed line provide the value for the plateau of $P_{1,i}$, which is explicitly indicated as 0.0085 for (a) and 0.0170 for (b). The red and blue dashed lines gives the square and cube, respectively, of the black one.

were obtained from the same data set.

In order to compare Fig. 44 to the expected results from Eq. (3.1.17), note first that $p_1 \approx \eta_1 p$, with η_1 the detection efficiency for field 1. As p_1 decreases, then, we observe two plateaus forming for $P_{1,1}$ and $P_{2,2}$, since those quantities should be roughly independent of p in this limit, as can be seen from Eqs. (5.7.1) and (5.7.2) for $|\psi_1\rangle$ and $|\psi_2\rangle$, respectively. If we had perfect detection, 100% efficiency and number-resolving, we should not see a component $P_{2,1}$, since only pairs of photons would be generated in field 2 after detecting two photons in field 1. However, in our limit of low detection efficiency, the loss of a photon in the pair leads to a plateau on $P_{2,1}$, but with twice the value of $P_{1,1}$, since we have now two photons entering the TMD apparatus. As explicitly indicated in Fig. 44, we observe $P_{1,1}(p_1 \to 0) \approx 0.0085$ and $P_{2,1}(p_1 \to 0) \approx 0.017$, as expected. Ideally, the

detection efficiency η_2 for field 2 should be given by $P_{1,1}$, with an overall probability to detect a photon in field 2 of $4P_{1,1} = 3.4\%$.

The Fock states $|1_a\rangle$ and $|2_a\rangle$ are limits of $|\psi_1\rangle$ and $|\psi_2\rangle$, respectively, when $p \to 0$. For finite p, there are always some higher order components, but with smaller values as p decreases. For instance, from Eq. (5.7.1) we expect the probabilities $P_{1,2}$ and $P_{1,3}$ to decrease proportional to p and p^2, respectively. From the log-log plot in Fig. 44a, we obtain $P_{1,2} \propto p_1^{s_{12}}$ and $P_{1,3} \propto p_1^{s_{13}}$, with $s_{12} = 1.07 \pm 0.02$ and $s_{13} = 1.99 \pm 0.07$, as expected. From Eq. (5.7.2), on the other hand, we expect $P_{2,3}$ to be proportional to p, obtaining $P_{2,3} \propto p_1^{s_{23}}$ with $s_{23} = 1.10 \pm 0.07$ from Fig. 44b.

We observe then the suppression of higher order components as expected for the states on Eqs. (5.7.1) and (5.7.2), resulting from corresponding projective measurements. However, it is also interesting to compare these suppressed components with the expected values for a coherent state with the level of single-photon detection probability observed in the plateaus of Figs. 44a and 44b, given by the upper dashed line. In both panels, the dashed lines in the middle and on the bottom give the square and the cube of the value for the single-photon detection level, the expected values for a coherent state. We measure then clear suppressions of $P_{1,2}$ and $P_{1,3}$ down to sub-poissonian levels. On the other hand, due to the low efficiency for detecting coincidences between five events (2 in field 1 and 3 in field 2), we could not measure $P_{2,3}$ in a clear sub-poissonian regime.

6 Conclusions

6.1 Continuous variables quantum computation

After many years of intense progress in experiments, one of the most pressing challenges of quantum computation nowadays is the enlargement of the Hilbert space available. In the CZ paradigm of ion trap quantum computing, extending the Hilbert space requires adding ever more ions to the quantum processor. As the number of ions increases, so does the influence of the environment in the form of natural decay and stray magnetic fields, the most relevant sources of environmentally driven decoherence in this kind of system. It may be said that, for general experimental realizations of a quantum processor, the desired enlargement of the Hilbert space implies as penalty greatly enlarging the *physical* size of the quantum processor, and thus the volume of actual space, i.e. the 'size' of the environment, probed by the quantum system.

In this thesis, we have tried to pursue a different route to enlarge the quantum configuration space, by using the volume in actual physical space sparingly, for a finite phonon number: a more feasible quantum computer might be that which packs a large configuration space in a small physical volume. We have here followed an alternative route that could help to mitigate the scalability problem of the ion trap quantum processor up to a certain point. The motional degrees of freedom of a single trapped ion offer, in principle, a configuration space with dimensionality restricted only by non-linearities of the trap harmonic potential. This approach has the practical advantage of causing only modest increase (polynomial) of the physical volume occupied by the atomic wave function employed in the computation, without considering an asymptotic limit though.

The main advantage of the ion trap CVQC approach might be the ability to harness sectors of the computational configuration space which are mostly disregarded in the CZ paradigm. The CVQC approach could, in principle, allow for a substantial increase in the size of the Hilbert space available for quantum computing while using current ion trap technology. The increase in manipulation and measurement complexity implied by our scheme would not be particular to it, but rather a common trait to any actual implementation of quantum computing. The fact that our scheme seems to put those challenges within the grasp of current technology, and hence bring them to our minds as

urgent matters, should be seen not only as a positive trait of our proposal, but also as a reminder of the daunting endeavor entailed in building a working quantum computer.

6.2 Two-photon superradiance

In conclusion, we demonstrated the ability to investigate the effect of superradiance in a large ensemble but with a small, controllable number of atoms in the excited state. We characterized the corresponding symmetric collective states through the photon statistics of the light emitted in the superradiance process. We also investigated the temporal dynamics of this light for both single-photon and two-photon wavepackets. There are still plenty of room to improve the system both in terms of four-photon generation rate and number of atoms in the ensemble. Larger generation rates may lead to purer single- and two-excitation states, but also to investigations of larger collective states, with three or four excitations. On the other hand, larger number of atoms, through larger optical depths of the atomic ensemble, may lead to different superradiant regimes, possibly presenting some interaction between the extracted photons. As a whole, such developments point to the feasibility of a new approach to generate and control larger and purer Fock states connected to long-lived atomic memories.

References

[1] Norman Ramsey. *Molecular beams*. Clarendon Press, 1963.

[2] JS Bell. Speakable and unspeakable in quantum mechanics. 1987.

[3] Stuart J Freedman and John F Clauser. Experimental test of local hidden-variable theories. *Phys. Rev. Lett.*, 28(14):938, 1972.

[4] Alain Aspect, Philippe Grangier, and Gérard Roger. Experimental tests of realistic local theories via bell's theorem. *Phys. Rev. Lett.*, 47(7):460, 1981.

[5] Fu-Guo Deng, Gui Lu Long, and Xiao-Shu Liu. Two-step quantum direct communication protocol using the einstein-podolsky-rosen pair block. *Phys. Rev. A*, 68(4):042317, 2003.

[6] Fei Gao, FenZhuo Guo, QiaoYan Wen, and FuChen Zhu. Revisiting the security of quantum dialogue and bidirectional quantum secure direct communication. *Sci. China Ser. G*, 51(5):559–566, 2008.

[7] Song-Kong Chong and Tzonelih Hwang. The enhancement of three-party simultaneous quantum secure direct communication scheme with epr pairs. *Opt. Commun.*, 284(1):515–518, 2011.

[8] Man Zhong-Xiao and Xia Yun-Jie. Controlled bidirectional quantum direct communication by using a ghz state. *Chin. Phys. Lett.*, 23(7):1680, 2006.

[9] Fei Gao, Fen-Zhuo Guo, Qiao-Yan Wen, and Fu-Chen Zhu. Quantum key distribution by constructing nonorthogonal states with bell states. *Int. J. Mod. Phys. B*, 24(23):4611–4618, 2010.

[10] Ulrik L Andersen, Gerd Leuchs, and Christine Silberhorn. Continuous-variable quantum information processing. *Laser & Photonics Reviews*, 4(3):337–354, 2010.

[11] Samuel L Braunstein and Arun K Pati. *Quantum information with continuous variables*. Springer Science & Business Media, 2012.

[12] Nicolas J Cerf, Gerd Leuchs, and Eugene S Polzik. *Quantum information with continuous variables of atoms and light*. Imperial College Press, 2007.

[13] Stefano Pirandola, Stefano Mancini, Seth Lloyd, and Samuel L Braunstein. Continuous-variable quantum cryptography using two-way quantum communication. *Nature Phys.*, 4(9):726–730, 2008.

[14] E Oelker, L Barsotti, S Dwyer, D Sigg, and N Mavalvala. Squeezed light for advanced gravitational wave detectors and beyond. *Opt. Express*, 22(17):21106–21121, 2014.

[15] N Treps, U Andersen, Benjamin Buchler, Ping Koy Lam, A Maitre, H-A Bachor, and Claude Fabre. Surpassing the standard quantum limit for optical imaging using nonclassical multimode light. *Phys. Rev. Lett.*, 88(20):203601, 2002.

[16] Berardo Ruggiero, Per Delsing, Carmine Granata, Yuri A Pashkin, and Paolo Silvestrini. *Quantum computing in solid state systems*. Springer Science & Business Media, 2006.

[17] Jarryd J Pla, Kuan Y Tan, Juan P Dehollain, Wee H Lim, John JL Morton, Floris A Zwanenburg, David N Jamieson, Andrew S Dzurak, and Andrea Morello. High-fidelity readout and control of a nuclear spin qubit in silicon. *Nature*, 496(7445):334–338, 2013.

[18] Daniel Loss and David P. DiVincenzo. Quantum computation with quantum dots. *Phys. Rev. A*, 57:120–126, Jan 1998.

[19] JQ You and Franco Nori. Superconducting circuits and quantum information. *Physics Today*, 58(11):42–47, 2005.

[20] Paul G Kwiat, Edo Waks, Andrew G White, Ian Appelbaum, and Philippe H Eberhard. Ultrabright source of polarization-entangled photons. *Phys. Rev. A*, 60(2):R773, 1999.

[21] J. I. Cirac and P. Zoller. Quantum computations with cold trapped ions. *Phys. Rev. Lett.*, 74:4091–4094, May 1995.

[22] C. Monroe, D. M. Meekhof, B. E. King, W. M. Itano, and D. J. Wineland. Demonstration of a fundamental quantum logic gate. *Phys. Rev. Lett.*, 75:4714–4717, Dec 1995.

[23] D. Leibfried, B. DeMarco, V. Meyer, D. Lucas, M. Barrett, J. Britton, W. M. Itano, B. Jelenkovic, C. Langer, T. Rosenband, and D. J. Wineland. Experimental demonstration of a robust, high-fidelity geometric two ion-qubit phase gate. *Nature (London)*, 422:412, 2003.

[24] Ferdinand Schmidt-Kaler, Hartmut Haffner, Mark Riebe, Stephan Gulde, Gavin P. T. Lancaster, Thomas Deuschle, Christoph Becher, Christian F. Roos, Jurgen Eschner, and Rainer Blatt. Realization of the cirac-zoller controlled-not quantum gate. *Nature (London)*, 422:408, 2003.

[25] J. I. Cirac and P. Zoller. A scalable quantum computer with ions in an array of microtraps. *Nature (London)*, 404:579, 2000.

[26] D. Kielpinski, C. Monroe, and D. J. Wineland. Architecture for a large-scale ion-trap quantum computer. *Nature (London)*, 417:709, 2002.

[27] Anders Sørensen and Klaus Mølmer. Quantum computation with ions in thermal motion. *Phys. Rev. Lett.*, 82:1971–1974, Mar 1999.

[28] G.J. Milburn, S. Schneider, and D.F.V. James. Ion trap quantum computing with warm ions. *Fortschr. Phys.*, 48(9-11):801–810, 2000.

[29] J. Mizrahi, C. Senko, B. Neyenhuis, K. G. Johnson, W. C. Campbell, C. W. S. Conover, and C. Monroe. Ultrafast spin-motion entanglement and interferometry with a single atom. *Phys. Rev. Lett.*, 110:203001, May 2013.

[30] P. C. Haljan, K.-A. Brickman, L. Deslauriers, P. J. Lee, and C. Monroe. Spin-dependent forces on trapped ions for phase-stable quantum gates and entangled states of spin and motion. *Phys. Rev. Lett.*, 94:153602, Apr 2005.

[31] RJ Glauber. Laser manipulation of atoms and ions. *Proc. Int. School of Physics 'Enrico Fermi' Course*, 118, 1992.

[32] NW McLachlan. Theory and application of mathieu functions clarendon press, 1947.

[33] M Abramowitz and IA Stegun. Handbook of mathematical functions, tenth printing, nbs. *Applied Mathematics Series*, 55, 1972.

[34] Dietrich Leibfried, Rainer Blatt, Christopher Monroe, and David Wineland. Quantum dynamics of single trapped ions. *Rev. Mod. Phys.*, 75(1):281, 2003.

[35] Hartmut Häffner, Christian F Roos, and Rainer Blatt. Quantum computing with trapped ions. *Phys. Rep.*, 469(4):155–203, 2008.

[36] C Cohen-Tannoudji, J Dupont-Roc, and G Grynberg. Atoms and photons, introduction to quantum electrodynamics, 1989.

[37] Daniel Jonathan, MB Plenio, and PL Knight. Fast quantum gates for cold trapped ions. *Phys. Rev. A*, 62(4):042307, 2000.

[38] David Deutsch. Quantum computational networks. In *Proceedings of the Royal Society of London A: Mathematical, Physical and Engineering Sciences*, volume 425, pages 73–90. The Royal Society, 1989.

[39] M. A. Nielsen and I. L. Chuang. *Quantum Computation and Quantum Information*. Cambridge University Press, 2000.

[40] EA Donley, TP Heavner, F Levi, MO Tataw, and SR Jefferts. Double-pass acousto-optic modulator system. *Review of Scientific Instruments*, 76(6):063112, 2005.

[41] Emanuel Knill, D Leibfried, R Reichle, J Britton, RB Blakestad, JD Jost, C Langer, R Ozeri, S Seidelin, and DJ Wineland. Randomized benchmarking of quantum gates. *Phys. Rev. A*, 77(1):012307, 2008.

[42] Adriano Barenco, Charles H Bennett, Richard Cleve, David P DiVincenzo, Norman Margolus, Peter Shor, Tycho Sleator, John A Smolin, and Harald Weinfurter. Elementary gates for quantum computation. *Phys. Rev. A*, 52(5):3457, 1995.

[43] Emanuel Knill. Quantum computing. *nature*, 463(7280):441–443, 2010.

[44] TD Ladd, F Jelezko, R Laflamme, Y Nakamura, C Monroe, and JL O'Brien. Quantum computers. *Nature*, 464(7285):45, 2010.

[45] Andrew M Childs and Isaac L Chuang. Universal quantum computation with two-level trapped ions. *Phys. Rev. A*, 63(1):012306, 2000.

[46] F Schmidt-Kaler, H Häffner, S Gulde, M Riebe, GPT Lancaster, T Deuschle, C Becher, W Hänsel, J Eschner, CF Roos, et al. How to realize a universal quantum gate with trapped ions. *Appl. Phys. B*, 77(8):789–796, 2003.

[47] M Riebe, K Kim, P Schindler, T Monz, PO Schmidt, TK Körber, W Hänsel, H Häffner, CF Roos, and R Blatt. Process tomography of ion trap quantum gates. *Phys. Rev. Lett.*, 97(22):220407, 2006.

[48] Andrew Steane, Ch F Roos, D Stevens, A Mundt, D Leibfried, F Schmidt-Kaler, and R Blatt. Speed of ion--trap quantum-information processors. *Phys. Rev. A*, 62(4):042305, 2000.

[49] H Häffner, S Gulde, M Riebe, G Lancaster, C Becher, J Eschner, F Schmidt-Kaler, and Rainer Blatt. Precision measurement and compensation of optical stark shifts for an ion-trap quantum processor. *Phys. Rev. Lett.*, 90(14):143602, 2003.

[50] Seth Lloyd and Samuel L. Braunstein. Quantum computation over continuous variables. *Phys. Rev. Lett.*, 82:1784–1787, Feb 1999.

[51] Samuel L. Braunstein and Peter van Loock. Quantum information with continuous variables. *Rev. Mod. Phys.*, 77:513–577, Jun 2005.

[52] Arvind, B. Dutta, N. Mukunda, and R. Simon. The real symplectic groups in quantum mechanics and optics. *Pramana*, 45:471–497, 2005.

[53] J. Eisert and M. B. Plenio. Introduction to the basics of entanglement theory in continuous-variable systems. *Int. J. Quantum Inform.*, 01(04):479–506, 2003.

[54] Stephen D. Bartlett, Barry C. Sanders, Samuel L. Braunstein, and Kae Nemoto. Efficient classical simulation of continuous variable quantum information processes. *Phys. Rev. Lett.*, 88:097904, Feb 2002.

[55] Stephen D. Bartlett and Barry C. Sanders. Universal continuous-variable quantum computation: Requirement of optical nonlinearity for photon counting. *Phys. Rev. A*, 65:042304, Mar 2002.

[56] C. Monroe, D. M. Meekhof, B. E. King, and D. J. Wineland. A "schrödinger cat" superposition state of an atom. *Science*, 272(5265):1131–1136, 1996.

[57] E. Solano, R. L. de Matos Filho, and N. Zagury. Deterministic bell states and measurement of the motional state of two trapped ions. *Phys. Rev. A*, 59:R2539–R2543, Apr 1999.

[58] D. Leibfried, D. M. Meekhof, B. E. King, C. Monroe, W. M. Itano, and D. J. Wineland. Experimental determination of the motional quantum state of a trapped atom. *Phys. Rev. Lett.*, 77:4281–4285, Nov 1996.

[59] E. Solano, R. L. de Matos Filho, and N. Zagury. Mesoscopic superpositions of vibronic collective states of N trapped ions. *Phys. Rev. Lett.*, 87:060402, Jul 2001.

[60] Brian Vlastakis, Gerhard Kirchmair, Zaki Leghtas, Simon E. Nigg, Luigi Frunzio, S. M. Girvin, Mazyar Mirrahimi, M. H. Devoret, and R. J. Schoelkopf. Deterministically encoding quantum information using 100-photon schrödinger cat states. *Science*, 342(6158):607–610, 2013.

[61] S. Haroche and J.-M. Raimond. *Exploring the Quantum: Atoms, Cavities, and Photons*. Oxford Univ. Press, 2006.

[62] Alessio Serafini, Alex Retzker, and Martin B Plenio. Manipulating the quantum information of the radial modes of trapped ions: linear phononics, entanglement generation, quantum state transmission and non-locality tests. *New J. Phys.*, 11(2):023007, 2009.

[63] J Alonso, F M Leupold, B C Keitch, and J P Home. Quantum control of the motional states of trapped ions through fast switching of trapping potentials. *New J. Phys.*, 15(2):023001, 2013.

[64] Shiqian Ding, Huanqian Loh, Roland Hablutzel, Meng Gao, Gleb Maslennikov, and Dzmitry Matsukevich. Microwave control of trapped-ion motion assisted by a running optical lattice. *Phys. Rev. Lett.*, 113:073002, Aug 2014.

[65] Safoura Mirkhalaf and Klaus Mølmer. Sympathetic wigner-function tomography of a dark trapped ion. *Phys. Rev. A*, 85:042109, Apr 2012.

[66] K. G. Johnson, B. Neyenhuis, J. Mizrahi, J. D. Wong-Campos, and C. Monroe. Sensing atomic motion from the zero point to room temperature with ultrafast atom interferometry. *Phys. Rev. Lett.*, 115:213001, Nov 2015.

[67] A. Hashemloo, C. M. Dion, and G. Rahali. Wave packet dynamics of an atomic ion in a paul trap. *Int. J. Mod. Phys. C*, 27(02):1650014, 2016.

[68] F. Nicacio, K. Furuya, and F. L. Semião. Motional entanglement with trapped ions and a nanomechanical resonator. *Phys. Rev. A*, 88:022330, Aug 2013.

[69] Xun-Wei Xu, Hui Wang, Jing Zhang, and Yu-xi Liu. Engineering of nonclassical motional states in optomechanical systems. *Phys. Rev. A*, 88:063819, Dec 2013.

[70] S R Miry and M K Tavassoly. Generation of nonlinear motional trio coherent states and their nonclassical properties. *J. Phys. B*, 45(17):175502, 2012.

[71] D Rodríguez-Méndez and H Moya-Cessa. High noon states in trapped ions. *Phys. Scr.*, 2012(T147):014028, 2012.

[72] Shinsuke Haze, Yusuke Tateishi, Atsushi Noguchi, Kenji Toyoda, and Shinji Urabe. Observation of phonon hopping in radial vibrational modes of trapped ions. *Phys. Rev. A*, 85:031401, Mar 2012.

[73] T. Dutta, M. Mukherjee, and K. Sengupta. Nonequilibrium phonon dynamics in trapped-ion systems. *Phys. Rev. A*, 85:063401, Jun 2012.

[74] T. Dutta, M. Mukherjee, and K. Sengupta. Ramp dynamics of phonons in an ion trap: Entanglement generation and cooling. *Phys. Rev. Lett.*, 111:170406, Oct 2013.

[75] M Orszag and Francisco Larrain. Generation of a c-not gate using a trapped ion. *J. Opt. B: Quant. Semiclass. Opt.*, 7(12):S754, 2005.

[76] Zhang Shi-Jun, Ma Chi, Zhang Wen-Hai, and Ye Liu. One step to generate quantum controlled phase-shift gate using a trapped ion. *Chin. Phys. B*, 17(5):1593, 2008.

[77] Hoi-Kwan Lau and Daniel F. V. James. Proposal for a scalable universal bosonic simulator using individually trapped ions. *Phys. Rev. A*, 85:062329, Jun 2012.

[78] R. L. de Matos Filho and W. Vogel. Quantum nondemolition measurement of the motional energy of a trapped atom. *Phys. Rev. Lett.*, 76:4520–4523, Jun 1996.

[79] L. Davidovich, M. Orszag, and N. Zagury. Quantum nondemolition measurements of vibrational populations in ionic traps. *Phys. Rev. A*, 54:5118–5125, Dec 1996.

[80] L. G. Lutterbach and L. Davidovich. Method for direct measurement of the wigner function in cavity qed and ion traps. *Phys. Rev. Lett.*, 78:2547–2550, Mar 1997.

[81] Luis Ortiz-Gutiérrez, Bruna Gabrielly, Luis F Muñoz, Kainã T Pereira, Jefferson G Filgueiras, and Alessandro S Villar. Continuous variables quantum computation over the vibrational modes of a single trapped ion. *Optics Communications*, 397:166–174, 2017.

[82] Anders Sørensen and Klaus Mølmer. Entanglement and quantum computation with ions in thermal motion. *Phys. Rev. A*, 62:022311, Jul 2000.

[83] Christian F Roos. Ion trap quantum gates with amplitude-modulated laser beams. *New J. Phys.*, 10(1):013002, 2008.

[84] D. M. Meekhof, C. Monroe, B. E. King, W. M. Itano, and D. J. Wineland. Generation of nonclassical motional states of a trapped atom. *Phys. Rev. Lett.*, 76:1796–1799, Mar 1996.

[85] Hsiang-Yu Lo, Daniel Kienzler, Ludwig de Clercq, Matteo Marinelli, Vlad Negnevitsky, Ben C. Keitch, and Jonathan P. Home. Spin-motion entanglement and state diagnosis with squeezed oscillator wavepackets. *Nature (London)*, 521:336, 2015.

[86] D. Leibfried, R. Blatt, C. Monroe, and D. Wineland. Quantum dynamics of single trapped ions. *Rev. Mod. Phys.*, 75:281–324, Mar 2003.

[87] Maryam Roghani and Hanspeter Helm. Trapped-atom cooling beyond the lamb-dicke limit using electromagnetically induced transparency. *Phys. Rev. A*, 77:043418, Apr 2008.

[88] Héctor Moya-Cessa, Francisco Soto-Eguibar, José M. Vargas-Martínez, Raúl Juárez-Amaro, and Arturo Zú niga Segundo. Ion laser interactions: The most complete solution. *Phys. Rep.*, 513(5):229 – 261, 2012.

[89] A. Einstein, B. Podolsky, and N. Rosen. Can quantum-mechanical description of physical reality be considered complete? *Phys. Rev.*, 47:777–780, May 1935.

[90] S. R. Jefferts, C. Monroe, E. W. Bell, and D. J. Wineland. Coaxial-resonator-driven rf (paul) trap for strong confinement. *Phys. Rev. A*, 51:3112–3116, Apr 1995.

[91] D. J. Wineland, C. Monroe, W. M. Itano, D. Leibfried, B. E. King, and D. M. Meekhof. Experimental issues in coherent quantum state manipulation of trapped atomic ions. *J. Res. Natl. Inst. Stand. Tech.*, 103:259, 1998.

[92] U. Poschinger, A. Walther, M. Hettrich, F. Ziesel, and F. Schmidt-Kaler. Interaction of a laser with a qubit in thermal motion and its application to robust and efficient readout. *Appl. Phys. B*, 107(4):1159–1165, 2012.

[93] F. Zähringer, G. Kirchmair, R. Gerritsma, E. Solano, R. Blatt, and C. F. Roos. Realization of a quantum walk with one and two trapped ions. *Phys. Rev. Lett.*, 104:100503, Mar 2010.

[94] Thomas Monz, Philipp Schindler, Julio T. Barreiro, Michael Chwalla, Daniel Nigg, William A. Coish, Maximilian Harlander, Wolfgang Hänsel, Markus Hennrich, and Rainer Blatt. 14-qubit entanglement: Creation and coherence. *Phys. Rev. Lett.*, 106:130506, Mar 2011.

[95] Seth Lloyd and Jean-Jacques E. Slotine. Analog quantum error correction. *Phys. Rev. Lett.*, 80:4088–4091, May 1998.

[96] Daniel S. Abrams and Seth Lloyd. Quantum algorithm providing exponential speed increase for finding eigenvalues and eigenvectors. *Phys. Rev. Lett.*, 83:5162–5165, Dec 1999.

[97] Daniel Gottesman, Alexei Kitaev, and John Preskill. Encoding a qubit in an oscillator. *Phys. Rev. A*, 64:012310, Jun 2001.

[98] F Schmidt-Kaler, S Gulde, M Riebe, T Deuschle, A Kreuter, G Lancaster, C Becher, J Eschner, H HÃ€ffner, and R Blatt. The coherence of qubits based on single ca + ions. *J. Phys. B: At. Mol. Opt. Phys.*, 36(3):623, 2003.

[99] T. Monz, K. Kim, W. Hänsel, M. Riebe, A. S. Villar, P. Schindler, M. Chwalla, M. Hennrich, and R. Blatt. Realization of the quantum toffoli gate with trapped ions. *Phys. Rev. Lett.*, 102:040501, Jan 2009.

[100] D. M. Lucas, B. C. Keitch, J. P. Home, G. Imreh, M. J. McDonnell, D. N. Stacey, D. J. Szwer, and A. M. Steane. A long-lived memory qubit on a low-decoherence quantum bus, 2007.

[101] Christian F Roos. Ion trap quantum gates with amplitude-modulated laser beams. *New J. Phys.*, 10(1):013002, 2008.

[102] Ying Li and Simon C. Benjamin. Hierarchical surface code for network quantum computing with modules of arbitrary size. *Phys. Rev. A*, 94:042303, Oct 2016.

[103] L-M Duan, MD Lukin, J Ignacio Cirac, and Peter Zoller. Long-distance quantum communication with atomic ensembles and linear optics. *Nature*, 414(6862):413–418, 2001.

[104] DGBJ Dieks. Communication by epr devices. *Phys. Lett. A*, 92(6):271–272, 1982.

[105] William K Wootters and Wojciech H Zurek. A single quantum cannot be cloned. *Nature*, 299(5886):802–803, 1982.

[106] M Żukowski, A Zeilinger, MA Horne, and AK Ekert. "event-ready-detectors" bell experiment via entanglement swapping. *Phys. Rev. Lett.*, 71(26):4287, 1993.

[107] H-J Briegel, Wolfgang Dür, Juan I Cirac, and Peter Zoller. Quantum repeaters: the role of imperfect local operations in quantum communication. *Phys. Rev. Lett.*, 81(26):5932, 1998.

[108] H Jeff Kimble. The quantum internet. *Nature*, 453(7198):1023–1030, 2008.

[109] Stefano Pirandola and Samuel L Braunstein. Physics: Unite to build a quantum internet. *Nature*, 532:169–171, 2016.

[110] Shuai Chen, Yu-Ao Chen, Thorsten Strassel, Zhen-Sheng Yuan, Bo Zhao, Jörg Schmiedmayer, and Jian-Wei Pan. Deterministic and storable single-photon source based on a quantum memory. *Phys. Rev. Lett.*, 97:173004, Oct 2006.

[111] P Michler, A Kiraz, C Becher, WV Schoenfeld, PM Petroff, Lidong Zhang, E Hu, and A Imamoglu. A quantum dot single-photon turnstile device. *Science*, 290(5500):2282–2285, 2000.

[112] J McKeever, A Boca, AD Boozer, R Miller, JR Buck, A Kuzmich, and HJ Kimble. Deterministic generation of single photons from one atom trapped in a cavity. *Science*, 303(5666):1992–1994, 2004.

[113] CW Chou, SV Polyakov, A Kuzmich, and HJ Kimble. Single-photon generation from stored excitation in an atomic ensemble. *Phys. Rev. Lett.*, 92(21):213601, 2004.

[114] Chin-Wen Chou, H De Riedmatten, D Felinto, SV Polyakov, SJ Van Enk, and H Jeff Kimble. Measurement-induced entanglement for excitation stored in remote atomic ensembles. *Nature*, 438(7069):828–832, 2005.

[115] KS Choi, A Goban, SB Papp, SJ Van Enk, and HJ Kimble. Entanglement of spin waves among four quantum memories. *Nature*, 468(7322):412–416, 2010.

[116] Emanuel Knill, Raymond Laflamme, and Gerald J Milburn. A scheme for efficient quantum computation with linear optics. *Nature*, 409(6816):46–52, 2001.

[117] Pieter Kok, William J Munro, Kae Nemoto, Timothy C Ralph, Jonathan P Dowling, and Gerard J Milburn. Linear optical quantum computing with photonic qubits. *Rev. Mod. Phys.*, 79(1):135, 2007.

[118] JD Franson, BC Jacobs, and TB Pittman. Quantum computing using single photons and the zeno effect. *Phys. Rev. A*, 70(6):062302, 2004.

[119] Alexios Beveratos, Rosa Brouri, Thierry Gacoin, André Villing, Jean-Philippe Poizat, and Philippe Grangier. Single photon quantum cryptography. *Phys. Rev. Lett.*, 89(18):187901, 2002.

[120] Sean D Barrett, Peter P Rohde, and Thomas M Stace. Scalable quantum computing with atomic ensembles. *New J. Phys.*, 12(9):093032, 2010.

[121] Chin-Wen Chou, Julien Laurat, Hui Deng, Kyung Soo Choi, Hugues De Riedmatten, Daniel Felinto, and H Jeff Kimble. Functional quantum nodes for entanglement distribution over scalable quantum networks. *Science*, 316(5829):1316–1320, 2007.

[122] Alfred B U'Ren, Christine Silberhorn, Konrad Banaszek, and Ian A Walmsley. Efficient conditional preparation of high-fidelity single photon states for fiber-optic quantum networks. *Phys. Rev. Lett.*, 93(9):093601, 2004.

[123] John F Clauser. Experimental distinction between the quantum and classical field-theoretic predictions for the photoelectric effect. *Phys. Rev. D*, 9(4):853, 1974.

[124] L Mandel. Quantum effects in one-photon and two-photon interference. *Rev. Mod. Phys.*, 71(2):S274, 1999.

[125] A Kuzmich, WP Bowen, AD Boozer, A Boca, CW Chou, L-M Duan, and HJ Kimble. Generation of nonclassical photon pairs for scalable quantum communication with atomic ensembles. *Nature*, 423(6941):731–734, 2003.

[126] D Felinto, CW Chou, H De Riedmatten, SV Polyakov, and HJ Kimble. Control of decoherence in the generation of photon pairs from atomic ensembles. *Phys. Rev. A*, 72(5):053809, 2005.

[127] Julien Laurat, Hugues De Riedmatten, Daniel Felinto, Chin-Wen Chou, Erik W Schomburg, and H Jeff Kimble. Efficient retrieval of a single excitation stored in an atomic ensemble. *Optics express*, 14(15):6912–6918, 2006.

[128] Kyung Soo Choi, Hui Deng, Julien Laurat, and HJ Kimble. Mapping photonic entanglement into and out of a quantum memory. *Nature*, 452(7183):67–71, 2008.

[129] Hugues De Riedmatten, Julien Laurat, Chin-Wen Chou, EW Schomburg, Daniel Felinto, and H Jeff Kimble. Direct measurement of decoherence for entanglement between a photon and stored atomic excitation. *Phys. Rev. Lett.*, 97(11):113603, 2006.

[130] Julien Laurat, Chin-wen Chou, Hui Deng, Kyung Soo Choi, Daniel Felinto, Hugues de Riedmatten, and HJ Kimble. Towards experimental entanglement connection with atomic ensembles in the single excitation regime. *New J. Phys.*, 9(6):207, 2007.

[131] SV Polyakov, CW Chou, D Felinto, and HJ Kimble. Temporal dynamics of photon pairs generated by an atomic ensemble. *Phys. Rev. Lett.*, 93(26):263601, 2004.

[132] Klemens Hammerer, Anders S Sørensen, and Eugene S Polzik. Quantum interface between light and atomic ensembles. *Rev. Mod. Phys.*, 82(2):1041, 2010.

[133] David C Burnham and Donald L Weinberg. Observation of simultaneity in parametric production of optical photon pairs. *Phys. Rev. Lett.*, 25(2):84, 1970.

[134] CK Hong and L Mandel. Theory of parametric frequency down conversion of light. *Phys. Rev. A*, 31(4):2409, 1985.

[135] Ling-An Wu, HJ Kimble, JL Hall, and Huifa Wu. Generation of squeezed states by parametric down conversion. *Phys. Rev. Lett.*, 57(20):2520, 1986.

[136] CK Hong, Zhe-Yu Ou, and Leonard Mandel. Measurement of subpicosecond time intervals between two photons by interference. *Phys. Rev. Lett.*, 59(18):2044, 1987.

[137] MJ Collett. Exact density-matrix calculations for simple open systems. *Phys. Rev. A*, 38(5):2233, 1988.

[138] Andrei B Klimov and Sergei M Chumakov. *A group-theoretical approach to quantum optics*. John Wiley & Sons, 2009.

[139] Leonard Mandel and Emil Wolf. *Optical coherence and quantum optics*. Cambridge university press, 1995.

[140] A Kuzmich, WP Bowen, AD Boozer, A Boca, CW Chou, L-M Duan, and HJ Kimble. Supplementary information: A cauchy-schwarz inequality for coincidence detection of the (1, 2) fields. *Nature*, 423(6941):731–734, 2003.

[141] Milrian S Mendes and Daniel Felinto. Perspectives for laboratory implementation of the duan-lukin-cirac-zoller protocol for quantum repeaters. *Phys. Rev. A*, 84(6):062303, 2011.

[142] MD Eisaman, L Childress, A André, F Massou, AS Zibrov, and MD Lukin. Shaping quantum pulses of light via coherent atomic memory. *Phys. Rev. Lett.*, 93(23):233602, 2004.

[143] Vlatko Balić, Danielle A Braje, Pavel Kolchin, GY Yin, and Stephen E Harris. Generation of paired photons with controllable waveforms. *Phys. Rev. Lett.*, 94(18):183601, 2005.

[144] DN Matsukevich, T Chaneliere, M Bhattacharya, S-Y Lan, SD Jenkins, TAB Kennedy, and A Kuzmich. Entanglement of a photon and a collective atomic excitation. *Phys. Rev. Lett.*, 95(4):040405, 2005.

[145] Milrian S Mendes, Pablo L Saldanha, José WR Tabosa, and Daniel Felinto. Dynamics of the reading process of a quantum memory. *New J. Phys.*, 15(7):075030, 2013.

[146] Rafael A de Oliveira, Milrian S Mendes, Weliton S Martins, Pablo L Saldanha, José WR Tabosa, and Daniel Felinto. Single-photon superradiance in cold atoms. *Phys. Rev. A*, 90(2):023848, 2014.

[147] Robert H Dicke. Coherence in spontaneous radiation processes. *Phys. Rev.*, 93(1):99, 1954.

[148] Marlan O Scully, Edward S Fry, CH Raymond Ooi, and Krzysztof Wódkiewicz. Directed spontaneous emission from an extended ensemble of n atoms: Timing is everything. *Phys. Rev. Lett.*, 96(1):010501, 2006.

[149] Marlan O Scully and Anatoly A Svidzinsky. The super of superradiance. *Science*, 325(5947):1510–1511, 2009.

[150] Tom Bienaimé, Romain Bachelard, Nicola Piovella, and Robin Kaiser. Cooperativity in light scattering by cold atoms. *Fortschr. Physik*, 61(2-3):377–392, 2013.

[151] Christoph Simon, Mikael Afzelius, Jürgen Appel, A Boyer de La Giroday, SJ Dewhurst, Nicolas Gisin, CY Hu, F Jelezko, Stefan Kröll, JH Müller, et al. Quantum memories. *Eur. Phys. J. D*, 58(1):1–22, 2010.

[152] Mikael Afzelius, Nicolas Gisin, and Hugues De Riedmatten. Quantum memory for photons. *Phys. Today*, 68(12):42–47, 2015.

[153] Félix Bussières, Nicolas Sangouard, Mikael Afzelius, Hugues de Riedmatten, Christoph Simon, and Wolfgang Tittel. Prospective applications of optical quantum memories. *J. Mod. Opt.*, 60(18):1519–1537, 2013.

[154] Alexander I Lvovsky, Barry C Sanders, and Wolfgang Tittel. Optical quantum memory. *Nature Phot.*, 3(12):706–714, 2009.

[155] Nicolas Sangouard, Christoph Simon, Hugues De Riedmatten, and Nicolas Gisin. Quantum repeaters based on atomic ensembles and linear optics. *Rev. Mod. Phys.*, 83(1):33, 2011.

[156] Erwan Bimbard, Nitin Jain, Andrew MacRae, and AI Lvovsky. Quantum-optical state engineering up to the two-photon level. *Nature Phot.*, 4(4):243–247, 2010.

[157] Michelle O Araújo, Ivor Krešić, Robin Kaiser, and William Guerin. Superradiance in a large and dilute cloud of cold atoms in the linear-optics regime. *Phys. Rev. Lett.*, 117(7):073002, 2016.

[158] SJ Roof, KJ Kemp, MD Havey, and IM Sokolov. Observation of single-photon superradiance and the cooperative lamb shift in an extended sample of cold atoms. *Phys. Rev. Lett.*, 117(7):073003, 2016.

[159] CJ Foot. Laser cooling and trapping of atoms. *Contemp. Phys.*, 32(6):369–381, 1991.

[160] Alan L Migdall, John V Prodan, William D Phillips, Thomas H Bergeman, and Harold J Metcalf. First observation of magnetically trapped neutral atoms. *Phys. Rev. Lett.*, 54(24):2596, 1985.

[161] C Monroe, W Swann, H Robinson, and C Wieman. Very cold trapped atoms in a vapor cell. *Phys. Rev. Lett.*, 65(13):1571, 1990.

[162] Eric A Cornell, Chris Monroe, and Carl E Wieman. Multiply loaded, ac magnetic trap for neutral atoms. *Phys. Rev. Lett.*, 67(18):2439, 1991.

[163] Jürgen Stuhler, Piet O Schmidt, Sven Hensler, Jörg Werner, Jürgen Mlynek, and Tilman Pfau. Continuous loading of a magnetic trap. *Phys. Rev. A*, 64(3):031405, 2001.

[164] John Weiner. Advances in ultracold collisions: experimentation and theory. *Adv. Atom. Mol. Opt. Phys.*, 35:45–78, 1995.

[165] Kurt Gibble and Steven Chu. Laser-cooled cs frequency standard and a measurement of the frequency shift due to ultracold collisions. *Phys. Rev. Lett.*, 70(12):1771, 1993.

[166] EL Raab, M Prentiss, Alex Cable, Steven Chu, and David E Pritchard. Trapping of neutral sodium atoms with radiation pressure. *Phys. Rev. Lett.*, 59(23):2631, 1987.

[167] Dong-Sheng Ding, Zhi-Yuan Zhou, Bao-Sen Shi, and Guang-Can Guo. Single-photon-level quantum image memory based on cold atomic ensembles. *Nature Commun.*, 4, 2013.

[168] Jonathan Simon, Haruka Tanji, James K Thompson, and Vladan Vuletić. Interfacing collective atomic excitations and single photons. *Phys. Rev. Lett.*, 98(18):183601, 2007.

[169] L-M Duan and HJ Kimble. Efficient engineering of multiatom entanglement through single-photon detections. *Phys. Rev. Lett.*, 90(25):253601, 2003.

[170] Caspar H van der Wal, Matthew D Eisaman, Axel André, Ronald L Walsworth, David F Phillips, Alexander S Zibrov, and Mikhail D Lukin. Atomic memory for correlated photon states. *Science*, 301(5630):196–200, 2003.

[171] DN Matsukevich and A Kuzmich. Quantum state transfer between matter and light. *Science*, 306(5696):663–666, 2004.

[172] DN Matsukevich, T Chaneliere, SD Jenkins, S-Y Lan, TAB Kennedy, and A Kuzmich. Deterministic single photons via conditional quantum evolution. *Phys. Rev. Lett.*, 97(1):013601, 2006.

[173] Daniel A Steck. Rubidium 87 d line data, 2001.

[174] Johan Ospina. Montagem do experimento para a geracao de pares de fotons individuais a partir de ensembles atomicos numa armadilha magneto-optica. Master's thesis, Universidade Federal de Pernambuco, Brazil, 2016.

[175] L Ortiz-Gutierrez, LF Muñoz, D Barros, JE Ospina, ND Alves, AFG Tieco, PL Saldanha, and D Felinto. In preparation.

[176] D Barros, L Ortiz-Gutierrez, LF Muñoz, JE Ospina, ND Alves, AFG Tieco, D Felinto, and PL Saldanha. In preparation.

[177] K-J Boller, A Imamoğlu, and Stephen E Harris. Observation of electromagnetically induced transparency. *Phys. Rev. Lett.*, 66(20):2593, 1991.

[178] Michel Gross and Serge Haroche. Superradiance: an essay on the theory of collective spontaneous emission. *Phys. Rep.*, 93(5):301–396, 1982.